High resolution sea ice monitoring using space borne Synthetic Aperture Radar

Stefan Muckenhuber

Thesis for the degree of philosophiae doctor (PhD)
at the University of Bergen

2017

Date of defence: 6 December 2017

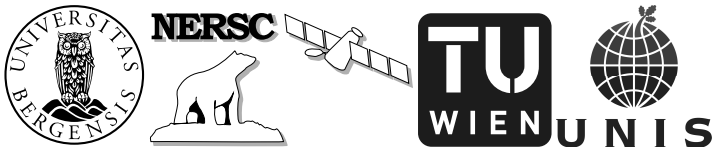

Stefan Muckenhuber: *High resolution sea ice monitoring using space borne Synthetic Aperture Radar,* PhD thesis, © 2017.

WEBSITE:
www.nersc.no

E-MAIL:
stefan.muckenhuber@nersc.no

The author conducted the research for this dissertation at the Nansen Environmental and Remote Sensing Center (NERSC) under the supervision of Stein Sandven (NERSC) and Frank Nilsen (University Centre in Svalbard and University of Bergen). As part of the PhD project the author spent one year at the Technical University of Vienna (TU Wien). The work was funded by the Norwegian Research Council in the framework of the project IceMotion (High resolution sea ice motion from Synthetic Aperture Radar using pattern tracking and Doppler shift, project number 239998/F50).

ABSTRACT

Sea ice represents a major factor in the climate system and updated knowledge about sea ice conditions is important for shipping and offshore industry, local communities and others. Due to its remote location and strong variability in extent and motion, satellite observations are among the most important data sources for sea ice monitoring. Considering the polar night and $60-90\,\%$ cloud coverage over the Arctic, the most reliable sensors for year round, high resolution sea ice monitoring are Synthetic Aperture Radar (SAR) that operate independent of solar illumination and cloud conditions. In the framework of this thesis, the author developed and applied methods for deriving high resolution sea ice information from space borne SAR imagery. A satellite database displaying the area of Svalbard has been established for the time period 2000-2014 and more than 3300 manual interpretations were conducted to distinguish fast ice, drift ice and open water in Isfjorden and Hornsund. The resulting time series revealed a significant reduction of fast ice coverage when comparing the time period 2000-2005 and 2006-2014. The relationship between sea ice, atmosphere and ocean in the two considered fjords has been discussed by comparing fast ice coverage to sea surface temperature from satellite measurements, surface temperature from weather stations and ocean heat content from CTD data. To derive automatic sea ice/water classification of dual polarisation Radarsat-2 SAR imagery, an algorithm based on texture features and support vector machine has been developed and applied operationally in the period 2013 until 2015. Validating the algorithm against 2700 manually derived ice charts from the Norwegian Meteorological Institute revealed an accuracy of $91 \pm 4\,\%$. The algorithm showed better performance in winter than in summer. To retrieve sea ice motion information from consecutive SAR images, a feature-tracking algorithm has been developed for Sentinel-1 data based on ORB (Oriented FAST and Rotated BRIEF). The algorithm locates corners, describes the surrounding area and and connects similar corners from one image to the next. The main advantages of the developed feature-tracking algorithm are the computational efficiency and the independence of the vectors in terms of position, lengths, direction and rotation. However, the vector distribution is not controlled by the user. To overcome this issue, a combined algorithm including a pattern-matching approach has been developed as a successor of the introduced feature-tracking algorithm. Based on a filtered feature-tracking vector field, drift and rotation on the entire SAR scene are estimated. This initial drift field limits the search area for a consecutive pattern-matching algorithm that provides small to medium scale adjustments of drift direction, length and rotation. Assessing the potential performance of the combined algorithm with buoy GPS data using 240 Sentinel-1 image pairs yielded a logarithmic normal distribution of the displacement difference with a median at 352.9 m using HV polarisation and 535.7 m using HH polarisation.

LIST OF PUBLICATIONS

PUBLICATION I

Stefan Muckenhuber[1], Frank Nilsen[2,3] , Anton Korosov[1] and Stein Sandven[1]: Sea ice cover in Isfjorden and Hornsund, Svalbard (2000–2014) from remote sensing data, The Cryosphere, 10, 149-158, doi:10.5194/tc-10-149-2016, 2016

PUBLICATION II

Natalia Zakhvatkina[4,5], Anton Korosov[1], Stefan Muckenhuber[1], Stein Sandven[1], Mohamed Babiker[1]: Operational algorithm for ice/water classification on dual-polarized RADARSAT-2 images, The Cryosphere, 11, 33-46, doi:10.5194/tc-11-33-2017, 2017

PUBLICATION III

Stefan Muckenhuber[1], Anton Korosov[1] and Stein Sandven[1]: Open-source feature-tracking algorithm for sea ice drift retrieval from Sentinel-1 SAR imagery, The Cryosphere, 10, 913-925, doi:10.5194/tc-10-913-2016, 2016

PUBLICATION IV

Stefan Muckenhuber[1] and Stein Sandven[1]: Open-source sea ice drift algorithm for Sentinel-1 SAR imagery using a combination of feature tracking and pattern matching, The Cryosphere, 11, 1835-1850, doi:10.5194/tc-11-1835-2017, 2017

1 Nansen Environmental and Remote Sensing Center (NERSC), Thormøhlensgate 47, 5006 Bergen, Norway
2 University Centre in Svalbard (UNIS), P.O. Box 156, 9171 Longyearbyen, Norway
3 Geophysical Institute, University of Bergen, P.O. Box 7800, 5020 Bergen, Norway
4 Nansen International Environmental and Remote Sensing Centre (NIERSC), 14th Line 7, Office 49, Vasilievsky Island, St. Petersburg, 199034, Russian Federation
5 Arctic and Antarctic Research Institute (AARI), Beringstr. 38, St. Petersburg, 199397, Russian Federation

ACKNOWLEDGEMENTS

First and foremost, I want to thank my supervisors Stein Sandven and Frank Nilsen. It has been a great pleasure to work with you and I am deeply grateful for your guidance and support. You gave me the opportunity to work and live in a number of different countries as part of this dissertation and this has certainly broaden my horizon and inspired my research.

I want to express my gratitude to several research groups for their scientific advice and collaboration, including Hanne Sagen and Mohamed Babiker from NERSC, Natalia Zakhvatkina from NIERSC, Wolfgang Dierking and Thomas Hollands from AWI, Ronald Kwok and Benjamin Holt from JPL and Wolfgang Wagner from TU Wien.

CONTENTS

1 INTRODUCTION

The thesis is divided into four chapters. The following Chapter 1 is an introduction to both the study object sea ice and our main mean of observation, the Synthetic Aperture Radar (SAR). The sea ice formation process is described, as well as the importance of sea ice for environment, shipping and offshore industry, local communities and others. Sea ice observations based on field techniques are discussed and the role of satellite remote sensing in sea ice monitoring. The basic concept of space borne SAR is explained to introduce the technique that enables high resolution sea ice monitoring independent of weather and solar illumination. Chapter 2 describes the methods that are applied for high resolution sea ice monitoring and explains why SAR represents our main source for continuous year round observations. Pre-processing steps for SAR imagery that can be beneficial for sea ice monitoring, like incidence angle correction and thermal noise removal, are briefly introduced. An overview is given of the work that has been done so far in the field of sea ice classification and sea ice motion retrieval from SAR and the papers presented as part of this thesis are put into context with previously published literature. A summary of the fours papers that are presented as part of this thesis can be found in Chapter 3. The thesis closes with Chapter 4 that includes a discussion on the presented work and an outlook on future research in the field of high resolution sea ice monitoring.

1.1 SEA ICE FORMATION

Formation of ice crystals occur in both freshwater lakes and saline oceans, when the atmosphere cools down the surface water to the freezing point. However, due to the presence of salt, properties and appearance of sea ice are significantly different from freshwater ice.

The water salinity is the controlling factor that governs the temperature dependence of both density and freezing temperature of the water. The maximum density of freshwater is reached at 3.98°C. This value decreases with increasing salinity to −3.5°C at 35‰salinity. At the same time, the freezing temperature decreases with salinity from 0°C in freshwater to −1.88°C at 35‰. The two temperatures are equal to −1.32°C at a critical salinity value of 24.69‰.

The salt induced changes in density and freezing temperature affect the vertical convection that arises during surface cooling. As the atmosphere removes heat from the water surface, the upper layer initially becomes denser and sinks, allowing warmer water from below rise to the surface. Eventually the entire water body reaches its maximum density temperature and the convection stops. Further cooling lowers only the temperature of the uppermost layer and once the freezing point is reached, the heat extraction leads to ice growth.

In the case of freshwater, the critical density point is at 3.98°C, meaning that a freshwater lake allows surface ice growth even though the interior of the water body is not colder than 3.98°C. The freezing temperature of sea water however, is above the maximum density temperature, meaning that the entire depth of the water body must be cooled down to −1.88°C before ice growth is possible. Considering up to 5000 m depth in the Arctic ocean, cooling down the entire water column to the freezing point is certainly not possible with observed surface energy fluxes. Nevertheless, sea ice growth occurs every year in the Arctic ocean. Instead of cooling the entire water column, the convection depth is usually limited to 50-200 m (also called mixing layer) due to salt induced stratification. In typical Arctic conditions, water density is controlled by the salinity range rather than the temperature variation. The water below the mixing layer has a higher salinity and is therefore denser regardless of a different temperature.

After reaching freezing temperature, continuing atmospheric cooling eventually leads to formation of ice crystals - given the presence of a sufficient number of nuclei. Independent of water salinity, ice crystals up to a few millimetres are generally formed in the shape of platelets due to the anisotropic growth behaviour of hexagonal crystals like ice, i.e. the basal plane is the preferred growing direction.

Under calm conditions, the platelets float parallel to the water surface and further freezing leads to consolidation and a smooth and solid ice cover is formed. This is typical for lake ice. In the ocean, calm conditions lead to the formation of a continuous but flexible ice sheet, called Nilas, that initially appears dark (thickness < 5 cm) and becomes brighter with increasing thickness ($5 - 10$ cm).

However, wind stress on the ocean surface rarely allows for this quiescent initial formation, but rather mixes the upper water columns and loose, randomly oriented ice crystals (Frazil Ice) are formed until a surface layer of slush builds up. Instead of consolidation, the Frazil Ice experiences a cyclic compression following the wave motion. Once compressed and cooled enough, the crystals bond with each other and eventually form disc-shaped features with diameter ranging from 10 cm to several metres. The edges of the discs are usually raised due to rotation and collision against each other. This ice type is named Pancake Ice after its characteristic appearance. It is commonly observed in the open sea, where the surface is generally rougher, and in particular in the Southern ocean.

Once the ocean surface is covered by a closed ice sheet, either due to the formation of Nilas or by consolidation of Pancake Ice, ice growth continues vertically downwards along the direction of the maximum heat flow from the relatively warm underlaying water to the cold atmosphere. Due to the spatial limitation in horizontal direction, ice crystals with a preferred growth direction along the vertical axis are favoured. So called congelation ice starts to build with a vertical columnar structure.

Salt molecules are not embedded in the ice crystals and increase the salinity of the surrounding sea water, which is then referred to as brine (a solution of salt in water with salinity values above average seawater). Due to its high density, a large portion of the brine is ejected by sinking and causes convec-

tion in the water layer beneath. A part of the brine however, remains in the sea ice, trapped by surrounding ice crystals, and forms brine pockets. The shape of the brine pockets can be cylindrical, in particular in the congelation ice, but also round or irregular, which is most common in the upper ice layer that is built of Frazil Ice. The temperature of the ice represents the freezing temperature of the brine, which means that size and salinity depend on the ice temperature. Brine ejection occurs not only during ice formation but continues as the ice ages. Typical salinity values of First Year Ice (FYI) are between $5 - 15‰$, whereas Multi Year Ice (MYI) is often below $5‰$.

The brine pockets have a significant impact on the sea ice properties. Compared to freshwater, sea ice appears much brighter which is linked to a higher albedo. More than three quarters of the incoming short wave radiation penetrate lake ice, whereas sea ice reflects more than 50%. The lower salinity of MYI, compared to FYI, makes the ice more resistant which means it is difficult and energy consuming for icebreakers to navigate. Younger (hence saltier) sea ice, as well as warmer sea ice is weaker in strength, since the liquid fraction, represented by the volume of brine pockets, is larger compared to old and cold ice. On the other side, MYI that survived several seasons can be fresh enough to supply the drinking water for a polar expedition [Petrich and Eicken, 2010; Stein Sandven and Johannesen, 2006; M. Shokr and Sinha, 2015].

1.2 IMPORTANCE OF SEA ICE

Depending on the season, 5% to 10% of the earth surface is covered by sea ice. Located in high latitudes, sea ice experiences a strong seasonal cycle and the extent varies between 4 million km^2 (September) to 15 million km^2 (March) in the Arctic and 3 million km^2 (February) to 18 million km^2 (September) in the Antarctic. A decline in sea ice cover has been observed in the last decades most visible when considering Arctic September ice extent that decreased from almost 8 million km^2 in 1980 to slightly above 4 million km^2 in 2016 [Stroeve and W. Meier, 2017]. Despite its remote location in the polar oceans, sea ice receives increasing human interest, because of its strong impact on ocean, atmosphere, flora, fauna, ship navigation, offshore industry, local communities and others.

Sea ice can be considered as a thin blanket that covers the polar ocean surface and separates it from the atmosphere above. Its vertical extent is limited to a few meters and very thin compared to ocean and atmosphere. This results in a strong vulnerability against small external perturbations. On the other hand, sea ice has also a major influence on the state of ocean and atmosphere. Because of its ability to reveal small climatic changes and its strong interaction with ocean and atmosphere, sea ice represents one of the most important indicator of climate change and a crucial component in climate research [Dieckmann and Hellmer, 2010]. Thermal and optical properties of sea ice are important input parameters for global climate models. The state of the sea ice cover has a strong influence on large-scale ocean and atmosphere circulations not only in high, but also mid latitudes [M. Shokr and Sinha, 2015].

The fluxes of heat, moisture and momentum across the ocean-atmosphere interface do not only affect the sea ice cover, but are to a large extent controlled by it. By reducing convective heat exchange and outgoing longwave radiation, sea ice effectively insulates the comparable warm ocean from the cold polar atmosphere. When daylight is present, sea ice reflects a high portion of incoming shortwave radiation, that would otherwise warm the upper ocean layer. During sea ice growth, brine is ejected and cold, saline water is produced that sinks down causing convection in the underlaying ocean layers. Strong ice growth can lead to the production of water that is dense enough to reach the deep water basins [McPhee, 2008].

Apart from land fast ice, that is attached to the coastline, sea ice is not fixed to any location, but constantly forced into motion by wind and surface currents. Sea ice drift can take place over large distances and into lower latitudes, where thermodynamic conditions cause ice melt rather than growths. Melting sea ice decreases both temperature and salinity of the upper ocean layer with effects on stratification and surface currents. An example for large scale ice export from the Arctic into lower latitudes is western Fram Strait, where strong southward ice velocities are found throughout the year. Sea ice drift can also shift the ice edge in a significant manner, defining the safe area for vessels with no ice tolerance. Divergence zones inside the pack ice can cause large fractures, where open water areas appear. Convergence zones on the other hand, can build up large pressure ridges, that are challenging even for ice breaker. Knowledge about sea ice drift is therefore crucial for navigation and any other offshore activity in sea ice covered waters [Leppäranta, 2011; M. Shokr and Sinha, 2015].

Safe marine navigation and offshore platforms situated in polar oceans require timely information on sea ice extent, type, strength and surface features along with meteorological data to evaluate possible routes, the need for ice breaker assistance etc. Sea ice charts, based on manual interpretation of satellite imagery, are therefore produced on a regular basis by several national institutes. Vessels with zero ice tolerance have to avoid sea ice covered areas at all and are mostly interested in information on ice edge location. Depending on the ice class, ships with a strengthened hull and strong enough engines can navigate through different ice types and need to consider additional ice information to evaluate possible routes. Both fuel consumption and navigation time can very significantly depending on ice conditions and there is a need for high resolution ice classification to e.g. detect fractures in the ice, also called leads, that can be used for navigation. Existing ice charts often lack sufficient temporal and spatial resolution to evaluate the best possible route. Recent Arctic summer ice loss increased the attention of shipping and offshore industry on the polar oceans. The sea ice decline is expected to continue and eventually open new profitable shipping routes and easy access to previously ice covered areas that are rich in natural resources. An example is the increasing interest in the Northwest and Northeast passage that could shortcut the way from the Atlantic to the Pacific via the Arctic ocean [Stein Sandven and Johannesen, 2006; M. Shokr and Sinha, 2015].

Shipping and offshore industry consider sea ice mainly as an obstacle that prevent safe and profitable operations in the polar oceans. However, for local communities in the Arctic, whose life is directly affected by sea ice,

the presence of sea ice is a very welcoming sight. Until the 1960's, before the traditional Inuit lifestyle was given up due to external influence, life took place both on land and on sea ice depending on the season. During winter and spring, temporary igloo villages were built on sea ice. People lived, traveled and hunted on the ice - even children were born on sea ice. The Inuit communities in the Canadian Arctic and Greenland are known for their profound knowledge, detailed terminology, myths and stories about sea ice. This reflects the important role that sea ice played and continues to play in their life. Temporary villages are no longer built during winter, but sea ice is still an important mean for travel, transportation and hunting. The introduction of snowmobiles in the 1970's has certainly increased speed and range of Arctic activities, but a strong dependence on sea ice remains [M. Shokr and Sinha, 2015].

Both in the Arctic and Antarctic, sea ice forms a unique habitat for a large variety of species including micro organisms like bacteria and algae, birds and marine mammals like seals and polar bears. Different types of algae are known for flourishing at the ice ocean interface. They use sea ice as a platform to remain in the uppermost ocean layer where incoming sunlight is sufficient to support growth [Arrigo et al., 2010]. Marine birds and mammals have evolved many different ways to exploit the presence of sea ice as hunting ground, shelter, for breeding and feeding etc. On the other side, several species experience sea ice merely as a barrier that first has to melt or break into smaller pieces before they can move back into previously ice covered areas. Presence of sea ice can separate the predator from its prey, giving some resident populations the opportunity to grow large during the period with ice cover [Tynan et al., 2010].

1.3 SEA ICE OBSERVATIONS

Historical records of Arctic sea ice distribution are hardly ever older than 150 years. Sea ice conditions before can be constructed based on sediment records and deposits along the Arctic coast. Ice rafted debris and other marine proxies that are found in marine and coastal sediment cores support the existence of sea ice in the area. Driftwood is primarily delivered on shore if the coastline is not shielded by land fast ice. Several types of marine mammals like polar bears, seals and different kinds of whale have a strong affinity for sea ice. Finding corresponding bones leads to the assumption that sea ice was present in this area.

It was not until the end of the 19^{th} century that sea ice edge positions around the entire Arctic were recorded systematically by ships - with varying quality and position quantity, however. The most detailed historical records exist from coastal seas that were accessible to shipping, in particular the Barents Sea, where ice edge information was collected over the last four centuries [Polyak et al., 2010]. A milestone in polar oceanography and sea ice research was Nansen's Fram expedition in 1893 - 1896. The Norwegian explorer Fridtjof Nansen attempted to reach the North Pole by freezing the specially designed ship Fram into the pack ice off the Siberian coast, and let it follow the transpolar ice drift through the Arctic into the Atlantic Ocean. Despite missing the geographical North Pole, the expedition is considered a success, since Fram safely exited the ice pack into the North Atlantic and

the extensive scientific observations [Nansen, 1902] represent a significant contribution to the understanding of the polar oceans.

Soviet and Russian research stations were deployed in the Arctic on multi year ice floes between 1937 - 1938, 1950 - 1951, 1954 - 1991 and 2003 - 2015. The results of these expeditions represent a very important contribution to long-term field observations of many sea ice parameters such as ice thickness, drift velocity and snow depth distribution [Warren et al., 1999]. Since 2002, a privately funded Russian sea ice camp (Camp Barneo) is established once per year close to the North Pole as a tourist attraction. A small number of scientists are generally included that may use the infrastructure to collect observations for research purposes.

Field techniques for sea ice observations include a vast number of methods to measure ice thickness and roughness, optical, thermal and mechanical properties of sea ice, snow characteristics, biological activities connected to sea ice, chemical composition, pollution etc. [Eicken et al., 2009] However, despite access to modern equipment and infrastructures like nuclear powered ice breaker, in-situ data remain comparable sparse considering the enormous extent, its strong variability (17 million km^2 to 28 million km^2) and constant motion. This is in particular the case for Antarctic sea ice. Until the 1950's a prevailing thought was that Antarctic sea ice was probably not any different than Arctic sea ice and not many bothered studying it, since the logistical challenges are higher than they are already in the Arctic [M. Shokr and Sinha, 2015].

To study and observe sea ice properties on a larger scale, remote sensing tools are therefore irreplaceable. Sensors mounted on helicopters and airplanes can provide sea ice data for the overflown area and satellite borne sensors are able to monitor sea ice up to global scale [W. N. Meier and Markus, 2015].

1.4 SATELLITE REMOTE SENSING OF SEA ICE

The basic challenge of satellite remote sensing is to measure properties of the observed object with a sensor that is attached to a fast moving platform in several 100 km to several 1000 km distance. A typical height of polar orbiting satellites, which represent the majority of satellites used for sea ice monitoring, is in the order of 700 km to 800 km, but geostationary satellites are as far away as 35000 km. To overcome the large distance, all satellite sensors (apart from satellites measuring the gravity field of the Earth) use electromagnetic waves that are either emitted or reflected by the observed object. Based on measurements of the waves that travelled to the sensor, one can derive information about the properties of the object.

Depending on the source of the electromagnetic wave, satellite sensors are divided into two categories: active and passive. An active sensor includes both transmitting and receiving antenna. It emits the electromagnetic wave that is reflected by the object and measures the returning signal. Transmitting and receiving can be done by the same physical antenna. A passive sensor does not have the capability to emit waves, but includes only a receiving antenna. In this case, the electromagnetic source can either be the object itself

or a third component that illuminates the object, e.g. the sun illuminates the Earth surface during daytime.

The electromagnetic spectrum includes all possible frequencies and respective wave lengths that could be used for remote sensing. However, observing surface properties of the Earth from space limits the alternatives, because the electromagnetic wave has to travel through the atmosphere. Oxygen and ozone in the upper atmosphere shield us from high frequency radiation like gamma rays and x-rays. The water vapour absorbs most parts of the infrared spectrum and the ionosphere blocks low frequency radio waves. Two so called atmospheric windows remain that are used for satellite remote sensing: the optical and the radar window. Through the optical window, visible light and parts of the infrared spectrum can pass with some atmospheric distortion depending on e.g. cloud cover. To a large degree independent from weather and other distortions, parts of the microwave and radio wave spectrum can transit the atmosphere through the radar window.

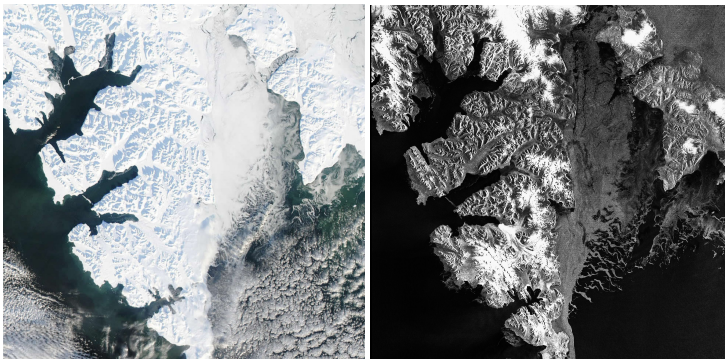

Figure 1: Satellite images of Svalbard archipelago and sea ice: (left) RGB image constructed from three bands acquired by NASA's VIS/IR sensor MODIS (Moderate Resolution Imaging Spectroradiometer) on 13 March 2014. (right) SAR image from CSA's Radarsat-2 taken on 16 March 2014.

The very first image of sea ice captured from space was taken by NASA's Television and Infrared Observations Satellite (TIROS) in 1960. TIROS belongs to the group of VIS/IR (visual/infrared) sensors. These are passive sensors using the optical window of the atmosphere. The electromagnetic sources for this type of sensor are the sun in the visual part of the spectrum and the earth surface in the infrared spectrum. The sensor divides the considered part of the spectrum into frequency bands and measures the intensity individually for each band. Appearing similar to the product of common cameras, RGB images can be constructed by combining the corresponding frequency bands (Figure 1). The albedo difference between sea ice and open water allows straightforward sea ice identification. A more advanced analysis of the different frequency bands can provide a variety of additional earth surface parameters, that are not revealed in the RGB image. The infrared bands reflect the temperature distribution of the surface and can be used for sea ice identification during winter, when the ice surface is considerably colder than the open water area. Depending on frequency band and acquisition mode, typical resolutions are in the order of 10 - 100 m in the visual

Table 1: Space born Synthetic Aperture Radar sensors for sea ice observations.

Sensor	Operator	Band	Polarisation	Period
Seasat SAR	NASA	L	HH	1978
ERS-1	ESA	C	VV	1991-2000
ERS-2	ESA	C	VV	1995-2011
JERS-1	JAXA	L	HH	1992-1998
Radarsat-1	CSA	C	VV	1995-2013
Radarsat-2	CSA	C	HH, VV, HV, VH	2007-today
Envisat ASAR	ESA	C	HH, VV, HV, VH	2002-2012
ALOS PALSAR	JAXA	L	HH, VV, HV, VH	2006-2011
ALOS-2 PALSAR-2	JAXA	L	HH, VV, HV, VH	2014-today
TerraSAR-X	DLR	X	HH, VV, HV, VH	2007-today
Sentinel-1A/B	ESA	C	HH, VV, HV, VH	2014-today

spectrum and 100 - 1000 m in the infrared spectrum. Among the successors of TIROS are NASA's VIS/IR satellites Landsat 1 - 8 (https://landsat.usgs.gov). Continuously operating since 1972, the Landsat mission provides the longest temporal record of high to medium resolution images of the Earth's surface. The quality of sea ice observations through the optical window is strongly depending on weather conditions, since the considered electromagnetic waves are scattered and blocked by clouds. Considering 60 - 90 % cloud coverage in the Arctic, this represents a major drawback. In addition, the visual channels of the sensor do not provide useful data during polar night, since the sun is not illuminating the surface.

Introduced in the late 1960's, space borne passive microwave (PM) sensors build the most important data source for global, long-term sea ice observations until today. Similar to IR sensors, PM sensors capture electromagnetic waves that are directly emitted by the Earth's surface. However, instead of a strong temperature dependence (as it is the case for the infrared spectrum), the intensity of emitted microwaves is mostly varying due to different emissivity values. The emissivity is a frequency depending material property and can be understood as the material's ability to emit radiation. Due to its crystalline structure, sea ice has typically higher microwave emissivity values than open water, meaning that sea ice emits more microwaves and appears brighter to the sensor [Ulaby, Long, et al., 2014; Ulaby, Moore, et al., 1986]. The first PM sensor was launched into space in 1968 on board of the Russian Kosmos-243 and the first sea ice estimates from PM are based on data from the Electrically Scanning Microwave Radiometer (ESMR) on the Nimbus-5 satellite that has been operational between 1973 and 1976. Since 1978, a number of different PM sensors, like SMMR (1978 - 1987), SSM/I (1987 - 2008), SSMI/S (2003 - today), AMSR-E (2002 - 2011), SMOS (2009 - today) and AMSR-2 (2012 - today), have provided the longest sea ice observation record with global and daily coverage. Corresponding ice concentration maps and datasets are distributed by the National Snow and Ice Data Centre (http://nsidc.org). Passive microwave sensors operate on a very low energy level limiting the spatial resolution to the order 10 - 50 km. Another drawback beside the low resolution is the low reliability of ice concentration values in late summer, because a high fraction of melt ponds has a strong effect on the result.

To provide high resolution images independent of cloud conditions and solar illumination, an active microwave sensor called Synthetic Aperture Radar (SAR) has been launched into space in 1978 onboard of NASA's Seasat satellite. Despite its short operation period of 105 days, the mission successfully demonstrated the great value of SAR for sea ice research and monitoring. Depending on the acquisition mode, SAR imagery over sea ice are usually provided with a resolution of order 10 - 100 m (NB: a higher resolution generally decreases the coverage). The data allows to provide high resolution sea ice maps including information on ridges and leads, which is crucial for ship navigation inside the ice cover and for determining heat exchange rates between ocean and atmosphere. Identifying and tracking individual floes from one SAR image to the next lead to the first detailed ice motion maps. Unlike VIS/IR and PM, a single SAR pixel value does not provide enough information to identify the ice concentration, but the textural characteristics allows to both identify and classify different sea ice types. The values in a SAR image (Figure 1) represent the radar backscatter, i.e. how much of the emitted signal is returned back to the sensor, and must not be confused with conventional black and white image values that depict the brightness or albedo of the object. The measured radar backscatter is a function of incidence angle, polarisation and scattering characteristics of the illuminated surface. The parameters affecting the scattering characteristics of sea ice are surface roughness, orientation of the surface features, as well as dielectric permittivity (linked to the salinity of the ice) and dielectric discontinuities, like gas bubbles. The band of a SAR sensor defines the frequency spectrum of the antenna. Common SAR bands are X-band (centre frequency of 9.4 GHz and corresponding wavelength 3.2 cm), C-band (5.3 GHz, 5.7 cm) and L-band (1.3 GHz, 24 cm). SAR sensors are capable of emitting (first letter in polarisation notation) and receiving (second letter) signals in both horizontal (H) and vertical (V) polarisation. Emitting and receiving the same polarisation is defined as co-polarisation mode (HH, VV), whereas HV and VH are referred to as cross-polarisation. Modern SAR sensors can facilitate the possibility to acquire images in single, dual or quad polarisation, i.e. taking one, two or four images of the same scene with a different emitting and/or receiving polarisation. Table 1 gives an overview of past and current space borne SAR sensors used for sea ice applications [Stein Sandven and Johannesen, 2006; M. Shokr and Sinha, 2015; Ulaby, Long, et al., 2014; Ulaby, Moore, et al., 1986].

The following Section 1.5 explains the concept of SAR, as well as the corresponding image construction for a more profound understanding of image interpretation and application fields.

1.5 SYNTHETIC APERTURE RADAR

A Synthetic Aperture Radar (SAR) is an imaging radar, mounted on a moving platform (e.g. aircraft, satellite), that utilises a combination of radar hardware, waveforms, signal processing, and relative motion to create high-resolution complex images of the illuminated area [Showman, 2010].

A conventional radar is an active sensor, that both transmits electromagnetic pulses, which are eventually reflected by an object, and receives the returning signal. By precisely measuring the time difference between trans-

mission and receipt of the reflected pulse, a radar can determine the distance between itself and the detected object. The range resolution of a radar system is defined as the minimum distance difference of two separated objects in order to be distinguished by the radar. If the distance difference of the two objects is less than the range resolution, the radar will only recognise a complex combination of the reflected energy from the two objects [McCandless and Jackson, 2004; Tomiyasu, 1978].

The simplest approach to provide two-dimensional reflectivity images is to mount a conventional radar in a side-looking angle on a moving platform and make continuous measurements. Until the 1950s, these systems, denoted as Side-Looking Airborne Radar (SLAR), were used to provide two-dimensional images without making use of the synthetic aperture principle [Moreira et al., 2013]. The flight direction of a moving radar is denoted as azimuth or along track, and the line-of-sight direction, perpendicular to the flight direction, as range or across track (Figure 2). The azimuth resolution δ_a of a SLAR is determined by the beamwidth Θ_a, approximately given by the wavelength λ divided by the antenna size d_a, and the distance between radar and reflecting object r_0 [McCandless and Jackson, 2004; Moreira et al., 2013; Sullivan, 2008; Tomiyasu, 1978].

$$\delta_a \approx r_0 \Theta_a \approx \frac{r_0 \lambda}{d_a} \qquad \text{(real aperture)} \tag{1}$$

Considering the technical specifications of Sentinel-1, which has a 12 m long antenna operating at C-band with wavelength 0.18 m, and an orbit height of 700 km, limits the azimuth resolution of a comparable real aperture to 10.5 km. This is certainly not enough for high-resolution sea ice monitoring.

However, utilising that the same object is illuminated not only once, but several times during the pass of the radar (Figure 2) and applying coherent processing of the received overlapping signals allows to construct a synthetic aperture that is much longer than the real aperture. The corresponding synthetic aperture length is given through $L_{sa} = \Theta_a r_0$ and results in a narrower beamwidth $\Theta_{sa} = \lambda / 2L_{sa}$ (the factor two appears due to the two-way travel path of the signal). Equation 2 provides the adjusted azimuth resolution calculation applying the synthetic aperture principle [McCandless and Jackson, 2004; Moreira et al., 2013; Sullivan, 2008; Tomiyasu, 1978].

$$\delta_a \approx r_0 \Theta_{as} \approx \frac{r_0 \lambda}{2L_{sa}} \approx \frac{d_a}{2} \qquad \text{(synthetic aperture)} \tag{2}$$

The above equation implies that a shorter antenna yields a finer azimuth resolution and this makes sense considering that a shorter antenna has a wider beamwidth and therefore illuminates the object over a longer time period. However, it has to be mentioned that technical restrictions and application constraints limit the possibilities of decreasing the antenna length to much. The achieved azimuth resolution, considering the antenna length of Sentinel-1, is in the order of 6 m, which represents a distinct improvement compared to the real aperture restrictions.

The original concept of SAR was invented in 1951 by Carl A. Wiley of the Goodyear Aerospace Corporation, and is described under the name 'Doppler

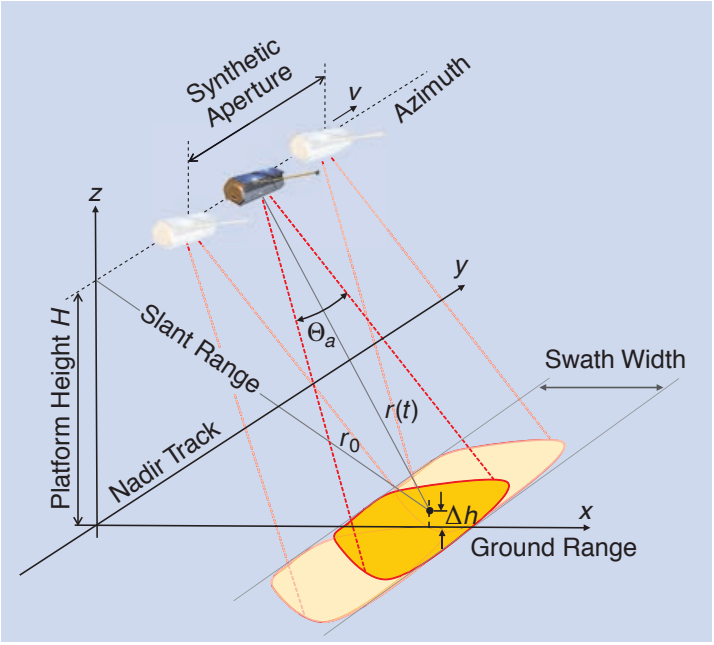

Figure 2: Schematic illustration of the SAR imaging geometry with r_0 being the shortest approach distance, Θ_a the azimuth beamwidth and v the satellite velocity [Moreira et al., 2013].

beam sharpening' in the patent on 'Pulsed Doppler radar methods and apparatus' (United States Patent Office, 1954) as making use of the Doppler frequency shift phenomenon to obtain angular resolution. Carl Wiley observed that the azimuth (along-track) coordinate of a reflecting object, that is linearly passed by a radar with constant velocity, corresponds one-to-one to the instantaneous Doppler shift of the reflected signal. Meaning that a frequency analysis of the reflected signal can enable a finer azimuth resolution than provided by a conventional real aperture radar, that is limited by the width of the physical beam [McCandless and Jackson, 2004; Sullivan, 2008].

A necessity for SAR processing is the fully coherent nature of the utilised radar. A pulse transmitted and received by a coherent radar has a defined phase angle to a reference signal provided by a highly stable continuous radar frequency source, called the waveform generator. E.g. in case the radar frequency is a multiple of the pulse repetition frequency, each pulse starts with the same phase. The coherent recording of the echoes enables the phase history of individual scattering elements to be tracked and the analysis of many echo records eventually delivers very fine resolution in both azimuth and range direction [Tomiyasu, 1978].

To achieve fine range resolution, both SAR and conventional radar utilise frequency modulated pulsed waveforms, so called chirp signals. The amplitude of a transmitted chirp signal is usually constant, whereas the frequency is increased (or decreased) over time in a linear manner. The chirp rate k_τ

describes how the frequency is varied over time, according to $f = k_\tau t$, and yields the pulse bandwidth $B_\tau = k_\tau \tau$ for a chirp with pulse width τ. The spatial resolution in range direction δ_r can be expressed as a function of either the pulse width τ or the reciprocal of the bandwidth B_τ multiplied by the speed of light c and divided by two [McCandless and Jackson, 2004; Moreira et al., 2013; Sullivan, 2008].

$$\delta_r \approx \frac{c\tau}{2} \approx \frac{c}{2B_\tau} \tag{3}$$

The time associated with the travel of the electromagnetic signal at the speed of light is denoted as fast time. The transmission of a chirp signal is followed by an echo window during which the SAR receives and stores the returning signal. The ground range extent of a SAR image, called swath width (Figure 2) depends on the time duration during which the radar is receiving. The pulse repetition frequency defines how many times the transmission and listening procedure is repeated per second. Utilising chirp signals improves the resolution, but makes it necessary to perform a matched filtering step called range compression [Moreira et al., 2013]. As shown in Figure 3 [Younis, 2015], visualising raw SAR data does not yield useful information before signal processing. The first step is to compress the chirp signals to a short pulse. This can be done either in the time domain by a convolution of the range signal with the range reference function (defined by the chirp signal) or in the frequency domain using simple multiplication. The latter is usually performed due to much lower computational cost. The resulting range compressed image reveals improved information about the relative distance between the sensor and the reflecting object [Moreira et al., 2013].

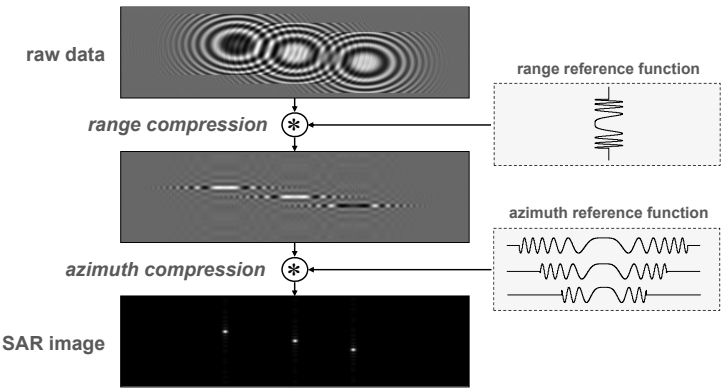

Figure 3: SAR processing chain of three point reflectors including a schematic illustration of range and azimuth reference functions [Younis, 2015].

In the direction orthogonal to the radar beam, i.e. azimuth direction, the SAR application is distinctive in its use of aperture synthesis to improve the spatial resolution. In contrast to a SLAR, a SAR consists not only of conventional radar building blocks such as antenna, transmitter and receiver, but also includes a data collection system providing coherent Doppler phase histories and an advanced signal processor capable of producing images out

of these phase histories [McCandless and Jackson, 2004].

As depicted in Figure 2, the satellite carrying the SAR sensor moves with a velocity v through its synthetic aperture and views the same object from different angles. The time associated with the movement of the satellite is denoted as slow time [Moreira et al., 2013]. For the following, we have to assume that the satellite velocity is constant and the object is not moved during the acquisitions. From the viewpoint of a moving SAR mounted on a satellite, a passed object on the ground appears to have a changing line-of-sight velocity relative to the satellite [Sullivan, 2008]. Because SAR involves phase coherent processing, the phase history of an isolated target during the integration time, i.e. the time period during the satellite is illuminating the target, follows a quadratic phase function corresponding to a linear frequency change [Tomiyasu, 1978]. Applying a similar signal processing step as done for range compression, the linear frequency shift in azimuth direction can be utilised to provide much finer azimuth resolution than achieved by a SLAR (Figure 3).

The SAR principle can be illustrated by considering the phase history of an observed point target. The following equations are based on Moreira et al., 2013 and Tomiyasu, 1978. At any point in time t, the distance r between the sensor at position x (distance from closest point on the satellite track) and the target can be described using

$$r = \sqrt{r_0^2 + x^2} \tag{4}$$

where r_0 is the minimum distance at $x = 0$. While the target is illuminated by the SAR, the distance r_0 is in general much larger than x. This allows expanding Equation 4 into a Taylor series and neglecting all but the first two terms, which yields the approximation:

$$r = r_0 \sqrt{1 + \frac{x^2}{r_0}} \approx r_0 + \frac{x^2}{2r_0} \tag{5}$$

NB: This approximation is only done here to provide an easy understanding of the process and is not applied for accurate SAR processing.

The motion of the satellite along the target causes a range variation that is directly related to the azimuth phase φ of the received echo. Hence, φ can be expressed as a function of x.

$$\varphi(x) = \frac{4\pi}{\lambda}(r_0 + \frac{x^2}{2r_0}) = \text{const.} + \frac{2\pi x^2}{\lambda r_0} \tag{6}$$

Assuming the satellite moves with a constant velocity v along the x-axis, yields a quadratic phase behaviour in time. Using the abbreviation $k = \frac{2\pi v^2}{\lambda r_0}$, the time dependent part, excluding the constant phase term, becomes

$$\varphi(t) = kt^2 \tag{7}$$

The quadratic phase behaviour corresponds to a linear change in the received azimuth frequency f, which is also called Doppler frequency in analogy to the Doppler effect.

$$f(t) = \frac{1}{2\pi}\frac{\partial\varphi(t)}{\partial t} = \frac{k}{\pi}t \tag{8}$$

Knowing the phase behaviour provides the azimuth reference function that can be utilised to compress the azimuth signal and eventually makes it possible to produce images with distinctly increased azimuth resolution.

Figure 3 summarises the two basic SAR processing steps range compression and azimuth compression. The corresponding reference functions depend in range direction on the transmitted chirp waveform and in azimuth direction on the geometry with adaptation according to the range. It is an interesting coincident that the frequency variation of the azimuth signal is similar to that in the range domain. Du to its linear frequency modulation, the azimuth signal is also referred to as azimuth chirp [Moreira et al., 2013].

2 METHODOLOGY

High resolution (order 10 - 1000 m) sea ice monitoring from space is done using either VIS/IR or SAR sensors. Due to the passive nature of the VIS/IR sensor, image acquisition is less energy demanding allowing good coverage with comparable high resolution. With the possibility to produce conventional RGB images, the data are easy to understand and represent an important tool for accessing the ice situation during favourable conditions and validating other satellite sensors. However, the dependence on solar illumination and clear sky is a major drawback in the polar regions and prohibit reliable, year round monitoring. Our main source for continuous sea ice monitoring with high temporal and spatial resolution is therefore SAR data and VIS/IR imagery are mainly used for interpretation support of the SAR scenes. The active nature of SAR includes a higher energy demand and limits the acquisition time to around 30 %. Nevertheless, we found good SAR coverage in our area of interest, which is the European Arctic sector. The interpretation of a SAR scene is not as intuitive as for a RGB image, but by understanding the sensor concept and the interaction of the electromagnetic waves with the sea ice surface, many details can be revealed that are not captured by VIS/IR sensors.

The main tasks for high resolution sea ice monitoring from SAR are identifying sea ice on a SAR image (ice/water classification), defining the ice type (sea ice type classification) and tracking recognisable pattern over two, or more, consecutive scenes to observe sea ice motion. Other sea ice parameters like thickness, age, strength and deformation can be estimated from classification and motion products or observed with lower resolution sensors (e.g. passive microwave, scatterometer, altimetry). The following Section 2.1, Section 2.2 and Section 2.3 will introduce the methods that are applied for SAR pre-processing, sea ice classification and sea ice motion retrieval and put the papers that are presented as part of this thesis into context with previously published literature in this field.

2.1 SAR PRE-PROCESSING

Both sea ice classification and sea ice motion retrieval from SAR can benefit from pre-processing steps like incidence angle correction and thermal noise removal.

The backscatter signal of the co-polarisation mode (HH, VV) has a strong dependence on the incidence angle, i.e. the backscatter generally decreases with increasing incidence angle [M. Shokr, 2009]. To compensate for this backscatter decrease in range direction, the image values can be corrected to a certain extent using a linear function of the incidence angle. The angular dependence, however, varies for different types of open water and sea ice [Mäkynen et al., 2002], meaning that the correction factor depends on the

illuminated object. Open water shows in general a higher angular dependence with a strong influence of wind conditions (strong winds are linked to a stronger angular dependence). The backscatter decrease of sea ice can be considered more stable and less affected by wind or other conditions. This allows to use a representative linear correction factor for all sea ice scenes from a certain SAR sensor, as done by Zakhvatkina, Alexandrov, et al., 2013 for ENVISAT ASAR and Zakhvatkina, Anton A. Korosov, et al., 2017 for Radarsat-2.

The returning signals of the cross-polarisation channels (HV, VH) are less sensitive to the incidence angle, but have a comparable low energy level, which reduces the signal to noise ratio and introduces artefacts produced by thermal noise. Corresponding thermal noise correction values are usually provided in the metadata of the SAR image and need to be subtracted from the image values. Zakhvatkina, Anton A. Korosov, et al., 2017 presented a thermal noise removal procedure for HV images from Radarsat-2 as part of an ice/water classification algorithm.

2.2 SEA ICE CLASSIFICATION

Sea ice classification on SAR imagery includes ice/water classification, during which the sea ice covered area is separated from open water, and sea ice type classification, representing another step during which different types of sea ice are identified inside the ice covered area. Ice/water and ice type classification can be done manually or using automatic algorithms.

The challenge of sea ice classification from SAR is, that both sea ice and open water can appear dark (low backscatter) and bright (high backscatter) on the image. Calm open water and flat young ice are usually dark on a SAR image, whereas open water during strong winds can have a similar bright backscatter signal as multi year ice, rough first year ice or young ice covered with frost flowers. Using dual polarisation can add certain information to distinguish sea ice from open water and different ice types, e.g. rough open water appears darker in HV, but some ambiguities remain [Onstott and Shuchman, 2004; Stein Sandven and Johannesen, 2006]. Therefore, image characteristics like spatial structures and image textures need to be considered to perform a reliable classification product [Bogdanov et al., 2005; Clausi, 2002; Maillard et al., 2005; M. E. Shokr, 1991; Soh and Tsatsoulis, 1999; P. Yu et al., 2012].

The human eye is well trained for pattern recognition, enabling experienced sea ice experts to preform manual interpretation of SAR scenes to classify open water and different sea ice types. Compared to automatic algorithms, this approach demands more time effort, but can provide a higher reliability. Several national institutes (Canadian Ice Service, Finnish Meteorological Institute, Norwegian Meteorological Institute, Swedish Meteorological and Hydrological Institute etc.) provide daily sea ice charts based on a combination of satellite imagery and in situ data. Manual interpretation of SAR imagery represents a crucial instrument to produce these operational ice charts, in particular during polar night and cloud coverage, when VIS/IR images do not reveal any information about the ocean surface. However, the provided ice charts have often a limited resolution and cannot be used

to study small regions like Arctic fjords. Automatic algorithms also fail near the coastline, adding to the lack of knowledge about sea ice coverage inside Arctic fjords. To provide high resolution sea ice classification for two Arctic fjords (Isfjorden, Hornsund), Stefan Muckenhuber, Nilsen, et al., 2016 produced a time series (2000 - 2014) classifying open water, fast ice and drift ice using manual interpretation of SAR data and VIS/IR images as validation during polar day. To distinguish fast ice from drift ice, the motion of the ice from one image to the next has been used as additional information.

Automatic sea ice classification algorithms significantly decrease the effort to produce ice charts from SAR imagery. This can increase the temporal resolution of operational products and improve the possibilities to work with large SAR datasets. A number of studies have been conducted to develop automatic sea ice classification algorithms and several corresponding products have been distributed operationally. Dokken et al., 2002 introduced a polynya algorithm for ERS SAR imagery based on wavelet transformation for edge detection and texture analysis to identify open water, new and young ice, and define size and shape of polynyas. To support operational SAR sea ice classification, Soh, Tsatsoulis, et al., 2004 developed a system called ARKTOS (Advanced Reasoning using Knowledge for Typing of Sea Ice) that segments the SAR image, generates descriptors for the segments, uses input from sea ice experts to classify the segments and allows the incorporation of other data types than SAR. Haarpaintner and Solbø, 2007 applied a texture based algorithm, that uses an automatically trained maximum likelihood classifier, on Radarsat-1 and ENVISAT ASAR imagery to distinguish sea ice from open water. Better results were achieved when dividing the SAR images into slices of incidence angle increments to overcome the angle dependence of the SAR backscatter. Karvonen et al., 2005 developed an ice/water classification algorithm for Radarsat-1 based on segmentation and intensity autocorrelation to produce ice charts for the Baltic Sea. Comparison with manual ice charts from the Finnish Ice Service showed about 90 % accuracy. The continuation of this work with Radarsat-2 and ENVISAT ASAR imagery is presented in Karvonen, 2010. Geldsetzer and Yackel, 2009 found that the dual polarisation mode of ENVISAT ASAR enables unambiguous open water discrimination from all sea ice types except thin sea ice using a decision-tree classifier with statistical thresholds. Gill and Yackel, 2012 applied a supervised k-means and maximum likelihood classification algorithm on several polarimetric parameters to assess the potential of discriminating three sea ice types and rough open water. To classify sea ice and open water on Radarsat-2 imagery, Clausi et al., 2010, Ochilov and Clausi, 2012 and Leigh et al., 2014 developed a Map Guided Sea Ice Classification System that combines an image segmentation method named iterative region growing using semantics [Q. Yu and Clausi, 2008] with a pixel based support vector machine. The algorithm has been validated using 20 SAR scenes over the Beaufort Sea and the average accuracy was found to be 96 %. Zakhvatkina, Alexandrov, et al., 2013 introduced a neural network algorithm based on texture feature analysis for sea ice classification of ENVISAT ASAR data that could discriminate two types of first year ice, multi year ice and open water/nilas with an accuracy of around $80 - 85$ %. Operationally distributed ice/water maps based on this algorithm were compared with manual ice charts from the Norwegian Meteorological Institute and provided an accuracy of 97 % [Stein Sandven, Alexandrov, et al., 2012]. Zakhvatkina, Anton A. Korosov, et al., 2017 developed an ice/water classification algorithm for dual polarisation images

from Radarsat-2 and distributed ice/water maps operationally as part of the marine services under the Copernicus programme. More than 2700 SAR scenes have been processed from 2013 until 2015 and the algorithm provided an accuracy of 91 % compared to manual ice charts from the Norwegian Meteorological Institute. After pre-processing the SAR image, i.e. angular correction for HH and thermal noise removal for HV, grey level co-occurrence matrices (GLCM) are computed in a sliding window w. Based on the GLCM, eight texture features are computed, which (together with the backscatter values) specify whether the window w is classified as open water or sea ice. A support vector machine has been trained to classify the window according to the combination of texture feature and backscatter values.

2.3 SEA ICE MOTION

Similar to sea ice classification, sea ice drift can be derived manually or by applying automatic algorithms. However, instead of working with a single SAR scene, two consecutive images have to be considered that allow to follow sea ice formations from one point in time and space to another point in time and space (NB: instantaneous range velocity can also be retrieved from SAR Doppler shift analysis, but this procedure is at an early development stage and accuracy issues with e.g. Sentinel-1 Doppler data hinder the progress in this field). The pattern recognition performance of the human eye allows manual sea ice drift retrieval with good accuracy. However, compared to automatic algorithms, the effort to produce manual drift maps is very large. High resolution drift maps are therefore mainly produced by algorithms and manual drift retrieval is rather used for validation purpose or case studies.

Contemporary algorithms for deriving sea ice drift from two consecutive SAR images are usually based on one of two basic concepts:

- **Feature-tracking**
- **Pattern-matching**

Feature-tracking algorithms detect distinct patterns (features) in both images individually and connect similar features in a second step without the need for knowing their locations. This can be done computationally efficient and the resulting vectors are often independent of their neighbours in terms of position, lengths, direction and rotation, which is an important advantage for resolving shear zones, rotation and divergence/convergence zones. However, the distribution of the resulting vector field is usually not controlled by the user, but defined by the locations of the features that the algorithm successfully connected. Large gaps may occur between densely covered areas, which can eventually lead to missing shear and/or divergence/convergence zones [Stefan Muckenhuber, Anton Andreevich Korosov, et al., 2016]. Pattern-matching algorithms, on the other hand, consider a small template from the first image (around the starting location of the vector) and try to find its match by sliding it over a larger template from the second image. Despite a comparable large computational effort, this approach is widely used, since it allows user defined vector positioning. Tho speeds up the processing, a pyramid approach is generally used for deriving high-resolution drift fields. However, this limits usually the independence of neighbouring vectors, since they are restricted by a lower resolution estimate [Thomas et al., 2008].

Based on the first available space borne SAR imagery from Seasat in 1978, Hall and Rothrock, 1981 and Curlander et al., 1985 derived sea ice displacement vectors by identifying and connecting ice features manually. The first automatic sea ice drift algorithm for Seasat data was introduced by Fily and Rothrock, 1987, who presented a pattern-matching algorithm based on cross correlation using a resolution pyramid, i.e. high resolution drift estimates are based on low resolution estimates, to decrease the computational effort. The algorithm performed well in heavy packed ice with large floes, but fragmentation and rotation represented a challenge. Instead of computing the cross correlation directly, as done by Fily and Rothrock, 1987, Collins and Emery, 1988 proposed an algorithm that computed the correlations in the Fourier domain to increase the computational efficiency and allow for calculating sea ice drift without considering a resolution pyramid. Vesecky et al., 1988 compared drift results from a pair of Seasat SAR images using two automatic approaches: a cross correlation pattern-matching algorithm with resolution pyramid and a feature-tracking algorithm using floe-lead boundary segments. The results of the two approaches complemented each other in many ways and Vesecky et al., 1988 concluded that a combined algorithm including both methods can provide a better sea-ice velocity estimate than either approach could alone. Considering the wide range of movement and conditions that sea ice exhibits in particular in the marginal ice zone, Daida et al., 1990 proposed a set of three feature based algorithms that are chosen and applied according to an automatic pre-examination of the image pair. After the Seasat mission, ERS-1 was the first earth observation satellite that carried a SAR sensor and delivered systematic acquisitions of sea ice covered oceans from 1991 until 2000. Based on ERS-1 data, the first operational sea ice drift retrieval system, called Geophysical Processing System (GPS), was put in place by Ronald Kwok et al., 1990 at the Alaska SAR Facility. The algorithm combined a pattern-matching approach, based on cross correlation, over pack ice with a feature-tracking method, considering the shape of ice floes [McConnell et al., 1991], for the marginal ice zone. A pattern-matching algorithm applying a pyramid resolution introduced by Kloster et al., 1992 was applied on a number of ERS-1 SAR scenes over the Barents Sea during the SeasonalIce Zone Experiment 1992 Stein Sandven, Johannessen, et al., 1999. Calculated drift vectors were compared with in-situ measurement from Argos buoys and the pattern-matching algorithm performed well in the interior of the ice pack, but had difficulties to find drift vectors in the marginal ice zone. Sun, 1996 demonstrated on ERS-1 SAR data that an algorithm based on optical flow methods has the capacity to outperform traditional pattern-matching techniques based on area correlation in areas with strong rotation and deformation, while requiring less computational power. Based on Radarsat-1, ENVISAT ASAR data and the GPS algorithm from Ronald Kwok et al., 1990, sea ice drift fields, in particular over the Western Arctic (depending on SAR coverage), have been calculated for the time period 1996-2012 once per week with a spatial resolution of $10 - 25$ km [R. Kwok and Cunningham, 2002]. A high-resolution sea ice drift algorithm for SAR images from ERS-1 based on a pattern-matching procedure that included both phase correlation and cross correlation was introduced by Thomas et al., 2008, allowing drift calculation up to 400 m resolution. The work on this algorithm has been continued by Hollands and Dierking, 2011, who derived high-resolution sea ice drift from ENVISAT ASAR data. Karvonen, 2012 developed a phase correlation based algorithm with some additional constraints for Radarsat-1 and ENVISAT ASAR data to provide an operational sea ice

drift product for the Baltic Sea. Berg and Eriksson, 2014 introduced a hybrid algorithm for sea ice drift retrieval from ENVISAT ASAR data using phase correlation and a feature based matching procedure that is activated if the phase correlation value is below a certain threshold. Komarov and Barber, 2014 and Stefan Muckenhuber, Anton Andreevich Korosov, et al., 2016 have evaluated the sea ice drift retrieval performance of dual-polarisation SAR imagery. Using a combination of phase/cross correlation, Komarov and Barber, 2014 found that sea ice drift information extracted from Radarsat-2 HV images can improve the drift estimates from HH polarisation in certain areas. They recommended a simple superposition of the vector fields obtained from HH and HV. Stefan Muckenhuber, Anton Andreevich Korosov, et al., 2016 developed an open-source feature-tracking algorithm based on corner detection for computationally efficient sea ice drift retrieval from Sentinel-1 SAR imagery and showed that the HV channel provided on average around four times as many feature-tracking vectors as the HH polarisation. Making use of Sentinel-1 SAR data, an operational sea ice drift product with 10 km resolution is provided by the Danish Technical University (Pedersen et al., 2015, http://www.seaice.dk/) as part of the Copernicus Marine Environment Monitoring Service (CMEMS, http://marine.copernicus.eu). S. Muckenhuber and S. Sandven, 2017 continued the work from Stefan Muckenhuber, Anton Andreevich Korosov, et al., 2016 and improved the feature-tracking approach by combining it with pattern-matching to derive drift vectors at user defined locations in a computationally efficient manner. Unlike Berg and Eriksson, 2014, the feature-tracking step is performed initially and serves as a first guess to limit the computational effort of the pattern-matching step.

3 SUMMARY OF PUBLICATIONS

3.1 PUBLICATION I

Stefan Muckenhuber[1], Frank Nilsen[2,3] , Anton Korosov[1] and Stein Sandven[1]: Sea ice cover in Isfjorden and Hornsund, Svalbard (2000–2014) from remote sensing data, The Cryosphere, 10, 149-158, doi:10.5194/tc-10-149-2016, 2016

To study local sea ice cover in two Arctic fjords, Isfjorden and Hornsund, the authors established a satellite database and produced corresponding sea ice classification maps. Around 17000 SAR, VIS/IR satellite images and ice charts were collected to display the area of Isfjorden, Hornsund, and the Svalbard region during winter and spring for the time period 2000-2014. More than 3300 manual interpretations of sea ice conditions in the two considered fjords have been conducted, resulting in two time series with almost daily resolution dividing the fjord area into fast ice (sea ice attached to the coastline), drift ice and open water. The sea ice time series complement the operationally provided ice charts from the Norwegian Meteorological Institute and products from automatic algorithms by providing a higher resolution, and hereby a reliable ice cover estimate for the fjord area, and distinguishing between fast and drift ice. To quantify sea ice coverage in a defined region over a certain period of time, a new index called 'days of fast ice' (DFI) has been introduced that includes both spatial and temporal extent of the fast ice coverage. The DFI values are calculated by building the sum over the fast ice area of all considered days relative to the total area. Based on the sea ice cover time series, DFI values for Isfjorden and Hornsund have been calculated for each winter season. A significant reduction of fast ice coverage is found when comparing the time periods 2000-2005 and 2006-2014 both in the monthly averaged and the DFI values. Calculating a mean before and after 2006 yields a decrease from 50 to 22 DFI for Isfjorden and from 56 to 34 DFI for Hornsund. Quantifying sea ice coverage with a single DFI value per year allows for simple comparison with other data and the authors relate the DFI values to sea surface temperature from satellite measurements, surface temperature from weather stations and ocean heat content from CTD data.

1 Nansen Environmental and Remote Sensing Center (NERSC), Thormøhlensgate 47, 5006 Bergen, Norway
2 University Centre in Svalbard (UNIS), P.O. Box 156, 9171 Longyearbyen, Norway
3 Geophysical Institute, University of Bergen, P.O. Box 7800, 5020 Bergen, Norway

3.2 PUBLICATION II

Natalia Zakhvatkina[4,5], Anton Korosov[1], Stefan Muckenhuber[1], Stein Sandven[1], Mohamed Babiker[1]: Operational algorithm for ice/water classification on dual-polarized RADARSAT-2 images, The Cryosphere, 11, 33-46, doi:10.5194/tc-11-33-2017, 2017

The authors developed an automatic sea ice/water classification algorithm for dual polarisation Radarsat-2 SAR imagery that has been applied operationally in the period 2013 until 2015. Technical issues inherent in Radarsat-2 data were addressed in a pre-processing step by introducing an angular correction procedure for the HH channel and a thermal noise removal method for HV. The algorithm calculates grey level co-occurrence matrices (GLCMs) from a sliding window with size 3.2 km $\times$ 3.2 km, that shall capture the textural characteristics inside the window. Based on the GLCM, a number of different texture features are derived. A support vector machine classification algorithm has been trained using 24 Radarsat-2 images acquired during winter, to distinguish sea ice from open water based on texture feature and backscatter values. The algorithm is already set up to define several sea ice and open water classes, but these subclasses were merged into the main classes sea ice and open water to increase the reliability of the algorithm. Automatically produced sea ice charts of the ice-covered sea between Greenland and Franz Josef Land have been distributed as open-source product from 2013 until 2015. To evaluate the accuracy of the algorithm, the results have been compared to manually derived ice charts from the Norwegian Meteorological Institute. The validation of around 2700 automatically derived ice charts from SAR showed that the average classification accuracy was 91 ± 4 %. The algorithm performed better during winter months and had a stronger deviation from the manual ice charts during summer.

4 Nansen International Environmental and Remote Sensing Centre (NIERSC), 14th Line 7, Office 49, Vasilievsky Island, St. Petersburg, 199034, Russian Federation

5 Arctic and Antarctic Research Institute (AARI), Beringstr. 38, St. Petersburg, 199397, Russian Federation

3.3 PUBLICATION III

Stefan Muckenhuber[1], Anton Korosov[1] and Stein Sandven[1]: Open-source feature-tracking algorithm for sea ice drift retrieval from Sentinel-1 SAR imagery, The Cryosphere, 10, 913-925, doi:10.5194/tc-10-913-2016, 2016

To derive high resolution sea ice motion from consecutive SAR images in a computational efficient manner and independent of rotation, the authors introduce a drift algorithm for Sentinel-1 data based on the feature-tracking algorithm ORB (Oriented FAST and Rotated BRIEF). ORB builds on the FAST keypoint detector and the binary BRIEF descriptor with many modifications to enhance the performance. The FAST detector is used to find keypoints on several resolution pyramid levels and the Harris corner measure is applied to pick the best among them. To achieve rotation invariance, the orientation of the keypoint is calculated by using the intensity-weighted centroid of a circular patch with the located keypoint at the centre. To describe the area around the keypoints, i.e. the features, the binary BRIEF descriptor is applied. The Hamming distance in combination with a brute-force procedure is used to match the features from the first and second SAR scene. The authors tuned the parameters of the algorithm for optimal SAR sea ice drift application and provided the most suitable parameter set (including spatial resolution of SAR image, patch size of FAST descriptor, number of pyramid levels, scale factor, etc.) for the area of interest, i.e. the ice-covered seas between Greenland and Severnaya Zemlya. Using 43 test image pairs over Fram Strait, the presented drift algorithm was compared to two other available feature-tracking algorithms, i.e. SIFT and SURF, and showed the best performance both in processing time and in quantity and quality of the drift vectors. To assess the accuracy of the algorithm, calculated vectors have been compared to 350 manually derived displacements vectors and the root mean square distance was found to be 563 m.

3.4 PUBLICATION IV

Stefan Muckenhuber[1] and Stein Sandven[1]: Open-source sea ice drift algorithm for Sentinel-1 SAR imagery using a combination of feature tracking and pattern matching, The Cryosphere, 11, 1835-1850, doi:10.5194/tc-11-1835-2017, 2017

The authors introduce a sea ice drift algorithm for Sentinel-1 data that shall combine the advantages from feature-tacking and patter-matching in the most meaningful way. The main advantages of the considered feature-tracking approach are the computational efficiency and the independence of the vectors in terms of position, lengths, direction and rotation. Pattern-matching on the other side allows better control over vector positioning and resolution. A feature-tracking procedure based on the algorithm from Publication III provides an un-evenly distributed vector field. Outliers in this vector field are excluded using drift and rotation estimates derived from least squares solutions. Based on the filtered feature-tracking vectors, drift and rotation on the entire SAR scene are estimated. This initial drift field limits the search area for a consecutive pattern-matching algorithm that provides small to medium scale adjustments. The resolution of the final drift product is mainly affected by the size of the pattern-matching template (2.7 km $\times$ 2.7 km), i.e. the considered area that is tracked from one image to the next. The vector spacing can be defined by the user. Considering 4 km vector spacing, the algorithm needs about 4 min when applied on a regular laptop. To assess the potential performance of the algorithm after finding suitable search restrictions, the authors compare the results from 246 Sentinel-1 image pairs to buoy GPS data collected in winter/spring 2015 north of Svalbard. A logarithmic normal distribution of the displacement difference was found with a median at 352.9 m using HV polarisation and 535.7 m using HH polarisation.

4 DISCUSSION AND OUTLOOK

The focus of this thesis is put on the development and application of methods for deriving high resolution sea ice information from space borne SAR imagery, in particular, manual and automatic sea ice classification and sea ice drift retrieval from consecutive SAR images.

Combining manual interpretation with an efficient processing chain, it has been shown that detailed sea ice information for small fjords like Isfjorden and Hornsund can be derived from SAR imagery on a daily basis with high accuracy. These efforts complement the operationally provided ice charts and products from automatic algorithms by providing a higher resolution and distinguishing between fast and drift ice. Together with constructed time series and ongoing hydrographic measurement programs the sea ice time series supports the hypothesis that the fjord systems along west Spitsbergen went from an Arctic state to a more Atlantic water state after winter 2006. The provided time series is meant to be used in future studies for a better understanding of the air-ice-ocean interaction processes in an Arctic fjord system, but also in climate effect studies linked to, e.g. glacier dynamics, ocean chemistry, and marine biology.

Using the introduced sea ice/open water algorithm, operational sea ice charts could be provided fully automatically based on dual polarisation Radarsat-2 SAR imagery with an accuracy of more than 90 %. The study emphasises the advantages of using dual polarisation mode for discriminating sea ice and open water compared to single polarisation and introduces pre-processing steps for both HH and HV that can be beneficial for other SAR applications as well. Since the start of the Sentinel-1 mission, ESA provided less Radarsat-2 imagery for non commercial purpose and the sea ice/water algorithm needed to be adapted to the data format of Sentinel-1. Ongoing work at NERSC includes the development of an automatic sea ice classification algorithm for Sentinel-1 that is also based on a support vector machine approach, but includes several modifications to enhance the performance. Instead of considering a rectangular window, as done in the Radarsar-2 algorithm, texture features are calculated for before defined segments. Classifying segments shall improve the resolution and allow a better separation of different ice and open water classes. A principal components analysis is applied to identify the most suitable set of texture features. In addition, ongoing efforts at NERSC to improve the thermal noise removal from Sentinel-1 HV imagery will improve both automatic sea ice classification as well as sea ice drift retrieval.

The developed feature-tracking algorithm showed that high resolution sea ice motion can be derived automatically from Sentinel-1 imagery in a computational efficient manner with vectors that are independent in terms of position, lengths, direction and rotation. The HV channel provided significantly more vectors than the HH channel, in particular for image pairs with larger time gaps, suggesting that the HV image depicts more features that

are better preserved over time. The major drawback of feature-tracking is that the vector positioning is not user controlled and large gaps may occur between clouds of densely located vectors. To overcome this problem, a combined algorithm has been developed that is designed to utilise the respective advantages of feature-tracking and pattern-matching to allow computational efficient sea ice drift calculation at user defined locations including a quality measure for each individual drift vector.

This combined algorithm allows to proceed to the next step towards providing large drift data-sets and developing an operational sea ice drift product that is distributed in near-real-time with a resolution of order 1 km. Therefore, the algorithm performance needs to be tested on large SAR data-sets to further evaluate weaknesses and strengths, and implemented in an infrastructure that allows near-real-time processing and distribution of the results. The necessary expertise to continue these plans and access to a super-computing and near-real-time infrastructure will be provided through an ongoing cooperation with the remote sensing group at TU Wien. The combined sea ice drift algorithm will be implemented into the SAR processing structure of TU Wien and applied on large SAR data-sets to evaluate its performance. The drift algorithm will be improved and adjusted according to the results to achieve a stable algorithm that performs well in different ice conditions. The final goal is a fully automated near-real-time distribution of high-resolution sea ice drift maps from Sentinel-1 data and providing large drift data-sets. The results shall be automatically evaluated via buoy comparison to estimate the accuracy of the product.

Another open task is to utilise the advantage of dual polarisation with the combined drift algorithm. A simple approach would be to combine the feature-tracking vectors derived from HH and HV and produce a combined first-guess. Pattern-matching can be performed based on this combined first-guess for both HH and HV individually and the results could be compared and eventually merged into a single drift product. Having two drift estimates for the same position, from HH and HV pattern-matching respectively, would also allow to disregard vectors that disagree significantly. However, this option would increase the computational effort by two.

Furthermore, the author is currently investigating the influence of non-linear motion on sea ice displacement, as derived from satellite imagery, based on GPS-data from in-situ tracker and the FRAM-2014/15 ice drift expedition. These efforts shall help to combine drift results from satellite image pairs with different time gaps to provide useful drift information from large data-sets.

The introduced combination of feature-tracking and pattern-matching can also be applied to any other application that aims to derive displacement vectors computationally efficient from two consecutive images. The only restriction is that the considered images need to depict edges, that can be recognised as keypoints for the feature-tracking algorithm.

A long-term goal is to combine sea ice drift, including deformation, with ice type classification from SAR data to create innovative, high-resolution ice maps that can be used by a variety of stack holders in the polar regions such as sea-ice modeller, operational ice forecasting services, ice navigation,

offshore operation, climate research and environmental monitoring including tracking of pollution embedded in sea ice.

A | PUBLICATION I

SEA ICE COVER IN ISFJORDEN AND HORNSUND, SVALBARD (2000–2014) FROM REMOTE SENSING DATA

Stefan Muckenhuber[1], Frank Nilsen[2,3] , Anton Korosov[1] and Stein Sandven[1]

1 Nansen Environmental and Remote Sensing Center (NERSC), Thormøhlensgate 47, 5006 Bergen, Norway
2 University Centre in Svalbard (UNIS), P.O. Box 156, 9171 Longyearbyen, Norway
3 Geophysical Institute, University of Bergen, P.O. Box 7800, 5020 Bergen, Norway

The Cryosphere, 10, 149–158, 2016
www.the-cryosphere.net/10/149/2016/
doi:10.5194/tc-10-149-2016

The Cryosphere Open Access EGU

Sea ice cover in Isfjorden and Hornsund, Svalbard (2000–2014) from remote sensing data

S. Muckenhuber[1], **F. Nilsen**[2,3], **A. Korosov**[1], **and S. Sandven**[1]

[1]Nansen Environmental and Remote Sensing Center (NERSC), Thormøhlensgate 47, 5006 Bergen, Norway
[2]University Centre in Svalbard (UNIS), P.O. Box 156, 9171 Longyearbyen, Norway
[3]Geophysical Institute, University of Bergen, P.O. Box 7800, 5020 Bergen, Norway

Correspondence to: S. Muckenhuber (stefan.muckenhuber@nersc.no)

Received: 22 June 2015 – Published in The Cryosphere Discuss.: 31 July 2015
Revised: 3 December 2015 – Accepted: 24 December 2015 – Published: 19 January 2016

Abstract. A satellite database including 16 555 satellite images and ice charts displaying the area of Isfjorden, Hornsund, and the Svalbard region has been established with focus on the time period 2000–2014. 3319 manual interpretations of sea ice conditions have been conducted, resulting in two time series dividing the area of Isfjorden and Hornsund into "fast ice" (sea ice attached to the coastline), "drift ice", and "open water". The maximum fast ice coverage of Isfjorden is $> 40\,\%$ in the periods 2000–2005 and 2009–2011 and stays $< 30\,\%$ in 2006–2008 and 2012–2014. Fast ice cover in Hornsund reaches $> 40\,\%$ in all considered years, except for 2012 and 2014, where the maximum stays $< 20\,\%$. The mean seasonal cycles of fast ice in Isfjorden and Hornsund show monthly averaged values of less than 1 % between July and November and maxima in March (Isfjorden, 35.7 %) and April (Hornsund, 42.1 %), respectively. A significant reduction of the monthly averaged fast ice coverage is found when comparing the time periods 2000–2005 and 2006–2014. The seasonal maximum decreases from 57.5 to 23.2 % in Isfjorden and from 52.6 to 35.2 % in Hornsund. A new index, called "days of fast ice" (DFI), is introduced for quantification of the interannual variation of fast ice cover, allowing for comparison between different fjords and winter seasons. Considering the time period from 1 March until end of the sea ice season, the mean DFI values for 2000–2014 are 33.1 ± 18.2 DFI (Isfjorden) and 42.9 ± 18.2 DFI (Hornsund). A distinct shift to lower DFI values is observed in 2006. Calculating a mean before and after 2006 yields a decrease from 50 to 22 DFI for Isfjorden and from 56 to 34 DFI for Hornsund. Fast ice coverage generally correlates well with remote-sensing sea surface temperature and in situ air temperature. An increase of autumn ocean heat content is observed during the last few years when the DFI values decrease. The presented sea ice time series can be utilized for various climate effect studies linked to, e.g. glacier dynamics, ocean chemistry, and marine biology.

1 Introduction

Svalbard is an Arctic archipelago located between 76 and 81° N and 10–34° E. It is surrounded by the Arctic Ocean in the north, with the Greenland Sea and Fram Strait to the west and the Barents Sea to the east. Spitsbergen is the largest island in the archipelago, and the study area of this work includes two fjords along the west coast of Spitsbergen (Fig. 1).

Water masses along the west side of Spitsbergen are strongly influenced by the West Spitsbergen Current (WSC), that is steered along the slope between the West Spitsbergen Shelf and the deep ocean, the coastal current (CC) on the shelf, and freshwater input from glacier and river runoff along the coastline (Fig. 1). The WSC transports warm and salty Atlantic water (AW) northward, representing the major oceanic heat and salt source for the Arctic Ocean. The WSC contributes strongly to Svalbard's relatively warm climate and causes the eastern Fram Strait to be the northernmost permanently ice-free ocean (Onarheim et al., 2014). The fjords along western Spitsbergen are usually separated from the WSC by the colder and fresher water masses of the northward flowing CC. This, in combination with low temperatures and fresh water input from glacier and river runoff, makes seasonal sea ice growth inside the fjords possible. But

AW from the WSC can reach the upper shelf and eventually flood into the fjords (Nilsen et al., 2008, 2012). These warm water intrusions have a strong effect on the seasonal sea ice cover inside the fjords. The fjord–shelf exchange is controlled by the density difference between the fjord water masses and the AW, which is determined by the sea ice and brine production during winter (Nilsen et al., 2008). This means that the sea ice cover inside the fjords is not only a result of advected or advecting water masses, but can alter the fjord water significantly and influence the exchange with the shelf.

The aim of this study is to investigate sea ice conditions between 2000 and 2014 in two representative fjords along the west coast of Spitsbergen (Fig. 1), where ocean and atmosphere data are available for further analysis. The two considered fjords are Isfjorden, the largest fjord of Spitsbergen with the size of 2490 km^2 (as defined from 2013 Landsat 8 images), and Hornsund, a smaller fjord (320 km^2) located in southern Spitsbergen. Both fjords reveal a seasonal sea ice coverage with strong variations between different years. Information about sea ice coverage in Isfjorden has been collected between 1974 and 2008 in Grønfjorden (Zhuravskiy et al., 2012), which is a small sub fjord at the southern entrance of Isfjorden, but no data for the entire fjord area have been published so far. Previous studies have investigated sea ice conditions in Hornsund during the winter seasons of 2005–2011, and the results have been published in Styszyńska and Kowalczyk (2007), Styszyńska and Rozwadowska (2008), Styszyńska (2009) and Kruszewski (2010, 2011, 2012). These studies compare in situ observations from the Polish Polar Station in Isbjørnhamna, a bay at the northern entrance of Hornsund, with atmospheric and oceanic measurements and mean monthly sea ice concentration at the approach to Hornsund. The survey concentrates on regional ice conditions near Isbjørnhamna and no time series for the entire fjord is given.

The data for this article were collected and interpreted within the framework of the Polish–Norwegian AWAKE-2 project. The aim of AWAKE-2 is to understand the interactions between the main components of the climate system in the Svalbard area: ocean, atmosphere, and ice, to identify mechanisms of interannual climate variability and long-term trends. The main hypothesis of AWAKE-2 is that the AW inflows over the Svalbard shelf and into the fjords have become more frequent during the last decades and this results in new regimes and changes in atmosphere, ocean, sea ice, and glaciers in Svalbard. Being a link between land and ocean, Arctic fjords are highly vulnerable to warming and are expected to exhibit the earliest environmental changes resulting from anthropogenic impacts on climate. Sea ice cover is a key parameter for monitoring climate variability and trends since it captures the variability of both ocean and atmosphere conditions. Due to the major role sea ice cover plays in air–sea interactions, knowledge about the ice cover is crucial for a better understanding of the Arctic fjord system. The focus

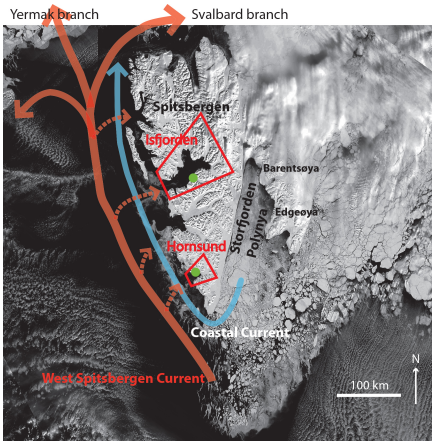

Figure 1. MODIS image of Svalbard taken on 8 April 2009 including a schematic illustration of the ocean currents along western Spitzbergen. The two considered fjords Isfjorden and Hornsund are marked with red polygons. The respective weather stations, marked with green dots, are located at 78.25° N, 15.50° E (Isfjorden) and 77.00° N, 15.54° E (Hornsund).

of this paper is to present a new sea ice cover time series, revealing the variability in sea ice cover and showing that the observed variability is consistent with other observations. Future studies may be able to use the data set to further understand linkages and drivers of the observed variability.

The paper is organized as follows: Sect. 2 explains the collected satellite images and gives an error estimate for the established sea ice cover time series. A method for manual interpretation of satellite data to describe sea ice conditions in a fjord is introduced in Sect. 3 as well as a new index, the days of fast ice (DFI) index, for quantifying fast ice coverage in a fjord. The sea ice cover time series for Isfjorden and Hornsund, the resulting DFI values and the dates for onset of freezing are presented in Sect. 4 and compared to atmosphere and ocean time series. The discussion can be found in Sect. 5.

2 Data

Investigating sea ice conditions, such as spatial extent and ice type, via satellite remote sensing in comparable small areas like Isfjorden and Hornsund requires a spatial resolution of a few 100 m or lower. Daily images throughout the year with this resolution are only produced by Synthetic Aperture Radar (SAR), which is an active microwave sensor capable of penetrating cloud cover and taking images during polar night. Since the interpretation of sea ice conditions from SAR images can be ambiguous, high and medium resolution visual/near infrared (VIS/NIR) images provide valuable ad-

ditional information during polar day. They can also be utilized, if SAR images are not available. However, good temporal coverage with VIS/NIR sensors is only achieved with a resolution above 250 m. Hence, lower accuracy is expected if only VIS/NIR images are utilized.

A satellite database including 6571 SAR images, 9123 VIS/NIR images and 861 ice charts displaying the area of Isfjorden and Hornsund has been established (see Table 1). Focus was placed on the time period 2000–2014, and the part of the season when sea ice was present in the fjords.

NERSC (Nansen Environmental and Remote Sensing Center) maintains a large satellite database including several thousand Level 1 SAR images from ASAR (Advanced Synthetic Aperture Radar on ENVISAT) and Radarsat-2. To select the images which are recorded at the considered region and time period, the NERSC MAIRES online service (http://web.nersc.no/project/maires/sadweb.py) has been used. 4326 ASAR and 2245 Radarsat-2 sub images covering Isfjorden and Hornsund, respectively, have then been created and stored in GeoTIFF format. The collected SAR data represent a time series from 2005 until 2014 with a temporal resolution of around 1–2 images per day and a spatial resolution between 50 and 150 m.

Medium resolution (300–500 m) VIS/NIR images from MERIS (Medium Resolution Imaging Spectrometer on ENVISAT) and MODIS (Moderate Resolution Imaging Spectroradiometer on Terra and Aqua) covering the Svalbard region have been downloaded from websites hosted by NASA (National Aeronautics and Space Administration). MODIS images from the data sets MOD02HKM (Terra) and MYD02HKM (Aqua) can be ordered pre-processed, which allows all available images of the considered area and time period to be downloaded. A total of 8501 MODIS images represents a temporal resolution of up to several images per day for the period 2000 until 2014. The relevant MERIS images had to be chosen prior to downloading via online "quicklooks" to select images with cloud-free conditions. About 10 MERIS images per year have been chosen and added to the database.

High resolution VIS/NIR images have a distinct lower spatial and temporal coverage, but when available, view the ice conditions with an unmistakable clarity. 335 images from Landsat 1–8 and 161 from ASTER (Advanced Spaceborne Thermal Emission and Reflection Radiometer on Terra) have been chosen for downloading via quicklooks provided by USGS (United States Geological Survey) and the Japan Space System.

In addition to the satellite images, 861 ice charts from the Norwegian Meteorological Institute (met.no) have been added to the database. These ice charts are based on the same satellite images that are used for this paper. The resolution of the met.no ice charts is too low to give sufficient accurate estimates about daily ice conditions in fjords like Isfjorden and Hornsund. Nevertheless, the met.no charts can serve as additional information about the overall sea ice concentration outside the boundary of the high resolution SAR image. Most of the stored ice charts depict ice conditions during polar night when no visual images are available to obtain a quick overview of the large scale sea ice concentration.

To validate and discuss the remote sensing sea ice observations, in situ air, ocean and remote sensing sea surface temperature (SST) data are considered. Monthly SST values are provided by the ESA (European Space Agency) for the time period 1993–2010 with a grid spacing of 25 km × 25 km (http://catalogue.ceda.ac.uk/uuid/1dc189bbf94209b48ed446c0e9a078af, doi:10.1002/gdj3.20). This data set is used to calculate winter SST for Isfjorden, representing the mean January–April at 78.25° N, 14.75° E. Moreover, 285 CTD (conductivity, temperature, and depth) profiles taken between 2000 and 2014 at the Isfjorden mouth area (78.08–78.16° N, 13.5–14.3° E) and 107 CTD profiles taken between 2009 and 2014 inside Hornsund have been used to calculate the mean heat content of the 25–100 m depth water column for each year during autumn (July–September). The 25–100 m depth range was chosen in order to avoid the shallow atmospheric heated surface layer and rather concentrate on the layers that represent fjord circulation of either Atlantic water (AW) or Arctic water (ArW). The CTD data were extracted from the UNIS (University Centre in Svalbard) hydrographic database (UNIS HD), where the CTD profiles used in this study are mainly collected by UNIS with additional profiles from the Norwegian Marine Data Centre (NMDC). Air temperature measurements from weather stations in Isfjorden (Svalbard airport, 78.25° N, 15.50° E) and Hornsund (77.00° N, 15.54° E) are provided by the Norwegian meteorological institute (eklima.met.no) for the entire observation period. The temperatures of days with average temperature below −2 °C between October and May are added together to derive negative degree days for each winter.

Continuity of the presented sea ice time series is expected since VIS/NIR images from the same sensor are considered for the entire observation period. Including SAR as additional data source for the time period 2005–2014 provides useful data during cloud cover and leads to an increased temporal resolution compared to the period prior to 2005, which is solely based on visible data. Visible images are not able to capture sudden sea ice condition changes, if the fjord is covered by clouds. However, complete cloud cover usually did not exceed a few days. The formation and melting of sea ice takes place over time scales of days, but sea ice advection from or into the fjord and break up of fast ice can happen within a few hours. These sudden changes are captured in the time series prior to 2005 on the first succeeding day with little or no cloud cover.

Table 1. Satellite databases used, including sensor, image type, spatial resolution (i.e. pixel size), amount of collected images, covered time span (i.e. date of first and last image) and source.

Sensor	Image type	Resolution	# of images	Time span	Source
ASAR	SAR	150 m	4326	21 Jul 2005–7 Apr 2012	NERSC database
ASTER	VIS/NIR	15 m	161	19 Aug 2000–12 Aug 2013	http://gds.ersdac.jspacesystems.or.jp
Landsat 1–8	VIS/NIR	15 m	335	25 Mar 1973–29 Jul 2014	http://earthexplorer.usgs.gov
MERIS	VIS/NIR	300 m	126	25 Jun 2003–7 Apr 2012	http://oceancolor.gsfc.nasa.gov
MODIS	VIS/NIR	500 m	8501	25 Feb 2000–4 Aug 2014	http://ladsweb.nascom.nasa.gov
Radarsat 2	SAR	50 m	2245	5 Apr 2011–30 Jul 2014	NERSC database
met.no	ice chart	–	861	24 Oct 2005–27 Jun 2014	http://polarview.met.no

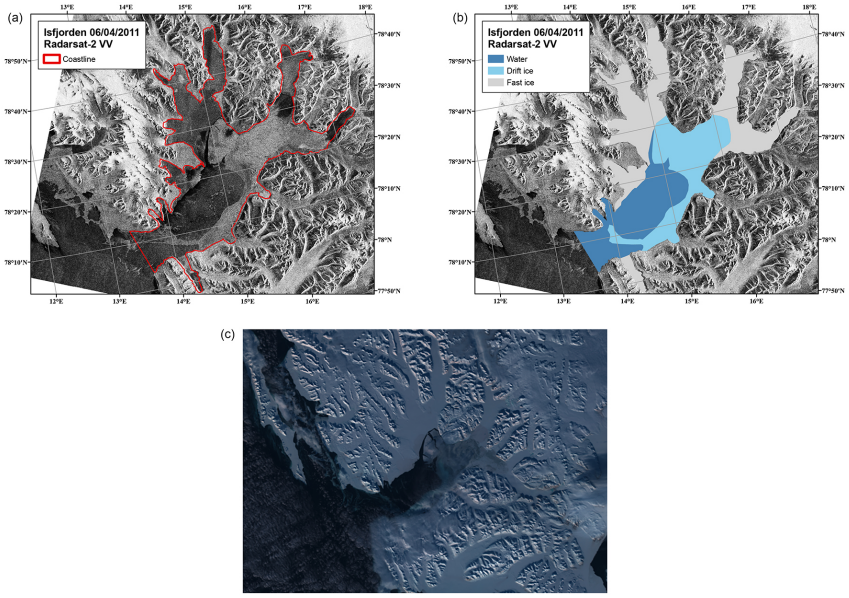

Figure 2. Radarsat-2 **(a,b)** and MERIS **(c)** images of Isfjorden taken on 6 April 2011. Radarsat-2 images are shown in ArcGIS with adjusted symbology **(a)** before and **(b)** after analysis by a sea ice expert.

3 Methods

The downloaded Level 1 satellite data from ASAR, Radarsat-2, MODIS, and MERIS were processed with the open-source python toolbox "Nansat" (developed by NERSC) into geoTIFF and PNG Level 2 images, which can be displayed by ArcGIS and several other programs. Within ArcGIS, two polygons covering Isfjorden and Hornsund were created using a high resolution VIS/NIR image from Landsat 8 as reference. This polygon describes the fjord area very accurately and can be subdivided in order to evaluate the sea ice coverage by area. Due to the large amount of considered days and images, the processing chain needed to be fast and efficient. This was achieved by implementing most steps into a python code working inside ArcGIS.

For the time period 2005–2014, both SAR and VIS/NIR images are available, and the processing chain for a specific date (leading to one data point in the time series) is as follows. The SAR images of the considered day are loaded into ArcGIS, and their symbology is adjusted to increase the visual difference between water and ice. Then the mentioned polygon is superimposed on the images and divided by a sea ice expert into the regions "fast ice", "drift ice", and "open water" (Fig. 2a, b). Both "fast ice" and "drift ice" appear white on the visible image and are characterized by high backscatter values on the SAR image. "Open water" appears dark blue on the visible image and has low/high SAR

backscatter values during low/high wind speeds. "Fast ice" is attached to the coastline and does not change its position on consecutive SAR images. This makes it easy to identify "fast ice", but the difference between "drift ice" and "open water" can be ambiguous during high wind speeds, if only SAR data are available. The origin of the sea ice, which can result from both freezing inside the fjord or advection from the shelf, is not considered during the manual interpretation. The area of each region is calculated in m^2 using a built in function of ArcGIS, and the results are saved in a text file. In case VIS/NIR images are available for the same date, they are used for validation and interpretation support of the SAR images (Fig. 2c).

Prior to 2005, no high quality SAR images could be accessed, and the time series is solely based on VIS/NIR images. During polar night it is therefore not possible to describe the ice conditions. During polar day high accuracy is only achieved for days with high resolution VIS/NIR images and lower accuracy is expected for the other days, due to the lower resolution of MODIS and MERIS compared to SAR. The method yields still high reliability for the analyzed years before 2005 since water and ice can be separated unmistakably on visual images. Continuity of the time series is expected since MODIS, Aster, and Landsat data are available and considered for the entire time series.

3.1 Days of fast ice (DFI)

To quantify sea ice coverage in a defined region (in our case Isfjorden and Hornsund), a new index called "days of fast ice" (DFI) is introduced. The index describes fast ice conditions over a considered time period in a single value with unit days. Both temporal and spatial extent of the fast ice is included. The DFI are calculated by building the sum over the fast ice area of all considered days relative to the total area, i.e. in our case the entire fjord area (Eq. 1).

$$\mathrm{DFI} = \sum_{\mathrm{days}} \frac{\text{fast ice area}}{\text{total area}} \tag{1}$$

The unit days shall give a quick understanding of the range (considered time period) and linear scaling. The index indicates the number of days that the fjord would be covered 100 % with fast ice. The DFI values allow a simple comparison between different regions and time periods as well as with external parameters like atmospheric or oceanic data.

3.2 Error estimates

Since the time series is based on manual interpretation, defining an exact error value for spatial sea ice extent is not possible. Nevertheless, possible error sources can be evaluated and an error estimate from the analyzing sea ice expert can be given.

The biggest error source is wrong interpretation of ambiguous SAR images during polar night, when no visible images are available for validation. As mentioned above, "fast ice" is easy to identify, whereas the separation of "drift ice" and "open water" is sometimes inconclusive. This error for "drift ice" and "open water" is hard to quantify, but can be up to 10 % and in some cases even more.

The different resolutions of the utilized satellite images is another potential source of error. In our study, the areas covered by "fast ice", "drift ice", and "open water" do not vary randomly from pixel to pixel, but are usually divided by defined edges. Using different resolutions should not affect the classification of a certain region but only the accuracy of the edge position in the order of one pixel. Hence, a relative error estimate can be given by multiplying the edge length with the pixel size and dividing the result by the fjord area. Assuming an edge of 20 km and 7 km, which is about the fjord width of Isfjorden and Hornsund, and a resolution range of 15 m (Landsat, ASTER) to 500 m (MODIS), the resulting error range is 0.01–0.4 % for Isfjorden and 0.03–1 % for Hornsund.

Insufficient geographic information for the satellite image can lead to a slightly stretched satellite image compared to the fjord polygon in the order of a few pixels. This can lead to an additional error of the same order of magnitude as the discussed resolution error, but only a small number of the satellite images are affected by that.

The observed glacier retreat has a negligible effect on larger fjords like Isfjorden, but can change the total area of smaller fjords like Hornsund on the order of 0.5 % per year. Blaszczyk et al. (2013) quantified the total glacier retreat area at the marine margin in Hornsund to be 18.8 km^2 between 2001 and 2010 (equal to 5.8 % of the fjord area measured in 2013). The utilized Hornsund coastline was created using a Landsat image from 2013, meaning that the coastline represents the fjord area very well during the later years, but overestimates the total fjord area during the first few years in the order of up to 5 %. The glacier covered area along the coastline polygon was not classified separately but added to the surface coverage at the glacier front. This might lead to a slight overestimation of the surface type next to the glacier front, which is most likely "fast ice" during winter. The resulting error is negligible for the second half of the time series and in the order of 0–1 % for the first half.

The daily error estimate based on consideration of the mentioned sources and personal appraisal of the analyzing sea ice expert is in the order of 1 % for "fast ice" and between 1 % up to 10 % for "drift ice" and "open water" depending on the availability of VIS/NIR images for validation. The error propagation from a single day to a time period of several months leads to a very high accuracy for all given monthly averaged fast ice cover and days of fast ice (DFI) values. The error of these values are therefore not considered in the following since they do not influence the interpretation of the results.

Table 2. Calculated "days of fast ice" (DFI) for Isfjorden and Hornsund between 2000 and 2014 for two different time periods. "Total season" refers to the entire sea ice season starting during autumn of the previous year and "short season" refers to 1 March until the end of the ice season, i.e. the time period when VIS/NIR images are available. **Δ** describes the difference between the entire and short season.

(DFI)	Isfjorden			Hornsund		
Year	Total season	Short season	Δ	Total season	Short season	Δ
2000	–	46.0		–	56.7	
2001	–	33.8		–	54.3	
2002	–	52.2		–	53.6	
2003	–	43.1		–	53.5	
2004	–	70.7		–	59.9	
2005	–	55.4		–	56.0	
2006	19.4	9.5	9.9	25.8	25.8	0
2007	19.3	14.1	5.2	51.1	40.1	11
2008	28.5	20.5	8	54.2	49.8	4.4
2009	61.6	49.8	11.8	71.4	51.4	20
2010	34.9	24.8	10.1	53.6	47.4	6.2
2011	68.7	32.2	36.5	76.1	44.9	31.2
2012	16.9	12.8	4.1	2.5	2.0	0.5
2013	22.7	19.0	3.7	49.9	47.0	2.9
2014	18.0	13.2	4.8	2.5	0.4	2.1
Mean ± SD	32.2 ± 18.5	33.1 ± 18.2	10.5 ± 9.6	43.0 ± 25.5	42.9 ± 18.2	8.7 ± 9.9

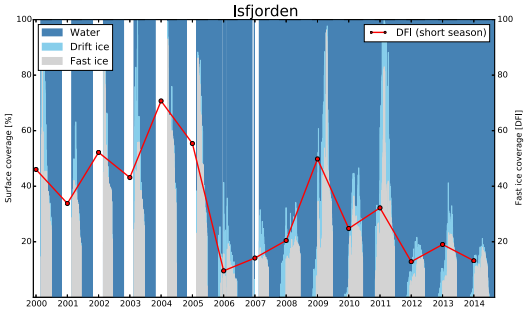

Figure 3. Surface coverage of Isfjorden between 2000 and 2014 divided into "fast ice", "drift ice", and "open water" by a sea ice expert. Total area = 2487.6 km^2 (defined with Landsat image from 19 September 2013). White gaps occur when no satellite data were available. The red dots display the "days of fast ice" (DFI) values of the short season as shown in Table 2.

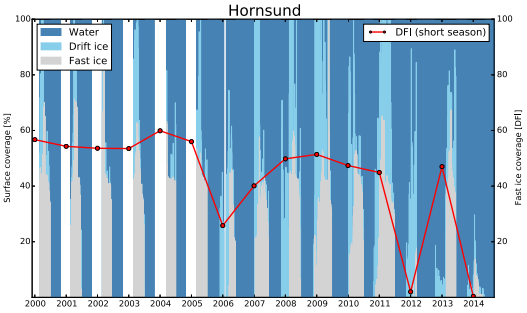

Figure 4. Surface coverage of Hornsund between 2000 and 2014 divided into "fast ice", "drift ice", and "open water" by a sea ice expert. Total area = 324.0 km^2 (defined with Landsat image from 24 August 2013). White gaps occur when no satellite data were available. The red dots display the "days of fast ice" (DFI) values of the short season as shown in Table 2.

4 Results

By utilizing the created satellite database (Sect. 2) and applying the described method (Sect. 3), two time series dividing the area of Isfjorden and Hornsund into "fast ice", "drift ice", and "open water" have been created (Figs. 3 and 4). In total, 3319 manual interpretations of sea ice conditions were conducted by a sea ice expert, leading to an almost daily resolution between 2000 and 2014. Unclassified gaps occur in both time series when SAR images were unavailable during the dark season (white gaps in Figs. 3 and 4).

The daily surface coverage in Isfjorden between 2000 and 2014 is shown in Fig. 3. A maximum fast ice coverage of 40 % and higher is reached in the time periods 2000–2005 and 2009–2011. During the periods 2006–2008 and 2012–2014, the fast ice area stays always below 30 %. Figure 4 displays the daily surface coverage in Hornsund for 2000 until 2014. Maximum fast ice cover values above 40 % are reached in all years, except for 2012 and 2014, where the fast ice season is significantly shorter and the maximum stays below 20 %. Late growth of fast ice is also observed in 2006, 2008 and 2013.

Monthly averaged fast ice cover, based on the time series shown in Figs. 3 and 4, are shown in Figs. 5 and 6, respectively. The monthly averaged values display the seasonal cycle of fast ice growth and melt/break up in Isfjorden and Hornsund. Values for the dark season (November–February)

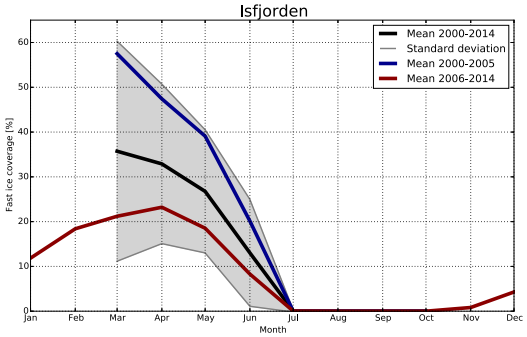

Figure 5. Monthly averaged fast ice coverage in Isfjorden shown for three time periods: 2000–2014 (mean in black and standard deviation in grey) 2000–2005 (blue) and 2006–2014 (red).

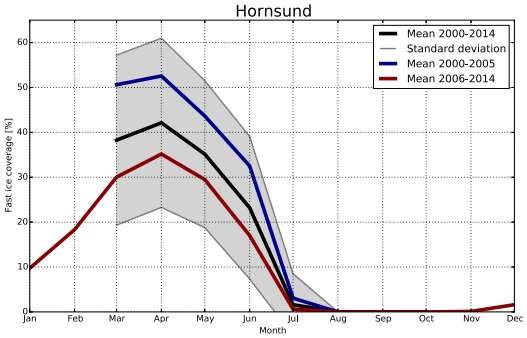

Figure 6. Monthly averaged fast ice coverage in Hornsund shown for three time periods: 2000–2014 (mean in black and standard deviation in grey) 2000–2005 (blue) and 2006–2014 (red).

before 2006 are missing since no high quality SAR images were available for this period.

Less than 1 % monthly averaged fast ice cover were observed in Isfjorden between July and November (Fig. 5). Considering the mean over the entire observation period 2000–2014 (black line, Fig. 5), the highest value is reached in March (35.7 %) or earlier. Before 2005 (blue line, Fig. 5), the value in March is 57.5 %. The mean for 2006–2014 (red line, Fig. 5) shows the highest value with 23.2 % in April. Monthly averaged fast ice coverage in Hornsund is shown in Fig. 6. Less than 2 % fast ice is observed between July and November. April is the month with the highest fast ice coverage values: 42.1 % for the mean over all considered years (black line, Fig. 6), 52.6 % for the period 2000–2005 (blue line, Fig. 6) and 35.2 % for 2006–2014 (red line, Fig. 6). Comparing the time periods 2000–2005 and 2006–2014 yields a significant reduction of the monthly averaged fast ice coverage. The seasonal maximum decreases by 60.2 and 33.1 %

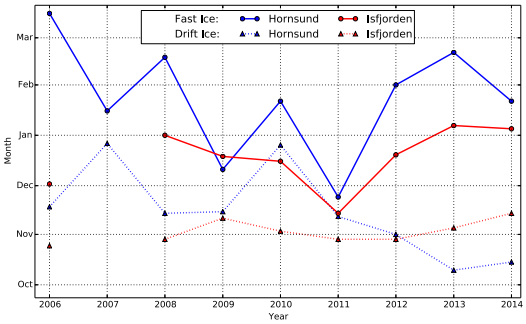

Figure 7. Onset of sea ice cover in Isfjorden and Hornsund. The years refer to the sea ice season, which starts during the previous year, meaning that January marks the beginning of the respective year. The triangles and dots mark the days with first appearance of drift and fast ice, i.e. the start of the sea ice season. Too few satellite images were available for Isfjorden in 2007 to give a reliable estimate.

(relative to the value for 2000–2005, assuming the maximum occurs in March) in Isfjorden and Hornsund, respectively.

4.1 Days of fast ice (DFI)

Utilizing Eq. (1) and the time series shown in Figs. 3 and 4, DFI values have been calculated for Isfjorden and Hornsund, and the results are shown in Table 2. For each sea ice season, two different time periods were considered. The "total season" refers to the entire sea ice season, which lasts usually from November of the previous year until June, and the "short season" lasts from 1 March until the end of the sea ice season. The "short season" can also be calculated for years in which only VIS/NIR images are available, whereas SAR images are necessary for the "total season".

High correlation coefficients (R) between the total and short season DFI time series for both Isfjorden ($R = 0.89$) and Hornsund ($R = 0.94$) suggest that the short season values effectively capture the interannual variability of the entire season. Only the ice season 2011 shows a higher than average difference in the short and total season DFI values (Table 2), due to very early fast ice growth (Fig. 7) and a high fast ice peak before March.

The DFI mean values (total and short season, Table 2) for Isfjorden are around 10 DFI lower than the mean values for Hornsund, which means around 25 % less fast ice coverage in Isfjorden relative to the total area of each fjord. Similar high standard deviations for both fjords indicate strong variations from year to year.

Both "short season" time series show a strong decrease in 2006. Isfjorden's DFI values between 2000 and 2005 are all above the mean, whereas after 2006 only 2009 has more than the average "days of fast ice". Calculating a mean before and

after 2006 shows a drop from 50 to 22 DFI. The situation of Hornsund is similar, yet not so pronounced. The mean value decreases from 56 to 34 DFI before and after 2006. Low values are reached in 2006 and particularly in 2012 and 2014, where the fast ice coverage goes down to almost 0 DFI.

4.2 Onset of freezing

The sea ice season in Isfjorden and Hornsund starts usually between late autumn and beginning of winter. Figure 7 shows the days on which drift and fast ice first appear, i.e. the start of the sea ice season in Isfjorden and Hornsund. The year refers to the winter season, which starts during the previous year. This means, that January in Fig. 7 refers to the beginning of the respective year. The first sea ice of the season appears during polar night and SAR images are necessary to define the date of the freezing onset. Since no SAR images were available prior to 2005, the time series in Fig. 7 starts with the sea ice season 2006. Too few satellite images were available to give an reliable estimate of the freezing onset in Isfjorden 2007.

Drift ice starts to grow in Isfjorden in all examined years around the beginning of November. The appearance of fast ice in Isfjorden varies between mid November (2011), December (2009, 2010, and 2012), and the beginning of January (2008, 2013, and 2014). The start of the sea ice season in Hornsund underlies stronger variations. The first drift ice of the season was found in November or December in all years except for the last 2 years, during which an early start in October was observed. Fast ice starts to appear in Hornsund between the end of November and mid March. Late fast ice formation was observed during 2006, 2008, and 2013.

4.3 Ocean and atmospheric data

In Fig. 8, the DFI values for Isfjorden are compared with satellite-derived winter sea surface temperatures (SSTs) near the mouth of the fjord, ocean heat content from in situ profiles taken at the mouth of the fjord for 25–100 m depth, as well as winter atmospheric temperatures from a nearby weather station, represented by negative degree days. Fast ice coverage generally correlates well with winter SST and air temperature. The SST time series deviate somewhat in 2003, 2004, and 2006 compared to the observed DFI values, and fast ice coverage in 2011 is relatively low considering the relatively low air temperatures. Low DFI values between 2006 and 2008 are reflected in the ocean heat content time series and a general increase of autumn ocean heat content is observed between 2010 and 2014 when the DFI values decrease.

The DFI values for Hornsund are shown together with autumn ocean heat content and winter atmospheric temperatures in Fig. 9. Except for 2001 and 2010, relatively low/high fast ice cover occurs during winters with relatively high/low air temperatures. The water masses found inside the fjord

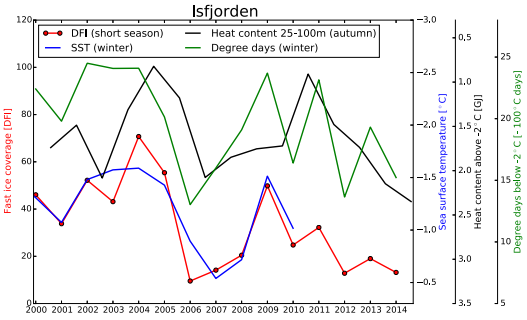

Figure 8. Isfjorden's (red) "days of fast ice" (DFI) values of the short season compared to (blue) winter sea surface temperature (SST), (black) autumn heat content above -2 °C of the 25–100 m depth water column and (green) winter negative degree days below -2 °C. Winter SST values represent the mean for the period January–April at 78.25° N, 14.75° E. Heat content values are calculated using the mean temperature profile during autumn (July–September) at the Isfjorden mouth area. Negative degree days have been derived from temperature measurements at the Svalbard airport station (78.25° N, 15.50° E). Note the reversed SST and heat content axis.

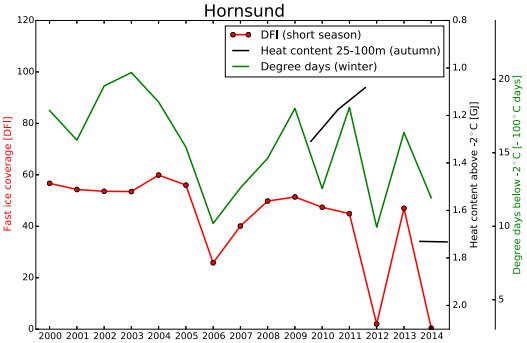

Figure 9. Hornsund's (red) "days of fast ice" (DFI) values of the short season, compared to (black) autumn heat content above -2 °C of the 25–100 m depth water column and (green) winter negative degree days below -2 °C. Heat content values are calculated using the mean temperature profile inside Hornsund during autumn (July–September). Negative degree days have been derived from temperature measurements at the Hornsund station at 77.00° N, 15.54° E. Note the reversed heat content axis.

during autumn show a distinct higher heat content in 2013 and 2014 compared to 2009–2011.

5 Discussion and outlook

Isfjorden has two periods with relatively high sea ice cover (2000–2005 and 2009–2011, Fig. 3) and two periods with

relatively low sea ice cover (2006–2008 and 2012–2014, Fig. 3). All periods last 3 years or more, which suggests the involvement of an oceanic mechanism since the atmospheric conditions underlay variations with shorter time scales. However, wind forcing of the West Spitsbergen Shelf (WSS) on timescales from days to months is shown to be one of the mechanisms of starting a shelf circulation of warm AW towards the fjords (Cottier et al., 2007; Nilsen et al., 2012). Cottier et al. (2007) reported that during the Arctic winter of 2005/2006, periods of sustained along-shelf winds generated upwelling and cross-shelf exchange that caused extensive flooding of the coastal waters with warm Atlantic water from the West Spitsbergen Current (WSC) (Cottier et al., 2007). The winter temperature of the WSS reverted to that typical of fall, interrupting the normal cycle of sea ice formation in the region, including both the shelf and the fjords along the west coast of Spitsbergen.

Ongoing hydrographic measurement programs and construction of longer time series (Pavlov et al., 2013) show that fjord systems along west Spitsbergen went from an Arctic state to a more Atlantic water state after winter 2006 (Cottier et al., 2007). In Fig. 8, times series for the winter SST in Isfjorden and the autumn heat content (25–100 m depth) at the mouth of Isfjorden show that both the SST and heat content increased in the period 2006–2008. Atlantic water circulated the WSS and Isfjorden during this period (Cottier et al., 2007; Nilsen et al., 2016) and the surface water seldom reached the freezing point temperature (Fig. 8). Hence, the effect of forcing event on the time scale of weeks (Cottier et al., 2007), and a corresponding advection of AW, can have an influence on the fjord thermodynamics and local sea ice condition on a yearly time-scale. The fjord–shelf system went towards a more Arctic state during the following years, but in 2012, similar forcing events as for 2006 (Nilsen et al., 2016) caused the AW to dominate the fjords again, and the heat content in Fig. 8 shows an increasing trend after 2011. Calculated negative degree-days from atmospheric temperature data closely follows the variation in DFI (Fig. 8) and can also explain the low DFI values in some years. But care must be taken in attributing changes in sea ice cover to atmospheric variability, as reduced sea ice cover and a warmer ocean can also increase the atmospheric temperature.

Another possible explanation for the perennial duration of both small and large fast ice cover years in Isfjorden can be given by looking at the density difference between the fjord water masses and the AW. In contrast to the external forcing mechanism suggested above, this represents a local forcing mechanism through air–ice–ocean interaction. Nilsen et al. showed that a high ice production during winter, results in a higher formation of dense brine-enriched fjord water and the local water masses in the fjord proper can end up being denser than the water masses residing on the shelf (Nilsen et al., 2012). This is a key mechanism that enables AW to penetrate into Isfjorden in spring and the following summer and autumn, and determines in which depth the warm AW will circulate in the water column. Considering Isfjorden as a coastal polynya with the opening area restricted by fast ice cover, more sea ice is produced in winters with less fast ice coverage. Hence, low fast ice coverage can cause AW intrusion in the following summer, which then can lead to low fast ice coverage in the following winter if the intruding AW is circulating high in the water column.

The mechanisms described for Isfjorden could apply for Hornsund, but being a smaller fjord, the resident time for different water masses will be smaller and variations on shorter time scales can be expected. A comparison of the DFI time series in Figs. 8 and 9 suggests that interannual sea ice cover variability in Hornsund may be less influenced by intrusion of AW residing on the shelf. The sea ice cover in Hornsund seems to revert to a "normal" state after a year with known AW intrusion, while Isfjorden is influenced by the AW for several years after such events (Nilsen et al., 2008, 2016). However, Hornsund responds similarly to Isfjorden during the most extreme years of AW dominance on the WSS and strong external forcing mechanisms (Nilsen et al., 2016), i.e. the winters of 2006, 2012, and 2014. Thus, Hornsund, being the most southern fjord along the west coast of Spitsbergen, could serve as an indicator of AW dominance for all fjords north of Hornsund along the west coast. Ocean and atmosphere measurements from the Polish research station in Hornsund carried out by the ongoing Polish–Norwegian project AWAKE-2 (Arctic climate system study of ocean, sea ice and glaciers interactions in Svalbard area) will be utilized within AWAKE-2 to explain the difference between average seasons and years with distinct less sea ice coverage, i.e. 2006, 2012, and 2014.

Considering the start of the freezing season, i.e. the first appearance of drift or fast ice in the two fjords, Isfjorden shows in general less variability and earlier ice growth (Fig. 7). A low correlation between the start of the freezing season for the two fjords is observed, suggesting a stronger dependence on local conditions rather than a large-scale ocean and/or atmosphere influence. Occurrence of drift ice always precedes fast ice, often with a time lead of 1–2 months. However, care must be taken when defining the start of the freezing in Arctic fjords using satellite images since the first appearance of drift ice will not necessarily reflect that the surface layer of the fjord proper has reached the freezing point temperature, but merely that some protected side fjords within the larger fjord system may have a fresher and colder surface layer, allowing for sea ice production for a limited period. Hence, the true freezing season will start somewhere between the first detection of drift ice and the establishment of fast ice in an Arctic fjord.

Recent observations of the ice cover to the north of Svalbard further demonstrate the intimate link between the heat of the Atlantic water and the distribution of sea ice. Onarheim et al. (2014) have shown that the sea ice area north of Svalbard has been decreasing for all months since 1979 with the largest ice reduction occurring during the winter months at

a rate of 10 % per decade (Onarheim et al., 2014). This is in contrast to the observed changes in more central parts of the Arctic Ocean, where largest ice decline is happening during summer. However, the observed reduction is concurrent with a gradual warming of 0.3 °C per decade warming of the AW along West Spitsbergen, and thus, the extra oceanic heat has been the major driver of the sea ice loss, which is concurrent with our results from both Isfjorden and Hornsund. Another indication of warm water as a major driver is the delayed maximum fast ice area in Isfjorden (Fig. 5) from March (or earlier) to April for the 2000–2005 period to the 2006–2014 period, respectively. A warmer water column in late autumn can cause delayed ice formation and consequently lower ice concentrations in early winter.

In conclusion, the presented sea ice time series can be used to obtain a better understanding of interannual variability in Arctic fjord system. Since a sea ice cover reflects the physical state of the ocean and atmosphere, the present sea ice time series can be used in future studies to better understand air–ice–ocean interaction processes within each fjord system, but also in various climate effect studies linked to, e.g. glacier dynamics, ocean chemistry, and marine biology.

The Supplement related to this article is available online at doi:10.5194/tc-10-149-2016-supplement.

Acknowledgements. This research was supported by the Polish–Norwegian AWAKE-2 (Arctic climate system of ocean, sea ice and glaciers interaction in Svalbard) project (Pol-Nor/198675/17/2013). We thank the developer group of the open-source python toolbox "Nansat" (https://github.com/nansencenter/nansat) and the following agencies/institutes for providing the utilized satellite images and ice charts: National Aeronautics and Space Administration, European Space Agency, and the Canadian Space Agency and Norwegian Meteorological Institute. We would like to thank Ragnheid Skogseth (RS) for preparing and sharing CTD data from the UNIS Hydrographic Database (UNIS HD). The hydrographic data used in this paper are either collected by UNIS or extracted from public databases like The Norwegian Marine Data Centre (NMD at the imr.no). Funding for RS and the construction of the UNIS HD merits REOCIRC (Remote Sensing of Ocean Circulation and Environmental Mass Changes, a Research Council of Norway project no. 222696/F50) and GrønnBille (The Oceanography of Grønnfjorden and Billefjorden, a Research Council of Norway project nr. 227067). A special thanks to the two anonymous reviewers for valuable input that improved our paper.

Edited by: M. Tedesco

References

Blaszczyk, M., Jania, J. A., Kolondra, L.: Fluctuations of tidewater glaciers in Hornsund Fjord (Southern Svalbard) since the beginning of the 20th century, Pol. Polar Res., 34, 4, 327–352, doi:10.2478/popore-2013-0024, 2013.

Cottier, F., Nilsen, F., Inall, M. E., Gerland, S., Tverberg, V., and Svendsen, H.: Wintertime warming of an Arctic shelf in response to large-scale atmospheric circulation, Geophys. Res. Lett., 34, L10607, doi:10.1029/2007GL029948, 2007.

Kruszewski, G.: Ice condition in Hornsund (Spitsbergen) during winter season 2008–2009, Problemy Klimatologii Polarnej, 20, 187–196, 2010.

Kruszewski, G.: Ice condition in Hornsund during winter season 2009–2010 (SW Spitsbergen), Problemy Klimatologii Polarnej, 21, 229–239, 2011.

Kruszewski, G.: Ice condition in Hornsund and adjacent waters (Spitsbergen) during winter season 2010–2011, Problemy Klimatologii Polarnej, 22, 69–82, 2012.

Nilsen, F., Cottier, F., Skogseth, R., and Mattsson, S.: Fjord-shelf exchanges controlled by ice and brine production: the interannual variation of Atlantic water in Isfjorden, Svalbard, Cont. Shelf. Res., 28, 1838–1853, 2008.

Nilsen, F., Vaardal-Lunde, J., and Skogseth, R.: Topographically controlled flow on the West Spitsbergen Shelf with special emphasis on the Atlantic water transport towards Isfjorden, D:07, ICES CM, 2012.

Nilsen, F., Skogseth, R., Vaardal-Lunde, J., and Inall, M.: A simple shelf circulation model – intrusion of Atlantic water on the West Spitsbergen Shelf, J. Phys. Oceanogr., accepted, 2016.

Onarheim, I., Smedsrud, L., Ingvaldsen, R., and Nilsen, F.: Loss of sea ice during winter north of Svalbard, Tellus A, 66, 23933, doi:10.3402/tellusa.v66.23933, 2014.

Pavlov, A., Tverberg, V., Ivanov, B., Nilsen, F., Falk-Petersen, S., and Granskog, M.: Warming of Atlantic water in two West Spitsbergen fjords over the last century (1912–2009), Polar Res., 32, 11206, doi:10.3402/polar.v32i0.11206, 2013.

Styszyńska, A.: Ice condition in Hornsund and its foreshore (SW Spitsbergen) during winter season 2007/2008, Problemy Klimatologii Polarnej, 19, 247–267, 2009.

Styszyńska, A. and Kowalczyk, M.: Ice condition in Hornsund and its foreshore (SW Spitsbergen) during winter season 2005–2006, Problemy Klimatologii Polarnej, 17, 147–158, 2007.

Styszyńska, A. and Rozwadowska, A.: Ice condition in Hornsund and its foreshore (SW Spitsbergen) during winter season 2006/2007, Problemy Klimatologii Polarnej, 18, 141–160, 2008.

Zhuravskiy, D., Ivanov, B., and Pavlov, A.: Ice conditions at Grønfjorden Bay, Svalbard, from 1974 to 2008, Polar Geogr., 35, 169–176, doi:10.1080/1088937X.2012.662535, 2012.

B | PUBLICATION II

OPERATIONAL ALGORITHM FOR ICE/WATER CLASSIFICATION ON DUAL-POLARIZED RADARSAT-2 IMAGES

Natalia Zakhvatkina[1,2], Anton Korosov[3], Stefan Muckenhuber[3], Stein Sandven[3], Mohamed Babiker[3]

II

1 Nansen International Environmental and Remote Sensing Centre (NIERSC), 14th Line 7, Office 49, Vasilievsky Island, St. Petersburg, 199034, Russian Federation
2 Arctic and Antarctic Research Institute (AARI), Beringstr. 38, St. Petersburg, 199397, Russian Federation
3 Nansen Environmental and Remote Sensing Center (NERSC), Thormøhlensgate 47, 5006 Bergen, Norway

The Cryosphere, 11, 33–46, 2017
www.the-cryosphere.net/11/33/2017/
doi:10.5194/tc-11-33-2017

The Cryosphere Open Access EGU

Operational algorithm for ice–water classification on dual-polarized RADARSAT-2 images

Natalia Zakhvatkina[1,2], Anton Korosov[3], Stefan Muckenhuber[3], Stein Sandven[3], and Mohamed Babiker[3]

[1]Nansen International Environmental and Remote Sensing Centre (Nansen Centre, NIERSC), 14th Line 7, Office 49, Vasilievsky Island, St. Petersburg, 199034, Russian Federation
[2]Arctic and Antarctic Research Institute (AARI), Bering Str. 38, St. Petersburg, 199397, Russian Federation
[3]Nansen Environmental and Remote Sensing Center (NERSC), Thormøhlensgate 47, 5006 Bergen, Norway

Correspondence to: Natalia Zakhvatkina (natalia.piotrovskaya@niersc.spb.ru)

Received: 30 May 2016 – Published in The Cryosphere Discuss.: 21 June 2016
Revised: 23 October 2016 – Accepted: 6 December 2016 – Published: 11 January 2017

Abstract. Synthetic Aperture Radar (SAR) data from RADARSAT-2 (RS2) in dual-polarization mode provide additional information for discriminating sea ice and open water compared to single-polarization data. We have developed an automatic algorithm based on dual-polarized RS2 SAR images to distinguish open water (rough and calm) and sea ice. Several technical issues inherent in RS2 data were solved in the pre-processing stage, including thermal noise reduction in HV polarization and correction of angular backscatter dependency in HH polarization. Texture features were explored and used in addition to supervised image classification based on the support vector machines (SVM) approach. The study was conducted in the ice-covered area between Greenland and Franz Josef Land. The algorithm has been trained using 24 RS2 scenes acquired in winter months in 2011 and 2012, and the results were validated against manually derived ice charts of the Norwegian Meteorological Institute. The algorithm was applied on a total of 2705 RS2 scenes obtained from 2013 to 2015, and the validation results showed that the average classification accuracy was $91 \pm 4\,\%$.

1 Introduction

Synthetic Aperture Radar (SAR) is an active microwave sensor providing high-resolution images over large areas independent of clouds and daylight. This is especially useful for observing the polar regions, where SAR data are widely used for exploring sea ice concentration, extent, detection of leads, polynyas, ice floes and ice edge, and ice type identification and classification (Johannessen et al., 2007; Dierking, 2013). Monitoring of sea ice processes, i.e., ice edge variations and motion, is important for practical tasks such as ice navigation and for scientific studies. High-resolution data from C-band SAR such as ERS-1/2 (European Remote Sensing satellites, European Space Agency, ESA), RADARSAT-1 (Earth observation satellite, Canadian Space Agency), and ENVISAT (Environmental Satellite, ESA) have been used as the main data source for sea ice monitoring in the last 2 decades (e.g., Johannessen et al., 2007). The advanced capabilities of SAR on board of RADARSAT-2 (RS2) and Sentinel-1 (European Commission and ESA) with multi-polarization data can improve sea ice observations such as ice edge detection and ice type classification.

SAR images can be used to identify different sea ice types and open water (OW) areas based on variations of the backscattered radar intensity caused by surface roughness and other sea ice properties. Classification methods based only on the backscattering coefficients (σ°) are hampered by ambiguities in the relation between ice types and σ°, since various ice types (multiyear, first-year, and some young and new ice) and open water depending on wind speed and direction can have similar σ° (Dierking, 2010; Johannessen et al., 2007). In particular, discrimination between calm open water and smooth first-year ice, as well as between windy open water and young ice with frost flowers or multiyear ice, can be problematic. Including additional image characteristics like image texture, tone, and spatial structures can improve the classification results significantly (Shokr, 1991; Soh and

Tsatsoulis, 1999; Clausi, 2002; Bogdanov et al., 2005; Maillard et al., 2005; Yu et al., 2012).

Numerous efforts have been made to develop algorithms to retrieve sea ice variables from SAR data. The SAR polynya detection algorithm proposed by Dokken et al. (2002) is based on wavelet transforms for edge detection and standard texture analysis. A threshold function using texture information is used to classify sea ice and water for polynya detection. A semi-automated sea ice classification method based on fuzzy rules was reported by Gill (2003) for classification of RADARSAT-1 data over the Arctic into calm water, wind-roughened water, and sea ice in low and high concentrations. Advanced Reasoning using Knowledge for Typing of Sea Ice (ARKTOS) (Soh et al., 2004) has been established to support scientific research and operational applications in the field of sea ice segmentation and classification. Haarpainter and Solbø (2007) developed an automatic algorithm for ice–ocean discrimination in RADARSAT-1 and ENVISAT SAR imagery. The texture-based algorithm consists of an automatically trained maximum likelihood classifier and divides the SAR images into slices of small incidence angle ranges. The results show that sea ice and water can be discriminated quite reliably. Some examples showed a tendency of the algorithm to a better performance at low incidence angles. Karvonen et al. (2005) distinguished the Baltic Sea ice from open water based on thresholding of segment-wise local autocorrelations in SAR images. The method provided 90 % accuracy compared to digital ice charts for the Baltic Sea. This algorithm has been used by the Finnish Meteorological Institute (FMI). Tests with RADARSAT-2 and ENVISAT SAR data show that over 89.4 % of the test data fit the ice classification provided by the Finnish Ice Service for the Baltic Sea and Arctic Sea (Karvonen, 2010, 2012).

Dual polarization has several advantages for sea ice classification compared to single-polarization SAR data. Rough or frost-flower-covered young ice and multiyear ice, while very different in their thickness (10–15 cm and more than 2.5 m, respectively), show rather similar brightness in the HH channel whereas MYI is brighter than young ice in the HV channel. Smooth first-year level ice is darker in both HH and HV and can be easily distinguished from young ice and MYI. Wind-roughened open water is difficult to distinguish from sea ice in a single HH polarization. However, open water especially affected by wind is darker in HV that improves sea ice classification (Sandven et al., 2008). The dual-polarization ENVISAT SAR Alternative Polarization Mode data enabled discrimination of sea ice types and open water with a decision-tree classifier using estimated statistical thresholds for winter. Open water can be unambiguously discriminated from smooth FYI, rough FYI, and MYI with > 99 % accuracy using a co-polarized ratio threshold (Geldsetzer and Yackel, 2009). The possibilities of supervised k-means and maximum likelihood classification of various SAR polarimetric data to three pre-identified sea ice types and wind-roughened open water was explored in Gill and Yackel (2012).

The MAp-Guided Sea Ice Classification System (MAGIC) for automated ice–water discrimination on dual-polarization images from RADARSAT-2 combines a "glocal" Iterative Region Growing using Semantics (IRGS) classification (Yu and Clausi, 2008) with a pixel-based support vector machine (SVM) approach. The "glocal" classification identifies homogeneous regions with arbitrary class labels. The ice–water map is created with the SVM classifier exploiting SAR texture and backscatter features. The MAGIC system has been applied on 20 RS2 scenes over the Beaufort Sea. The average classification accuracy with respect to manually drawn ice charts is 96.5 % (Clausi et al., 2010; Ochilov and Clausi, 2012; Leigh et al., 2014).

A neural-network-based algorithm has been developed for ENVISAT SAR images for operational sea ice classification including validation (Zakhvatkina et al., 2013). The algorithm discriminated the level FYI, deformed FYI, MYI, and open water/nilas in the high Arctic in winter conditions and demonstrated good applicability in the central Arctic. Using the same approach an algorithm for mapping ice–water utilizing ENVISAT ASAR WSM images was created for automated ice edge detection in Fram Strait. The ice–water classes were estimated by a multi-layer perceptron neural network which uses SAR calculated texture features and concentration data from AMSR (Advanced Microwave Scanning Radiometer) and, later, SSM/I (Special Sensor Microwave/Imager) as inputs (Sandven et al., 2012). Daily ice–water products were provided with a resolution of 525 m from winter 2011 until April 2012. The accuracy of this classification was about 97 % compared to high-resolution sea ice concentration charts based on manual interpretation of satellite data provided by the Norwegian Meteorological Institute.

Our goal is to extend the method originally used for the single polarized ENVISAT SAR images (Sandven et al., 2012) by utilizing dual-polarization data from RS2 and to develop an algorithm for ice–water classification, which can be applied to RS2 data for the production of ice–water maps as part of marine services under the Copernicus programme. A special motivation for our work was not only development of an algorithm but also its extensively validation in various sea ice conditions and identification of the applicability conditions. We also aimed to develop the algorithm as an open-source software available for other scientists. Our algorithm is based on texture features and the SVM method using the advantages of dual-polarization RS2 SAR image data.

This paper describes the developed algorithm and discusses practical issues of its applicability. The steps and parameters for implementation of the algorithm are described, allowing users to test the algorithms themselves. The paper is organized as follows. Section 2 introduces the satellite images and geographical area used in the study. The algorithm including pre-processing and validation procedure is

described in Sect. 3. Results of the pre-processing step, ice–water classification, and comparison with manual ice charts are given in Sect. 4. Finally, a discussion of the results is presented in Sect. 5.

2 Data

The region of interest is the ice-covered sea between Greenland and Franz Josef Land, where detailed ice information from SAR data is important due to the highly variable sea ice conditions, in particular the export out of the Arctic through Fram Strait (Vinje and Finnekåsa, 1986). SAR is the most useful sensor to provide high-resolution year-round data for estimation of sea ice variables such as ice classification, ice edge variability, and ice drift.

This study is based on RS2 ScanSAR Wide (SCW) mode images with 500 km swath width, a pixel spacing of 50×50 m, and dual-polarization (HH + HV). This is the main mode used by RS2 for operational sea ice monitoring (RS2 Product Description, 2011). Twenty-four SCW scenes around Svalbard (Fig. 1) from 2011 and 2012 were utilized in the following analysis to train the algorithm. The winter-month images were selected to cover various types of thin (e.g., new and young ice), first-year, and multiyear ice with different degrees of deformation, packed ice, broken ice, and open water under different wind speed conditions (rough, very rough, and calm water, also in leads). The radar images include the most typical samples since the radar intensity contrast between open water and ice varies greatly with ice conditions and wind speed or direction which significantly affect the radar brightness of open water. In summer the contrast between backscatter intensities of the melted different ice types observed on the SAR image is diminished since surfaces become smoother and are covered by meltwater. The intensities are reduced as well as the contrast between ice and OW.

The backscatter at HH generally decreases with increasing incidence angle (Fig. 2a), whereas the HV channel is less sensitive to the incidence angle. The HV channel includes disturbances in azimuth direction (visible as bright and dark stripes) along the burst boundaries in the ScanSAR Wide Beam SAR image (Fig. 2b). The expected noise level is a local mean noise power value that fluctuates across the image. The noise level is obtained from a model that accounts for the characteristics of the SAR sensor, the beam mode, the acquisition, and the ground processing (RS2 PUG) (Jefferies, 2012). The system noise level as a function of the incidence angle is documented in the XML file that comes with the RS2 image.

3 Methodology

3.1 Incidence angle correction for HH

During the first step of our ice–water classification algorithm SAR data pre-processing is conducted, including incidence angular correction for HH and absolute calibration to obtain σ° values. The auxiliary XML files coming with the product, i.e., scaling look-up table (LUT), provide information for georeferencing and calibration. These LUTs allow converting the processed digital numbers of the output SAR image to calibrated values. An important goal of radiometric calibration is to provide the proper comparison between the scattering of image targets with different SAR sensors or from the same sensor with different operating conditions, so the backscatter values of targets can be compared to one another or a reference. Absolute radiation calibration is used to convert the digital numbers in the SAR image to σ°, applying a constant offset and range dependent gains to the SAR image (RS2 Product Description, 2011). All images are corrected to a reference angle of 35°, which represents the center incidence angle and allows analysis of the SAR images without brightness amplification. Backscatter recalculation to 35° incidence angle is carried out using a predefined calculated coefficient:

$$\sigma_j{}^\circ = 10 \cdot \log_{10}\left(\frac{\left(\text{digital number}_j^2\right)}{A_j} \cdot \sin\left(\theta_j\right)\right) - \left(\text{coefficient} \cdot \left(\theta_j - 35\right)\right), \quad (1)$$

where σ° is the backscatter values of pixels in jth line (range direction), given in dB; digital number is the pixel brightness (data consist of the SAR amplitude value *Amp* and intensity value $I = \text{Amp}^2$; A is the gain value (invariant in line) corresponding to the range sample j (obtained by linear interpolation of the LUT supplied gain values); θ is the incidence angle for each jth pixel; and coefficient is the predefined calculated coefficient.

The coefficient was defined by calculating the linear trend of the observed backscatter signal on several HH-polarized RS2 SCW images of pack ice. The procedure is similar to the pre-processing of ENVISAT ASAR data in Zakhvatkina et al. (2013). The backscatter normalization to a pre-defined incidence angle provides homogenous image contrast across the swath over ice-covered areas. The details of the angular correction method are discussed in Sect. 5.1.

3.2 Thermal noise correction for HV

SAR data pre-processing also includes reduction of thermal noise effect and absolute calibration for HV. The thermal noise reduction consists of three steps: (1) reading the noise values and corresponding incidence angles from the XML file, (2) interpolation of noise on a finer grid for each

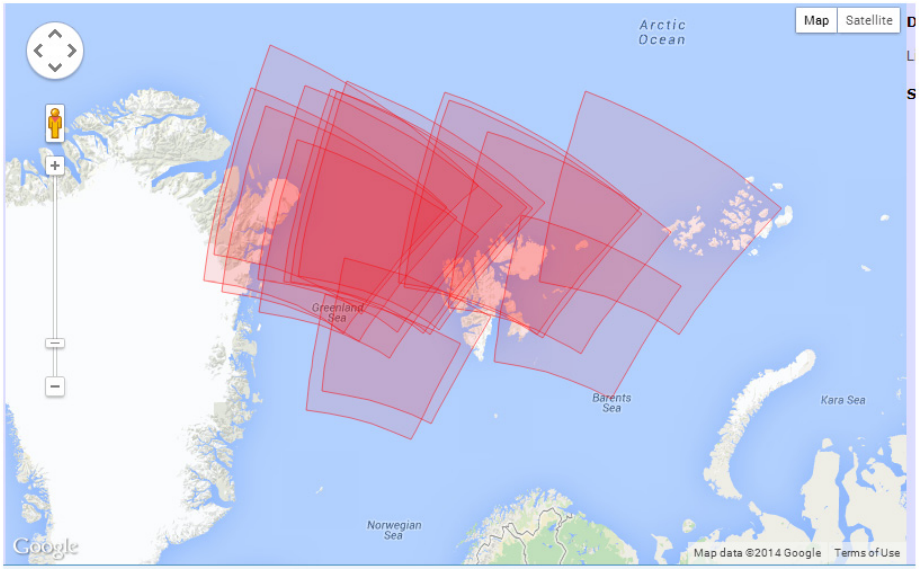

Figure 1. Location of RADARSAT-2 image used for training. All data are provided in GeoTIFF format with auxiliary XML files.

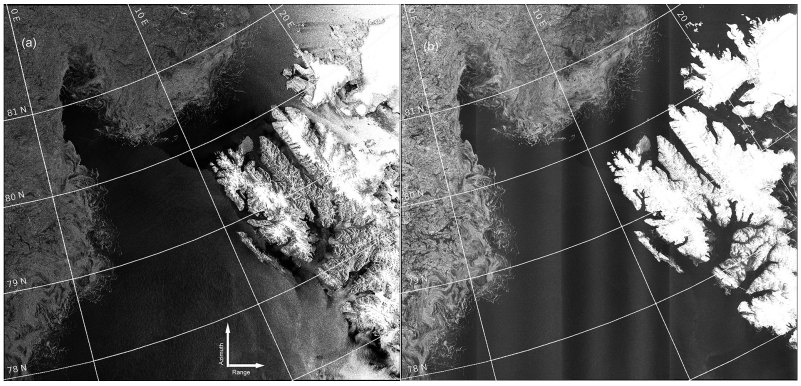

Figure 2. RS2 SCW dual-polarization image taken over Fram Strait on 28 November 2011 prior pre-processing. **(a)** HH channel with angular dependence; **(b)** HV channel with noise floor variations.

pixel, and (3) subtraction of interpolated noise values from the backscatter values of the entire image.

Due to the discontinuity of the noise floor at the boundaries of the individual SAR beams and the low resolution of the provided noise values in the XML file (only 100 points for 500 km swath width), the noise correction may result in an erroneous subtraction of a high noise floor from a low signal of the neighboring SAR beam and, hence, yield negative values for σ°. To prevent such flaws, a 10 pixel wide stripe of data along the edge of the SAR beam is masked out and disabled for further analysis.

3.3 Manual classification

The second step includes manual classification of SAR images into predefined classes (e.g., open water and ice of various types depending on which classes are needed). The predefined classes take into account information from optical data, ice concentration from passive microwave, previous classification results, and historical data.

Manual classification has been done for the training images containing several different sea ice types and ice-free areas with both rough and smooth open water. Predominant subclasses, which must be reliable and of high quality, were identified and chosen by sea ice experts through visual analysis of RS2 scenes based on their previous experience. The images selected for our algorithm training did not contain homogeneous ice cover because the mixing of different ice types with different degrees of deformation, cracks, ridges and leads usually occurs in ice-covered areas. The main class "sea ice" was chosen to include the following subclasses: (1) subclass including young ice, first-year, and multiyear ice; (2) fast ice; and (3) broken ice on the edge (border) mixed with ice-free areas (mostly found in the marginal ice zone). The class "open water" included the two subclasses open water with high and very high wind speed conditions and a third subclass that represented a mixture of calm open water, frazil ice, leads, and nilas. These manual classification results were collocated with texture feature images (description provided in Sects. 3.4 and 4.2) to get a number of training vectors. For the final product the subclasses were merged into the main classes "sea ice" and "open water" since the similarities between the subclasses are too high for a reliable discrimination without additional data.

3.4 Calculation of texture features

The third step is a calculation of texture features from HH and HV images. The calculation of texture features consists of the computation of the gray level co-occurrence matrix (GLCM) using Eq. (2) and the calculation of texture features based on the GLCM (Eqs. 3–10). Considering the full range of possible brightness levels (e.g., 0–255) and a small window size, most GLCM elements would be zero and that would have a negative effect on the classification result. Therefore we divide the full brightness range into few intervals (quantization levels K). The GLCM is created for each direction θ, where each cell (i, j) is a measure of the relative frequency of two pixels occurrence with brightness i and j, respectively, separated by a co-occurrence distance d. One may also say that the matrix element $P_{d,\theta}(i, j)$ is a measure of the second-order statistical probability for changes between gray levels i and j at a particular displacement distance d and at a particular angle (direction) (θ). The size of square GLCM is equal to number of quantized brightness levels K. The GLCM is averaged over four directions θ (0, 45, 90, 135°) to account for possible rotation of the ice floes (Clausi, 2002; Haralick et al., 1973).

$$S_{d,\theta}(i,j) = \frac{P_{d,\theta}(i,j)}{\sum_{i=1}^{K}\sum_{j=1}^{K} P_{d,\theta}(i,j)}, \quad (2)$$

where $S_{d,\theta}$ is the GLCM, $P_{d,\theta}$ is the number of neighbor pixel pairs, θ is the fixed vector directions (0, 45, 90, 135°), d is the co-occurrence distance, K is the number of quantized gray levels, and i, j are the gray levels (0–255).

$$\text{Energy} = \sum_{i=1}^{K}\sum_{j=1}^{K}\left[S_{d,\theta}(i,j)\right]^2 \quad (3)$$

$$\text{Homogeneity} = \sum_{i=1}^{K}\sum_{j=1}^{K}\frac{S_{d,\theta}(i,j)}{1+(i-j)^2} \quad (4)$$

$$\text{Contrast} = \sum_{i=1}^{K}\sum_{j=1}^{K}(i-j)^2 S_{d,\theta}(i,j) \quad (5)$$

$$\text{Correlation} = \frac{\sum_{i=1}^{K}\sum_{j=1}^{K}(i-\mu_x)\left(j-\mu_y\right)S_{d,\theta}(i,j)}{\sigma_x\sigma_y} \quad (6)$$

$$\text{Entropy} = -\sum_{i=1}^{K}\sum_{j=1}^{K} S_{d,\theta}(i,j)\log_{10}S_{d,\theta}(i,j) \quad (7)$$

$$\text{Kurtosis} = \sum_{i=1}^{K}\sum_{j=1}^{K}\frac{\left(S_{d,\theta}-\mu\right)^4}{\sigma^4} \quad (8)$$

$$\text{Skewness} = \sum_{i=1}^{K}\sum_{j=1}^{K}\frac{\left(S_{d,\theta}-\mu\right)^3}{\sigma^3} \quad (9)$$

$$\text{Cluster prominence} = \sum_{i=1}^{K}\sum_{j=1}^{K}\left(i+j-\mu_x-\mu_y\right)^4 S_{d,\theta}(i,j) \quad (10)$$

$\sigma_x^2 = \sum_{i=1}^{K}\sum_{j=1}^{K}(j-\mu_x)^2 S_{d,\theta}(i,j)$ and $\sigma_y^2 = \sum_{i=1}^{K}\sum_{j=1}^{K}\left(j-\mu_y\right)^2 S_{d,\theta}(i,j)$ are standard deviation of rows and columns, $\mu_x = \sum_{i=1}^{K}\sum_{j=1}^{K} i\,S_{d,\theta}$ and $\mu_y = \sum_{i=1}^{K}\sum_{j=1}^{K} j\,S_{d,\theta}$ are mean values of rows and columns, $\sigma^2 = \sum_{i=1}^{K}(i-\mu)^2\sum_{j=1}^{K} S_{d,\theta}(i,j)$ is the standard deviation, and $\mu = \sum_{i=1}^{K}\sum_{j=1}^{K} i\,S_{d,\theta}(i,j)$ is the mean values of brightness.

The results of this procedure depend on several factors such as the size of the sliding window, the co-occurrence distance, and the quantization levels (Shokr, 1991; Soh and Tsatsoulis, 1999; Clausi, 2002). In order to test the effects of these parameters on the classification accuracy, texture features were calculated for the window sizes 16, 32, 64, and 128 pixels using different co-occurrence distances and varying the number of quantized gray levels (Table 1). The optimal values for the parameters of texture features calculation were selected analyzing variations in the texture parameters by visual inspection of the normalized mean values distribution of each texture feature for a defined class. The decision is made for the benefit of the cases when the separation of the normalized texture values for the classes increases in the majority of investigated texture feature figures. Defined parameters were applied for calculations of all set of texture features, and then the visual comparison showed the best discrimination between the ice–water classes for some texture features (details provided in Sect. 4.2).

Table 1. Experiments of computation parameters. W is the window size, d is the co-occurrence distance, K is the quantized gray level, and moving step is a step of sliding window moving.

W	d	Moving step	K
32	4	8/16/32	16/25/32
32	8	8/16/32	16/25/32
32	16	8/16/32	16/25/32
64	4	8/16/32/64	16/25/32
64	8	8/16/32/64	16/25/32
64	16	8/16/32/64	16/25/32
64	32	8/16/32/64	16/25/32
128	4	32/64/128	16/25/32
128	8	32/64/128	16/25/32
128	16	32/64/128	16/25/32
128	32	32/64/128	16/25/32
128	64	32/64/128	16/25/32

A selection procedure is applied to limit a set of texture characteristics that provides a good classification with a small computational load. This procedure includes visual assessment of scatter plots, comparing values of texture features in different combinations. Candidate texture features that provide the best separation of classes are selected and others are discarded. The selection procedure also uses a set of training images to establish the set of texture features and its computation parameters, providing the smallest classification error. In other words, we constrain the texture features number by the demanded balance considering the SAR image level of details, computation time, and the optimal reliable class separation.

3.5 Support vector machines

The next step is the training of classifier (e.g., SVM) for classification of arrays with certain texture features as well as σ° values based on the results of manual classification. The SVM are supervised learning methods with associated learning algorithms that provide data classification. The basic SVM takes a set of input data (several "attributes", i.e., the features) and predicts the outputs (i.e., the class labels) for each given input, making it a non-probabilistic classifier. The support vector network maps the input vectors into a high dimensional feature space through nonlinear mapping. SVM finds a linear hyperplane separating objects into classes by the most widely clear gap between the nearest training data points of any class. An optimal hyperplane is defined as the linear decision function with maximal margin between the vectors in this higher dimensional space. When the maximum margin is found, only points which lie closest to the hyperplane have weights >0. These points determine this margin and are called support vectors (Cortes and Vapnik, 1995).

SVM performs a nonlinear classification using the kernel trick. The kernel function may transform the data into a higher dimensional space to make this nonlinearly separation possible when the relation between class labels and attributes is nonlinear. A common choice is a Gaussian kernel. In our study we have used the radial basis function kernel (RBF kernel), which is found to work well in a wide variety of applications.

The scikit-learn open source was used to implement the SVM classification method (http://scikit-learn.org/stable/index.html). SVM models implementation in scikit-learn is based on LIBSVM. Basically, SVM trains the model using low-level method and can only solve binary classification problems. In the case of multi-class classification, LIBSVM implements the "one-against-one" technique by fitting all binary sub-classifiers and finding the correct class by a voting mechanism. The effectiveness of SVM training depends on the selection of kernel, the kernel's parameters (γ), and margin parameter C. The software provides a simple tool to check a grid of parameters obtaining cross-validation accuracy for each parameter setting: the parameters with the highest cross-validation accuracy are returned (Hsu et al., 2003). The SVM parameters in our case were $\gamma = 0.1$ and $C = 1$.

The calculated texture features and σ° values corresponding to the manually identified classes on several preprocessed RS2 images were used as input data for training the SVM classifier. After completing the training procedure the resulting SVM is applied for automatic sea ice classification to divide the RS2 scene into the predefined classes.

3.6 Validation

The final step includes validation of the classification results using manually drawn ice charts. Validation of Arctic sea ice classification results is a challenging task since sea ice is a very inhomogeneous medium and validation data on ice classification are difficult to obtain. As a substitute our sea ice classification results have been compared with manual sea ice charts produced by the operational ice service at the Norwegian Meteorological Institute (MET Norway, http://polarview.met.no/). MET Norway produces ice charts every workday using the following data sources: high-resolution SAR images, low-resolution microwave SSM/I and SSMIS data (DMSP), MODIS images (Terra and Aqua), and AVHRR data from NOAA. In our comparison MET Norway ice charts are assumed to represent "true" classification and the confusion matrix was calculated for accuracy evaluation of our algorithm results.

After completing the algorithm training, the fully automated image classification includes only three of the above mentioned steps: pre-processing (Sect. 3.1 and 3.2), texture feature retrieval (Sect. 3.4), and application of the automatic classifier (SVM).

The initial size of the full-resolution RS2 SCW image is about $10\,000 \times 10\,000$ pixels. We downscale the original image by averaging to 5000×5000 pixels to increase the computational efficiency and decrease the influence of speckle

noise. The image size is further reduced during the computation of the texture features by using a sliding window with 16 pixel step size (the detailed parameters are described in Sect. 4.2). The image size of the final product is about 330×330 pixels with 1600 m pixel spacing. This reduction in resolution significantly increases the processing speed and allows computing a classification results in less than 15 min.

Pre-processing of RS2 data was performed utilizing the open-source Python toolbox NANSAT (Korosov et al., 2015), (https://github.com/nansencenter/nansat/wiki). The texture extraction algorithm was created in the Python programming language.

4 Results

To illustrate the algorithm performance the automatic SVM classification was applied to the RS2 scene shown in Fig. 2. The example scene was acquired on 28 November 2011 over the western part of Svalbard in Fram Strait. Figures 2 and 3 show both HH and HV polarizations before and after corresponding corrections described in Sect. 2: compensation of incidence angle effects for HH (Fig. 3a) and noise reduction for HV (Fig. 3b). The image contains several ice types, open water under different wind conditions, and land. The open water area is located on the right-hand side of the image and the ice-covered area in the upper-left corner. The sea ice area includes a marginal ice zone with bright broken up ice. The ice-covered areas and the rough OW areas appear both bright in HH and are therefore difficult to distinguish. Including HV, however, provides additional information since OW areas on this image appear generally darker than sea ice in HV. This is one of the major dual-polarization advantages and can be seen in the lower right part of the example image (Fig. 2).

4.1 Correction for incidence angle and thermal noise

The linear trend coefficient used for backscatter angular dependence correction of HH was estimated to be -0.298 dB/1° and allowed normalization of σ° to the incidence angle 35° as shown on Fig. 3a and c. The application of our noise correction procedure for HV reduces significantly thermal noise and gets rid of vertical striping as shown in Fig. 3b, d.

4.2 Texture feature calculation

As part of the algorithm development texture features were calculated based on different parameter settings. Visual examination of mean values of several texture features (Fig. 4a, b) suggested the optimal combination of the sliding window, moving step, and distance between neighboring pixels, which provides better separation of the ice–water classes compared to other combinations of window sizes with different texture parameters. A set of texture characteristics was selected analyzing variations in mean values of the textural characteristics of defined classes calculated with several combinations of obtained parameters (Fig. 4c, d). The largest change of distance between mean values of texture features of different classes on Fig. 4d defines the best option for the potential classification. Finally, together with visual inspection of the texture images (some examples are given on Fig. 5a–f) of the a priori known most problematic classification cases on the SAR images used for training, the set of texture characteristics are defined. The best results were achieved using the following parameter set: number of gray levels ($K = 32$), co-occurrence distance ($d = 8$), sliding window size ($w = 64 \times 64$), and moving step of the sliding window ($s = 16$). Using the following texture features for the two channels provided the best test results: for HH channel the energy, inertia, cluster prominence, entropy, third statistical moment of brightness, backscatter, and standard deviation were calculated; for HV channel the energy, correlation, homogeneity, entropy, and backscatter were calculated. Including more texture features for both channels was tested but found not to improve the information content. The calculation parameters were found experimentally to give a good compromise between speckle noise reduction, preservation of details, and correct classification results (methodology description in Zakhvatkina et al., 2013).

Texture characteristics provide a more complete delineation of surface parameters in addition to the raw backscatter signal, and increase the ability for ice and water separation. The scatter plots in Fig. 5g, h show the values of two different texture features plotted against each other and illustrate the usefulness of texture features for discrimination between defined classes.

4.3 Manual versus automatic classification

As described in Sect. 3 several SAR images were classified manually as part of the training procedure for the automatic algorithm. Comparing the manual classification from sea ice expert analysis with the algorithm results (Fig. 6) reveals a general high level of correspondence and illustrates the capability of the automatic approach. Detailed observation of the classification results show that most misclassifications are observed near land and in the MIZ. Figure 6b shows small features inside ice-covered zone (blue dots) that were misclassified as OW.

4.4 Validation

Validation of the algorithm results has been performed using 2705 RS2 images taken over our area of interest in the period 1 January 2013 until 25 October 2015. For each RS2 image an error matrix based on pixel-by-pixel difference between algorithm result and MET Norway chart has been calculated. OW and sea ice correspondence as well as an overall accuracy were obtained for each RS2 image classification result and averaged accuracies have been calculated for

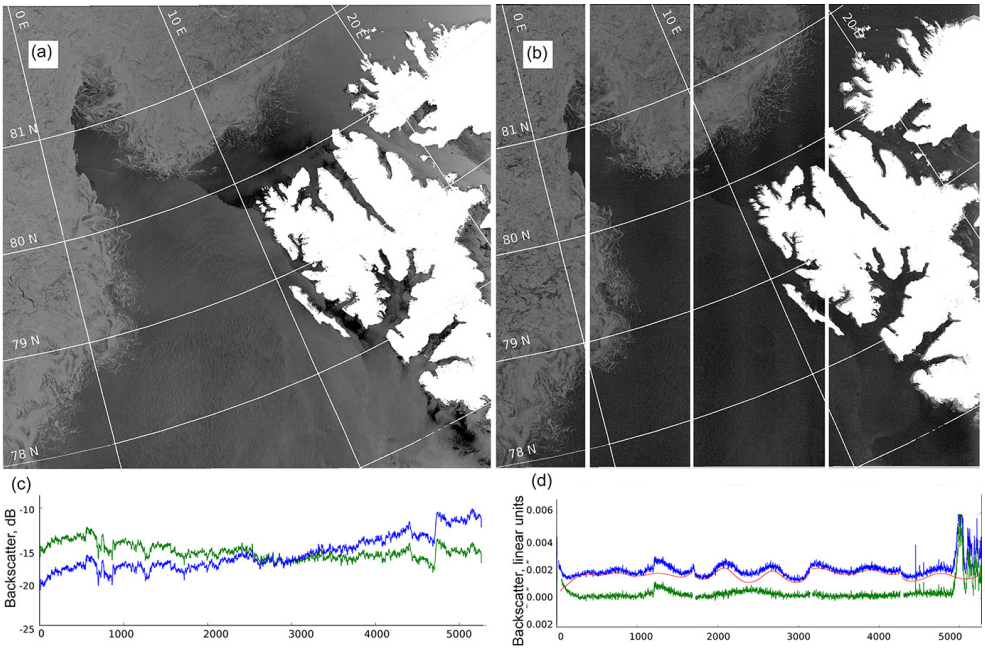

Figure 3. RS2 SCW dual-polarization image taken over Fram Strait on 28 November 2011, including pre-processing. **(a)** Calibrated image after correction of σ° at 35° incidence angle using the predefined coefficient for sea ice of -0.298 dB/1°. **(b)** Noise-corrected image: beam boundaries are visible due to differences in noise levels between adjacent beams. **(c)** σ° curves of SAR image across the entire swath: original image (blue) and after angular correction (green). **(d)** σ° curves of SAR image along the whole swath. The blue curve shows σ° value profile of the raw HV channel image in range direction, the red curve depicts the noise floor level, and the green curve is the result of subtraction.

each month. The impact of each class on the classification error has been estimated and the respective monthly averaged errors were computed. The averaged overall accuracies including standard deviation and errors in ice and water classification for each month are given in Table 2. In addition, the monthly accuracies are presented as a graph in Fig. 7. The monthly averaged overall accuracies show lower values during summer months (Fig. 7 – from May to October) and higher values during winter. The average total classification accuracy for all 2705 scenes is 91 ± 4 %.

Figure 8 shows an example of the validation process. The RS2 HH image is shown in Fig. 8a, the result of our SVM classification in Fig. 8c, and the MET Norway sea ice chart in Fig. 8b. To compare the algorithm result with the manually derived ice charts, both products are reclassified into ice and water (Fig. 8d and e). The error matrix is represented as an image (Fig. 8f) with the following three classes: no difference, sea ice error (MET Norway: sea ice, OW in our results), and OW error (MET Norway: OW, sea ice in our results).

5 Discussion

5.1 Significance of incidence angle variations and thermal noise reduction

Water areas have a very large range of brightness depending on wind speed. At higher wind speeds the contrast between open water and first- and multi-year ice is reduced, which gives an ambiguity between these classes. The dependence of backscatter on incidence angle is well known (Shokr, 2009) and is significantly higher for open water than for sea ice. The correction factor for the incidence angle is therefore very different for ice and water. The coefficients for the angular dependence of water-covered areas are significantly influenced by wind conditions – with stronger wind intensity grows faster. Our observations show that angular dependence of sea ice is more stable regardless of wind or other conditions (Fig. 3). Since the surface type is not known a priori we have to choose which angular correction to apply and the preference is given to the more reliable sea ice angular correction. However, the total compensation is impossible as the backscatter dependence on the incidence angle varies for dif-

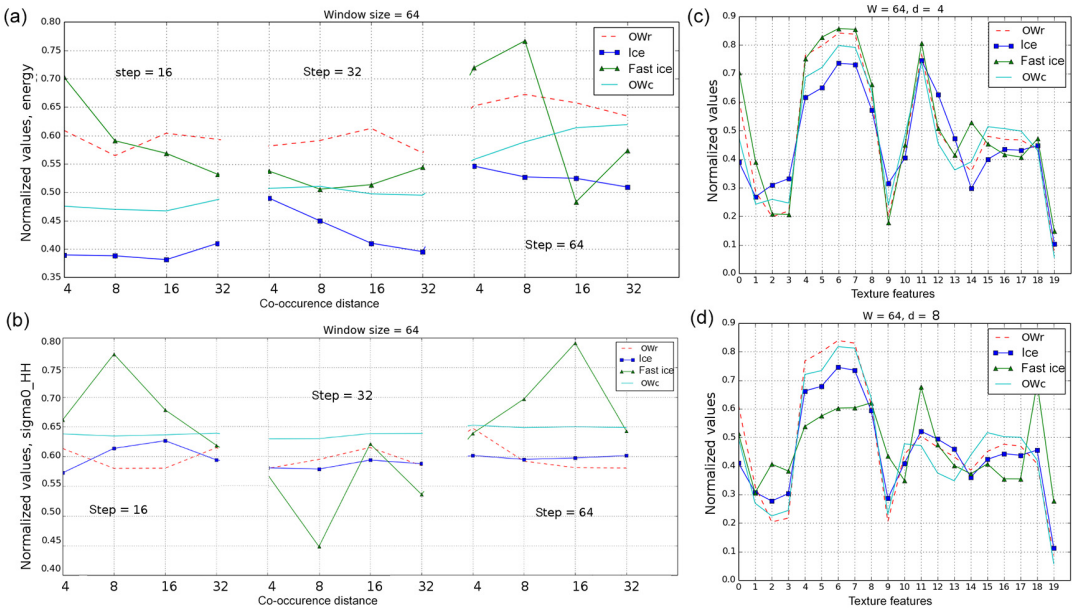

Figure 4. Normalized mean values of texture characteristics for calm open water (OWc), rough open water (OWr), ice, and fast ice, calculated in window size 64 × 64 pixels: **(a)** energy and **(b)** σ° of HH with different co-occurrence distances for several moving step variations. Set of texture features are calculated with found above parameters: **(c)** $d = 4$ and step = 16; **(d)** $d = 8$ and step = 16 pixels (0 – energy, 1 – correlation, 2 – inertia or contrast, 3 – cluster prominence, 4 – homogeneity, 5 – entropy, 6 – third central statistical moment of brightness, 7 – fourth central statistical moment of brightness, 8 – average sea ice backscatter, 9 – standard deviation of brightness for HH). The range from 10 to 19 indicates the same texture features calculated for HV. The calculations were made for several images used for training.

Table 2. Monthly averaged accuracies of the automatic ice charts compared to MET Norway ice charts (results given in %).

2013						2014						2015					
Months	Images	Ov acc	SD	OW err	Ice err	Months	Images	Ov acc	SD	OW err	Ice err	Months	Images	Ov acc	SD	OW err	Ice err
Jan	72	91.52	5.43	3.99	4.50	Jan	97	91.89	4.70	2.52	5.59	Jan	51	94.84	3.10	1.28	3.88
Feb	70	91.05	4.54	2.66	6.30	Feb	93	92.11	5.05	3.37	4.52	Feb	33	94.47	4.05	2.33	3.86
Mar	106	91.21	4.71	1.20	7.59	Mar	110	92.20	3.45	2.83	4.98	Mar	73	94.36	4.40	1.67	3.82
Apr	110	92.03	4.57	0.95	7.02	Apr	130	93.34	3.40	1.30	5.36	Apr	54	94.86	4.36	1.47	3.83
May	111	88.60	7.96	0.88	10.52	May	137	92.80	4.77	1.00	6.20	May	63	95.05	3.21	0.72	3.81
Jun	98	87.64	7.58	1.59	10.76	Jun	93	89.98	5.78	1.54	8.48	Jun	67	84.73	14.09	0.69	3.80
Jul	83	89.73	8.01	2.72	7.54	Jul	95	86.82	9.89	1.98	11.20	Jul	47	74.49	21.61	1.73	3.81
Aug	85	94.36	3.10	2.96	2.68	Aug	88	88.39	10.87	1.87	9.74	Aug	47	86.65	12.25	2.64	3.85
Sep	93	95.88	2.02	2.47	1.65	Sep	97	87.55	17.56	8.24	4.21	Sep	43	94.83	3.87	3.36	3.78
Okt	72	94.53	2.99	3.98	1.49	Okt	78	94.89	3.15	1.87	3.24	Okt	27	94.69	4.16	4.58	3.78
Nov	84	92.00	4.77	5.10	2.90	Nov	47	94.58	2.84	2.38	3.04	Nov					
Dec	97	90.93	6.63	3.18	5.88	Dec	54	92.94	7.99	3.45	3.61	Dec					

Ov acc is monthly overall accuracy; SD is the standard deviation; OW err means open water on MET Norway ice chart and sea ice on automatic ice chart; Ice err means sea ice on MET Norway ice chart and open water on automatic ice chart.

ferent ice types (Mäkynen et al., 2002) and water areas in the scene. The radiometric corrections during calibration process are just a first-order approximation; nevertheless, the advantages of performing the angular correction are greater than the disadvantages (Moen et al., 2015). With regards to thermal noise correction we found that sometimes not all visible noise floor artifacts inside beams can be completely removed and these residuals may cause classification errors.

5.2 Number of texture features vs. efficiency

In addition to the eigth extracted texture features we characterize the surface by values of σ° averaged within the sliding window and a value of standard deviations. Given that we have two channels (HH and HV) the number of parameters grows up to 20 and some of them are strongly intercorrelated (Shokr, 1991; Albregtsen, 2008). High correlation be-

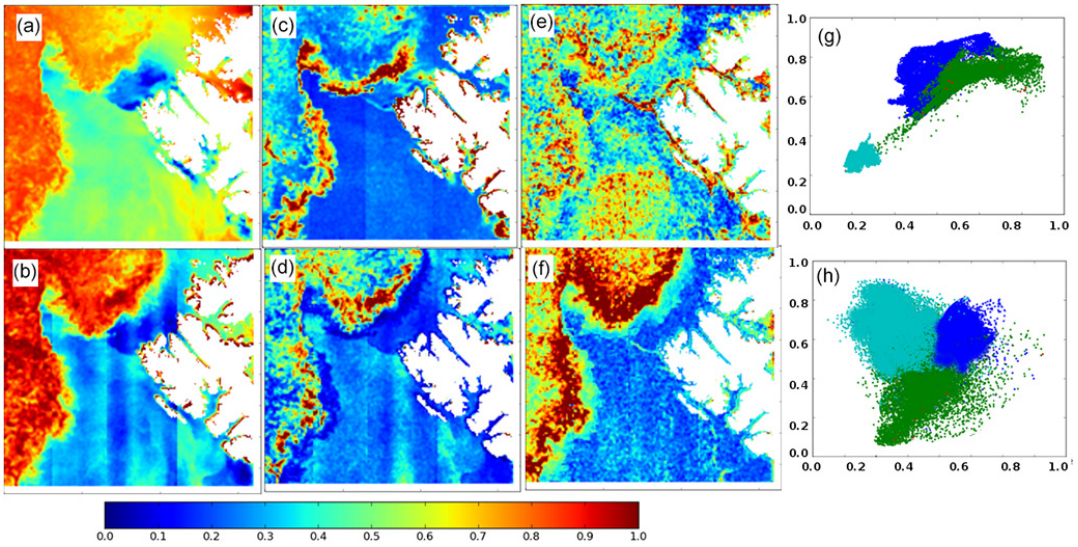

Figure 5. Texture features calculated for RS2 SCW scene, 28 November 2011, in the Fram Strait. **(a)** Backscatter of HH polarization; **(b)** backscatter of HV polarization; **(c)** inertia of HH polarization; **(d)** energy of HV polarization; **(e)** correlation of HH polarization; **(f)** correlation of HV polarization. The scatter plots show how a couple of textural features calculated from RS2 images, shown in Fig. 1, can be used to classify ice (green), rough OW (blue), and calm OW (cyan). **(g)** σ° of HV vs. σ° of HH. **(h)** Energy of HH vs. correlation of HV.

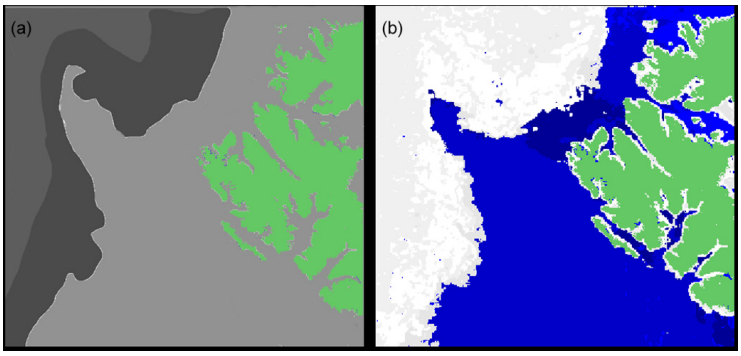

Figure 6. OW and sea ice classification of RS2 SCW image shown in Fig. 2. **(a)** Manual classification based on sea ice expert analysis to delineate sea ice (in the MIZ and general sea ice cover) and open water (calm and rough open water): dark gray is sea ice; very dark gray is marginal ice zone; light gray is OW; green is land. **(b)** Automatic SVM classification result: white is sea ice; dark blue is calm OW; blue is OW; green is land.

tween two textural characteristics shows that they have similar properties, and hence it makes no sense to use both features. In case of low correlation both features will contribute to the improvement of the classification accuracy (Clausi, 2002). The similarity can explain the misclassifications and in fact this is part of the motivation to reduce dimensionality. If we include too few texture features to the classifier then the informationally poor features have to be compensated by using complicated discrimination function and can lead to increased classification confusion. In contrast, if all texture features are used by the classifier, some classes can be underestimated or overestimated and the discrimination for many classes may lead to higher classification errors.

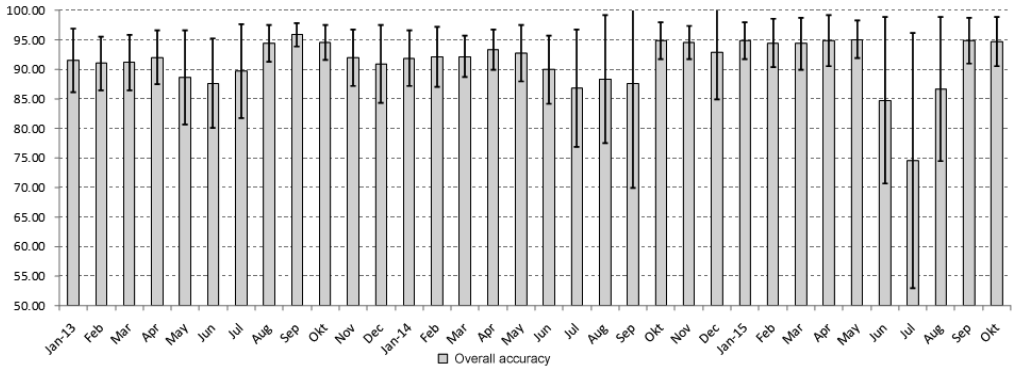

Figure 7. Monthly accuracy and standard deviation of SVM classification of RS2 images assuming that MET Norway operational ice charts are correct.

Sea ice in the upper part of Fig. 5a could not be distinguished from rough open water (upper right). However, Fig. 5b shows reliable detection of sea ice-covered area (left side). Calm open water can be easily recognized in Fig. 5c and d (dark blue areas). In both figures, the heterogeneous sea ice area can be clearly distinguished from the open water zone. The latter consist of very close ice floes and/or broken ice. Some other ice-covered area can be incorrectly defined as open water. Figure 5e adds more useful information about open water location (blue colored area). The scatter plot on Fig. 5g, h represents advantage of texture feature application for discrimination between the sea ice and two classes of open water using both polarizations, where sea ice (green) can be clearly seen as standing separately from OW (blue). The scatter plot in Fig. 5h demonstrates how different texture characteristics, e.g., energy versus correlation, of different polarizations can add useful information for detection. The examples in Fig. 5e and f show that the same texture feature calculated for one polarization can be used in applications to obtain well-delineated class; otherwise for other polarization it demonstrates the poor separation between classes.

5.3 Sources of errors

The MET Norway manual products and our algorithm results show generally a good consistency. However, differences typically appear at the ice–water boundary and inside ice-covered areas, where leads or channels on the SAR image are not delineated on the MET Norway ice charts. Some differences are also found in the coastal zones, where narrow ice zones near the coast are wrongly shown in our results or fast ice is wrongly classified as OW by our algorithm. This misclassification can be explained by appearance of fast ice and calm open water on a SAR image and its similarity in the low backscatter. For this case the polarization difference in backscatter between HH and HV bands (cross-polarization ratio) could be included for further improvement (Sandven, 2008; Dierking and Pedersen, 2012; Moen et al., 2013). More significant classification errors can be found in the MIZ.

Detecting typical backscatter ranges and textural structures for different sea ice types and water areas with different roughness stages is extremely difficult due to the high dynamic and variable nature of sea ice and wind speed impact. In particular, different structures on the water affected by wind and currents and visually detected on the SAR images (e.g., stripes, eddies) may cause wrong sea ice classification.

Residual HV noise effects (after correction) along the ScanSAR image beam boundaries and signal variations inside the separate beams due to instrumental artifacts (Fig. 5b, d) can have an uncorrected effect on the texture feature analysis and may cause classification errors. These residual noise effects are not visible in the ice-covered areas, but rough open water on high incidence angle close to the beam boundaries may be erroneously classified as sea ice.

The backscatter signal of melting ice becomes similar to open water and imposes limitations for the classification of RS2 images for the summer season.

We assume that our automatic algorithm classifies SAR images more reliable as than represented by the provided accuracy (91 %), and this inconsistency may occur for the following reasons:

1. The MET Norway ice charts have a lower resolution than our automatic ice charts making an absolute accurate estimation of the ice conditions in the each SAR images and detailed comparison impossible.

2. The classes obtained by MET Norway are not consistent with the simple ice–water classification provided by the algorithm. In the comparison, we reclassify the MET Norway ice chart into ice and open water. Here, areas with ice concentrations ≤ 10 % are regarded as open wa-

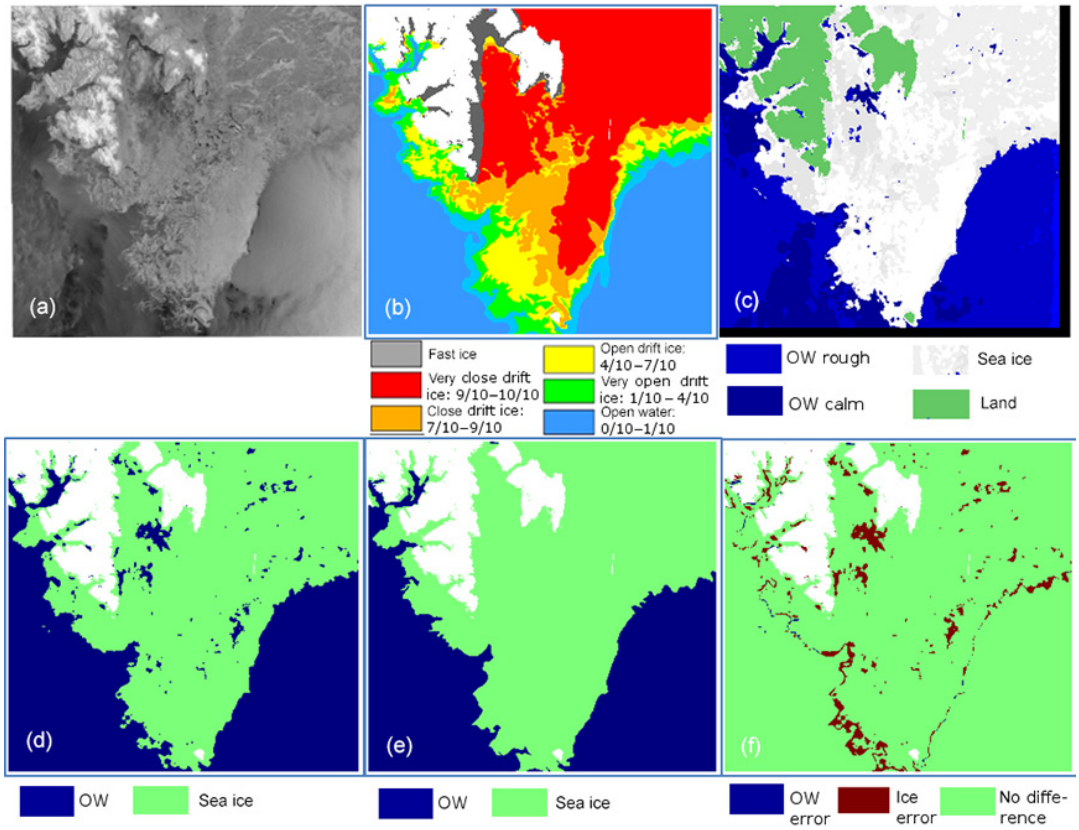

Figure 8. Validation procedure of automatic classification results compared to MET Norway ice charts. **(a)** Original RS2 SCW SAR image (HH polarization), taken over the southern part of Svalbard on 14 March 2013. **(b)** Collocated subset of manual ice concentration chart, provided by the Norwegian Ice Service (met.no) for the same day. **(c)** Result of the SVM classification. **(d)** Result of the SVM classification with delineation of two classes: water and sea ice. **(e)** Ice chart of MET Norway reclassified into two classes: open water (ice concentration from 0 to 10 %) and sea ice (ice concentration from 10 to 100 %). **(f)** The difference of recalculated MET Norway chart and classification result represents the error matrix as "image": no difference, sea ice error (sea ice in MET Norway, OW in our results), and OW error (OW in MET Norway, sea ice in our results). Overall accuracy is 95.78 %, OW error is 0.19 %, and ice error is 4.03 %.

ter. This assumption appears to be the subjective error factor during the validation process and finally reduces the accuracy.

3. MET Norway provides manual ice charts for every working day, but not for weekends and holidays. This might cause a difference in timing up to several days. Manual and automatic ice charts of the same day might also not be based on images taken at the same time of the day. Fram Strait is a very dynamic region and the sea ice situation can significantly change over time periods of several hours.

6 Conclusion

We have proposed an automated OW–ice cover classification of RADARSAT-2 SAR ScanSAR Wide Beam mode data acquired over Fram Strait for varying wind speeds and sea ice conditions. The classification uses backscatter and texture features together in a SVM approach. The intensity contrast between HH and HV polarization of open water increases at higher wind speeds, and open water is distinguished more reliably on dual-polarized RS2 data.

Previous studies of ENVISAT ASAR HH data in wide swath mode showed a similar backscatter dependence on incidence angle (Zakhvatkina et al., 2013), and the same tech-

nique was applied for the HH band of RS2 SCW images. The ScanSAR image swath consists of different combinations of four physical beams and there are well-known technical features caused by a wave-like modulation of the image intensity in range direction throughout the entire image in the sub-swaths and their edges of HV band (Romeiser et al., 2013). Although the techniques for compensating the effect in the SAR processor have been developed and applied, some ScanSAR images still show residual effects. To improve utilization of such images we have carried out a procedure of HV band noise reduction that is applied as a preprocessing tool. By computing texture features with sliding window size of 64×64 pixels and number of quantized gray levels amounting to 32, we classified more that 2700 SAR images for the period from January 2013 to October 2015. Validation of the classification was done by comparing with ice charts produced by MET Norway. The texture features were used as input to SVM classification. The results show that open water and ice are discriminated with an accuracy of 91 %.

The automated SVM-based algorithm has been adopted for operational decoding the ice edge, and it will also be extended and improved for sea ice type classification. With Sentinel-1A/B as the main satellite SAR system in the coming years, the next step will be to adapt the classification algorithm to Sentinel-1 data (Korosov, 2016). The amount of SAR data available for sea ice monitoring will increase significantly in the coming years. Efficient utilization of these data will require further efforts to develop automated algorithms which can be used in operational ice services.

7 Data availability

The RADARSAT-2 data used in this study are not publicly accessible because RADARSAT-2 is a commercial satellite. We obtained the data used in the study as MyOcean users under a special contingency agreement between ESA and MDA GSI.

Acknowledgements. The work has been supported by the EU projects MyOcean (grant agreement no. 218812), SIDARUS (grant agreement no. 262922), MAIRES (grant agreement no. 263165), Research Council of Norway (contract 196214), Norwegian Space Center (JOP.01.11.2), and EuRuCAS (grant agreement no. 295068), SONARC project under Research Council of Norway (contract no. 243608), and Russian Foundation for Basic Research (RFBR) project SONARC (grant agreement no. 15-55-20002). We acknowledge the MDA for providing RADARSAT-2 data through SIDARUS project. Authors would thank Nick Hughes from Norwegian Meteorological Institute for providing high-resolution ice charts for validation of the classification method.

Edited by: C. Duguay
Reviewed by: W. Dierking and two anonymous referees

References

Albregtsen, F.: Statistical Texture Measures Computed from Gray Level Coocurrence Matrices, Image Processing Laboratory Department of Informatics University of Oslo, 5 November 2008.

Bogdanov, A. V., Sandven, S., Johannessen, O. M., Alexandrov, V. Y., and Bobylev, L. P.: Multisensor approach to automated classification of sea ice image data, IEEE T. Geosci. Remote, 43, 1648–1664, 2005.

Clausi, D. A.: An analysis of co-occurrence texture statistics as a function of grey level quantization, Can. J. Remote Sens., 28, 45–62, 2002.

Clausi, D. A., Qin, A. K., Chowdhury, M. S., Yu, P., and Maillard, P.: MAGIC: MAp-Guided Ice Classification System, Can. J. Remote Sens., 36, suppl. 1, S13–S25, 2010.

Cortes, C. and Vapnik, V.: Support-Vector Networks, Mach. Learn., 20, 273–297, 1995.

Dierking, W.: Mapping of different sea ice regimes using images from Sentinel-1 and ALOS synthetic aperture radar, IEEE T. Geosci. Remote, 48, 1045–105, 2010.

Dierking, W.: Sea ice monitoring by synthetic aperture radar, Oceanography, 26, 100–111, 2013.

Dierking, W. and Pedersen, L.: Monitoring sea ice using ENVISAT ASAR— A new era starting 10 years ago, Proc. IEEE Int. Geosci. Remote SE (IGARSS2012), 1852–1855, 2012.

Dokken, S. T., Markus, P. W. T., Askne, J., and Bjork, G.: ERS SAR characterization of coastal polynyas in the Arctic and comparison with SSM/I and numerical model investigations, Remote Sens. Environ., 80, 321–335, 2002.

Geldsetzer, T. and Yackel, J. J.: Sea ice type and open water discrimination using dual co-polarized C-band SAR, Can. J. Remote Sens., 35, 73–84, 2009.

Gill, R. S.: SAR Ice Classification Using Fuzzy Screening Method, in: Proc. Workshop on Applications of SAR Polarimetry and Polarimetric Interferometry (POLinSAR), 14–16 January 2003, Frascati, Italy, 2003.

Gill, J. P. S. and Yackel, J. J.: Evaluation of C-band SAR polarimetric parameters for discriminating of first-year sea ice types, Can. J. Remote Sens., 38, 306–323, 2012.

Haarpaintner, J. and Solbø, S.: Automatic ice-ocean discrimination in SAR imagery, Norut IT-report, Tech. Rep., 2007.

Haralick, R. M., Shanmugam, K. S., and Dinstein, I.: Textural features for image classification, IEEE T. Syst. Man. Cyb., 3, 610–621, 1973.

Hsu, C.-W., Chang, C.-C., and Lin, C.-J.: A practical guide to support vector classification, Initial version: 2003, available at: http://www.csie.ntu.edu.tw/~cjlin/papers/guide/guide.pdf, last access: 8 June 2016.

Jefferies, B.: Radarsat-2 – New Ice Information Products, Proc. of the 13th Meeting – International Ice Charting Working Group, 15–19 October 2012, Tromso, Norway, 2012.

Johannessen, O. M., Alexandrov, V., Frolov, Bobylev, L., Sandven, S., Miles, M., Pettersson, L., Kloster, K., Smirnov, V., Mironov, Y., and Babich, N.: Remote Sensing of Sea Ice in the Northern Sea Route: Studies and Applications, Chichester, UK, Springer-Praxis, available at: https://www.nersc.no/sites/www.nersc.no/files/front-matter.pdf, 2007.

Karvonen, J.: C-band sea ice SAR classification based on segmentwise edge features, in: Geoscience and Remote Sensing New

Achievements, edited by: Imperatore, P. and Riccio, D., In- Tech, 129–146, 2010.

Karvonen, J.: Operational SAR-based sea ice drift monitoring over the Baltic Sea, Ocean Sci., 8, 473–483, 2012.

Karvonen, J., Simila, M., and Mäkynen, M.: Open Water Detection from Baltic Sea Ice Radarsat-1 SAR Imagery, IEEE T. Geosci. Remote Lett., 2, 275–279, 2005.

Korosov, A.: Very high resolution classification of Sentinel-1A data using segmentation and texture features, Proc. of European Space Agency Living Planet Symposium, 9–13 May 2016, Prague, Czech Republic, 2016.

Korosov, A., Hansen, M. W., and Yamakava, A.: Nansat – scientist friendly toolbox for processing satellite data, World Ocean Scientific Congress, 2–8 February 2015, Cochin, India, 2015.

Leigh, S., Zhijie, W., and Clausi, D. A.: Automated Ice–Water Classification Using Dual Polarization SAR Satellite Imagery, IEEE T. Geosci. Remote, 52, 5529–5539, 2014.

Maillard, P., Clausi, D. A., and Deng, H.: Map-guided sea ice segmentation and classification using SAR imagery and a MRF segmentation scheme, IEEE T. Geosci. Remote, 43, 2940–2951, 2005.

Mäkynen, M. P., Manninen, A. T., Similä, M. H., Karvonen, J. A., and Hallikainen, M. T.: Incidence angle dependence of the statistical properties of C-band HH-polarization backscattering signatures of the Baltic Sea ice, IEEE T. Geosci. Remote, 40, 2593–2605, 2002.

Moen, M.-A. N., Doulgeris, A. P., Anfinsen, S. N., Renner, A. H. H., Hughes, N., Gerland, S., and Eltoft, T.: Comparison of feature based segmentation of full polarimetric SAR satellite sea ice images with manually drawn ice charts, The Cryosphere, 7, 1693–1705, doi:10.5194/tc-7-1693-2013, 2013.

Moen, M.-A. N., Anfinsen, S. N., Doulgeris, A. P., Renner, A. H. H., and Gerland, S.: Assessing polarimetric SAR sea-ice classifications using consecutive day images, Ann. Glaciol., 56, 285–294, 2015.

Ochilov, S. and Clausi, D. A.: Operational SAR sea-ice image classification, IEEE T. Geosci. Remote, 50, 4397–4408, 2012.

RADARSAT-2 product description: MacDonald Dettwiler and Associates (MDA), Tech. Rep. Issue 1/8, available at: http://gs.mdacorporation.com/includes/documents/RN-SP-52-1238RS-2ProductDescription1-8_15APR2011.pdf (last access: 1 July 2014), 15 April 2011.

Romeiser, R., Horstmann, J., Caruso, M. J., and Graber, H. C.: A descalloping post-processor for ScanSAR images of ocean scenes, IEEE T. Geosci. Remote, 51, 3259–3272, 2013.

Sandven, S., Kloster, K., Alexandrov, V., Piotrovskaya, N., and Zakhvatkina, N.: Sea ice classification using ASAR Alternating Polarisation images, SeaSAR 2008, 21–24 January 2008, Oslo, Norway, 2008.

Sandven, S., Alexandrov, V., Zakhvatkina, N., and Babiker, M.: Sea ice classification using RADARSAT-2 Dual Polarisation data, SeaSAR 2012, the 4th International Workshop on Advances in SAR Oceanography, 18–22 June 2012, Tromso, Norway, 2012.

Shokr, M. E.: Evaluation of Second-Order Texture Parameters for Sea Ice Classification from Radar Images, J. Geophys. Res., 96, 10625–10640, 1991.

Shokr, M. E.: Compilation of a radar backscatter database of sea ice types and open water using operational analysis of heterogeneous ice regimes, Can. J. Remote Sens., 35, 369–384, 2009.

Soh, L. K. and Tsatsoulis, C.: Texture analysis of SAR sea ice imagery using gray level co-occurrence matrices, IEEE T. Geosci. Remote, 37, 780–795, 1999.

Soh, L. K., Tsatsoulis, C., Gineris, D., and Bertoia, C.: ARKTOS: An intelligent system for SAR sea ice image classification, IEEE T. Geosci. Remote, 42, 229–248, 2004.

Vinje, T. and Finnekåsa, Ø.: The ice transport through the Fram Strait, Norsk Polar institutt Skriffer, 186, 39, 1986.

Yu, Q. and Clausi, D. A.: IRGS: Image segmentation using edge penalties and region growing, IEEE T. Pattern Anal., 30, 2126–2139, 2008.

Yu, P., Qin, A. K., and Clausi, D. A.: Feature extraction of dual-pol SAR imagery for sea ice image segmentation, Can. J. Remote Sens., 38, 352–366, 2012.

Zakhvatkina, N., Alexandrov, V., Johannessen, O. M., Sandven, S., and Frolov, I.: Classification of sea ice types in ENVISAT synthetic aperture radar images, IEEE T. Geosci. Remote, 51, 2587–2600, 2013.

C | PUBLICATION III

OPEN-SOURCE FEATURE-TRACKING ALGORITHM FOR SEA ICE DRIFT RETRIEVAL FROM SENTINEL-1 SAR IMAGERY

Stefan Muckenhuber[1], Anton Korosov[1] and Stein Sandven[1]

III

1 Nansen Environmental and Remote Sensing Center (NERSC), Thormøhlensgate 47, 5006 Bergen, Norway

The Cryosphere, 10, 913–925, 2016
www.the-cryosphere.net/10/913/2016/
doi:10.5194/tc-10-913-2016

The Cryosphere Open Access EGU

Open-source feature-tracking algorithm for sea ice drift retrieval from Sentinel-1 SAR imagery

Stefan Muckenhuber, Anton Andreevich Korosov, and Stein Sandven

Nansen Environmental and Remote Sensing Center (NERSC), Thormøhlensgate 47, 5006 Bergen, Norway

Correspondence to: Stefan Muckenhuber (stefan.muckenhuber@nersc.no)

Received: 19 November 2015 – Published in The Cryosphere Discuss.: 21 December 2015
Revised: 15 April 2016 – Accepted: 19 April 2016 – Published: 26 April 2016

Abstract. A computationally efficient, open-source feature-tracking algorithm, called ORB, is adopted and tuned for sea ice drift retrieval from Sentinel-1 SAR (Synthetic Aperture Radar) images. The most suitable setting and parameter values have been found using four Sentinel-1 image pairs representative of sea ice conditions between Greenland and Severnaya Zemlya during winter and spring. The performance of the algorithm is compared to two other feature-tracking algorithms, namely SIFT (Scale-Invariant Feature Transform) and SURF (Speeded-Up Robust Features). Having been applied to 43 test image pairs acquired over Fram Strait and the north-east of Greenland, the tuned ORB (Oriented FAST and Rotated BRIEF) algorithm produces the highest number of vectors (177 513, SIFT: 43 260 and SURF: 25 113), while being computationally most efficient (66 s, SIFT: 182 s and SURF: 99 s per image pair using a 2.7 GHz processor with 8 GB memory). For validation purposes, 314 manually drawn vectors have been compared with the closest calculated vectors, and the resulting root mean square error of ice drift is 563 m. All test image pairs show a significantly better performance of the HV (horizontal transmit, vertical receive) channel due to higher informativeness. On average, around four times as many vectors have been found using HV polarization. All software requirements necessary for applying the presented feature-tracking algorithm are open source to ensure a free and easy implementation.

1 Introduction

Sea ice motion is an essential variable to observe from remote sensing data, because it strongly influences the distribution of sea ice on different spatial and temporal scales. Ice drift causes advection of ice from one region to another and export of ice from the Arctic Ocean to the sub-Arctic seas. Antarctic sea ice is even more mobile and its strong seasonality is linked to the ice transport from high to low latitudes (IPCC, 2013). Furthermore, ice drift generates convergence and divergence zones that cause formation of ridges and leads. However, there is still a lack of extensive sea ice drift data sets with sufficient resolution to estimate convergence and divergence on a spatial scaling of less than 5 km.

The regions of interest are the ice-covered seas between Greenland and Severnaya Zemlya, i.e. the Greenland Sea, Barents Sea, Kara Sea and the adjacent part of the Arctic Ocean. This area is characterized by a strong seasonal cycle of sea ice cover, a large variation of different ice classes (multiyear ice, first-year ice, marginal ice zone etc.) and a wide range of drift speeds (e.g. strong ice drift in Fram Strait).

With systematic acquisition of space-borne Synthetic Aperture Radar (SAR) data over sea ice areas, Kwok et al. (1990) have demonstrated that high-resolution ice drift fields can be derived from SAR data. SAR is an active microwave radar which acquires data independently of solar illumination and weather conditions. Sea ice motion fields of the Arctic Ocean with a grid spacing of 5 km have been produced on a weekly basis between 1997–2012 using Radarsat and ENVISAT (Environmental Satellite) SAR data and the geophysical processor system introduced by Kwok et al. (1990). Thomas et al. (2008a) have used pattern recognition to calculate sea ice drift between successive ERS-1 (European remote-sensing satellite) SAR images with a resolution of 400 m. This work has been continued by Hollands and Dierking (2011) using Advanced SAR (ASAR) data from ENVISAT. Komarov and Barber (2014) used a similar pattern-

matching technique to evaluate ice motion results from dual-polarization Radarsat-2 images.

With the successful launch of Sentinel-1A in April 2014 and the planned launch of Sentinel-1B in early 2016, high-resolution SAR data will be delivered for the first time with open and free access for all users and unprecedented revisit time of less than one day in the Arctic (ESA, 2012). This introduces a new era in SAR Earth observation. Sea ice drift data with medium resolution (10 km) are provided operationally via the Copernicus Marine Environment Monitoring Service (CMEMS, http://marine.copernicus.eu), but no sea ice drift algorithm using Sentinel-1 data has been published so far. The objective of this paper is to identify and develop the most efficient open-source algorithm for high-resolution sea ice drift retrieval from Sentinel-1 data.

Our goal is to exploit recent improvements and developments in computer vision by adopting a state-of-the-art feature-tracking algorithm to derive sea ice drift (i.e. vectors of sea ice displacement). Current pattern-matching algorithms constrain the high-resolution vectors with low-resolution estimates for practical reasons. Using feature tracking, drift vectors can be derived independently from the surrounding motion, which leads to better performance e.g. along shear zones. For application on large data sets and for operational use, we considered a computationally efficient algorithm, called ORB (Oriented FAST and Rotated BRIEF) (Rublee et al., 2011), tuned it for sea ice drift retrieval from Sentinel-1 imagery and compared the results with other available feature-tracking algorithms and existing sea ice drift products.

The software requirements necessary for deriving ice drift fields from Sentinel-1 data (Python with OpenCV and the Python toolbox Nansat) are all open source to ensure a free, user friendly and easy implementation.

The paper is organized as follows: Sect. 2 introduces the used Sentinel-1A data product. The ORB algorithm description and the used methods for tuning, comparison and validation are presented in Sect. 3. The recommended parameter set including the tuning, comparison and validation results are provided in Sect. 4. The discussion can be found in Sect. 5.

2 Data

The Sentinel-1 mission, an initiative of the European Union and operated by the European Space Agency (ESA), is composed of a constellation of two identical satellites sharing the same near-polar, sun-synchronous orbit: Sentinel-1A, launched in April 2014, and Sentinel-1B, planned to launch in early 2016. Sentinel-1 carries a single C-band Synthetic Aperture Radar (SAR) instrument measuring radar backscatter at a centre frequency of 5.405 GHz and supporting dual polarization (HH + HV, VV + VH). With both satellites operating, the constellation will have a revisit time of less than one day in the Arctic. Radar data are delivered to Copernicus services within an hour of acquisition with open and free access for all users (ESA, 2012).

The Sentinel-1 product used in this paper is called Extra-wide Swath Mode Ground Range Detected with Medium Resolution. These images cover an area of 400 km × 400 km with a pixel spacing of 40 m × 40 m (resolution: 93 m range × 87 m azimuth; residual planimetric distortions: within 10 m; Schubert et al., 2014) and provide both HH (horizontal transmit, horizontal receive) and HV (horizontal transmit, vertical receive) polarization.

Four image pairs (Table 1) representative of our region of interest have been chosen for parameter tuning. Furthermore, 43 image pairs acquired over Fram Strait and north-east of Greenland (Fig. 8) have been used to test the performance of different feature-tracking algorithms. To ensure an independent evaluation, the 43 test image pairs have not been used for parameter tuning. The two considered sets of image pairs cover both a range of different sea ice conditions (pack ice, fast ice, leads, ridges, marginal ice zone, ice edge etc.) and intervals between the acquisitions. We focused on winter and spring data, since our area of interest experiences the highest sea ice cover during this period.

3 Method

Sentinel-1 data sets were opened and processed with the open-source software Nansat (see Appendix A; Korosov et al., 2015, 2016). Nansat is a scientist-friendly Python toolbox for processing 2-D satellite Earth observation data. It is based on the Geospatial Data Abstraction Library (GDAL) and provides easy access to geospatial data, a simple and generic interface to common operations including reading, geographic transformation and export. Nansat proves to be efficient both for development and testing of scientific algorithms and for fast operational processing. To extend the functionality of GDAL, Nansat reads metadata from XML files accompanying Sentinel-1 data and supplements the GDAL data model with georeference information stored as ground control points (GCPs). Originally GCPs are pairs of latitude/longitude and corresponding pixel/line coordinates. In order to increase the accuracy of the geographic transformation, the projection of GCPs is changed from cylindrical to stereographic, placed at the centre of the scene. The reprojected GCPs are then used by GDAL to calculate geographic coordinates of any pixel in the raster using spline interpolation. Reprojection of GCPs does not require much additional computational effort, but improves the result significantly, particularly at high latitudes.

The normalized radar cross section (σ^0) is calculated from raw Sentinel 1A data using the following equation:

$$\sigma^0 = \mathrm{DN}_i^2 / A_i^2, \quad (1)$$

where DN_i is the digital number provided in the source TIFF file, A_i is the value of normalization coefficient from the ac-

Table 1. Sentinel-1 image pairs used for parameter tuning.

Region	First image acquisition time, UTC	Second image acquisition time, UTC	Time gap
Fram Strait	28 Mar 2015 07:44:33	29 Mar 2015 16:34:52	33 h
Svalbard North	22 Apr 2015 06:46:23	23 Apr 2015 13:59:03	31 h
Franz Josef Land	24 Mar 2015 03:21:13	24 Mar 2015 11:30:06	8 h
Kara Sea	22 Apr 2015 11:37:16	24 Apr 2015 11:20:59	48 h

companying calibration metadata and i is an index of a pixel (Anonymous, 2014). No additional preprocessing of SAR data was performed.

Our algorithm for sea ice drift detection includes three main steps: (a) resampling of raw data to lower resolution, (b) detection and matching of features and (c) comparison/validation.

a. To decrease the influence of speckle noise and increase the computational efficiency, the resolution is reduced before applying the ice drift algorithm from 40 to 80 m pixel spacing using simple averaging.

b. For detection and tracking of features on large data sets and for operational use, a computationally efficient algorithm, called ORB (Rublee et al., 2011), has been used. In our numerical experiments we tuned the parameters of ORB for optimal SAR sea ice drift application. The most suitable parameter set (including spatial resolution of SAR image, patch size of FAST descriptor, number of pyramid levels, scale factor, etc.) has been evaluated for our area and season of interest.

c. The introduced ORB set-up is compared to other available OpenCV feature-tracking algorithms, CMEMS data and manually drawn vectors for performance appraisal and validation.

3.1 ORB algorithm

ORB (Oriented FAST and Rotated BRIEF) is a feature-tracking algorithm introduced by Rublee et al. (2011) as "a computationally efficient replacement to Scale-Invariant Feature Transform (SIFT) that has similar matching performance, is less affected by image noise, and is capable of being used for real-time performance". ORB builds on the FAST keypoint detector (Rosten and Drummond, 2006) and the binary BRIEF descriptor (Calonder et al., 2010) with many modifications to enhance the performance. It uses FAST to find multiscale keypoints on several pyramid levels and applies a Harris corner measure (Harris and Stephens, 1988) to pick the best keypoints. To achieve rotation invariance, the orientation of the keypoint is calculated by using the intensity-weighted centroid of a circular patch with the located keypoint at the centre. Rublee et al. (2011) states that the ORB descriptor performance is equal to SIFT (Lowe, 2004) and higher than Speeded-Up Robust Features (SURF) (Bay et al., 2006). Like Rublee et al. (2011), we use a brute-force matcher and Hamming distance for feature matching. Unlike SIFT and SURF, ORB is an open-source software and use and distribution are not limited by any licenses.

Before the feature-tracking algorithm can be applied to a satellite image, the SAR backscatter values σ^0 have to be transformed into the intensity i range ($0 \le i \le 255$ for $i \in \mathbb{R}$) used in OpenCV. This transformation is done by using Eq. (2) and setting all intensity values below and above the range to 0 and 255.

$$i = 255 \cdot \frac{\sigma^0 - \sigma^0_{\min}}{\sigma^0_{\max} - \sigma^0_{\min}}, \tag{2}$$

Lower and upper brightness boundaries $\sigma^0_{\min}$ and $\sigma^0_{\max}$ are user defined and chosen to be constant in order to limit the influence of speckle noise and be independent e.g. of high backscatter values σ^0 over land. Converting the linear backscatter values before the transformation into decibel units has been tested, but decreased the algorithm performance for both channels.

After the transformation into intensity values, keypoints are detected on both SAR scenes using the FAST-9 keypoint detector (Rosten and Drummond, 2006). FAST-9 compares the intensity I_p of a centre pixel to the intensities of pixels on the surrounding circle with a perimeter of 16 pixels (Fig. 1). If there exists a set of nine contiguous pixels in the circle which are all brighter than $I_p + t$, or all darker than $I_p - t$, the centre pixel is recognized as a keypoint. The threshold t is set low enough to get more than the predefined amount N of keypoints.

To detect features of different scales, the keypoint search is performed on several pyramid levels. The number of pyramid levels in combination with the scale factor defines the range and increment of the keypoint detection scaling. A scale factor of 2 means that each next pyramid level has four times fewer pixels, but such a large-scale factor degrades the feature matching score. On the other hand, a small-scale factor close to 1 means to cover a certain scale range needs more pyramid levels and hence, the computational cost increases.

FAST does not produce a measure of cornerness and Rublee et al. (2011) have found that it has large responses along edges. Harris corner measure (Harris and Stephens, 1988) is used to order the FAST keypoints according to their

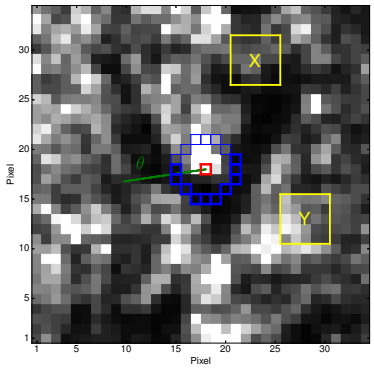

Figure 1. Subset of the first image from Fram Strait pair (Table 1) with centre at 2.31° W, 81.70° N and pixel spacing of 80 m. The centre pixel (red) is recognized as keypoint since $\geqslant 9$ contiguous pixels (bold blue) of the surrounding blue circle have intensity values smaller than the centre minus threshold t. The orientation θ of the keypoint is shown with a green arrow. The displayed area (34 × 34 pixels) around the keypoint represents the considered patch p used for feature description. The yellow 5 × 5 pixels subwindows X and Y are an example for a possible binary test sampling pair with $p(X) < p(Y)$ and hence, $\tau(p; X, Y) = 1$ (Eq. 7).

cornerness and reject less reliable keypoints. Considering a window $w(x, y)$ around the keypoint, the intensity derivatives I_x, I_y in x and y direction can be written in a matrix $\mathbf{M}$:

$$\mathbf{M} = \sum_{x,y} w(x,y) \begin{bmatrix} I_x^2 & I_x I_y \\ I_x I_y & I_y^2 \end{bmatrix}. \tag{3}$$

The eigenvalues λ_1 and λ_2 of $\mathbf{M}$ contain the intensity derivative in the direction of the fastest and slowest change respectively. Based on λ_1 and λ_2, a score R can be calculated for each keypoint:

$$R = \lambda_1\lambda_2 - k(\lambda_1 + \lambda_2)^2, \tag{4}$$

with k being an empirical constant. A high intensity variation in both dimensions returns a high R value. The top N keypoints with the highest R values are used and the rest is rejected.

FAST does not include orientation, but ORB adds a direction to each keypoint using the intensity-weighted centroid from Rosin (1999). The moments m_{pq} of a circular area around the keypoint are used:

$$m_{pq} = \sum_{x,y} x^p y^q I(x,y). \tag{5}$$

The intensity-weighted centroid has its location at the following:

$$C = \left(\frac{m_{01}}{m_{00}}, \frac{m_{10}}{m_{00}} \right). \tag{6}$$

The orientation θ (e.g. green arrow in Fig. 1) represents the direction of the vector connecting the keypoint with the intensity-weighted centroid. The moments m_{pq} are computed with x and y remaining within a circular region of radius r, where r is chosen to be the size of the patch p used for the following feature description Rublee et al. (2011).

After locating and adding orientation to the best N keypoints, a patch p around each keypoint is used for feature description (NB: keypoint refers to 1 pixel, feature refers to description of p). ORB applies a modified version of the binary descriptor BRIEF (Calonder et al., 2010). Rublee et al. (2011) defines a binary test τ for a patch p as follows:

$$\tau(p; X, Y) := \begin{cases} 1 & \text{if } p(X) < p(Y) \\ 0 & \text{if } p(X) \geq p(Y), \end{cases} \tag{7}$$

with $p(X)$ and $p(Y)$ being the intensities at test points X and Y. ORB uses 5 × 5 sub-windows as test points (e.g. in Fig. 1). Applying n binary tests on a single patch, Rublee et al. (2011) derive a binary feature vector $\boldsymbol{f}$:

$$\boldsymbol{f}_n(p) := \sum_{1 \leq i \leq n} 2^{i-1} \tau(p; X_i, Y_i). \tag{8}$$

The considered set of n binary tests with test points (X_i, Y_i) can be written in a $2 \times n$ matrix (Rublee et al., 2011):

$$\mathbf{S} = \begin{pmatrix} X_1, & \ldots, & X_n \\ Y_1, & \ldots, & Y_n \end{pmatrix}. \tag{9}$$

To be invariant to in-plane rotation, Rublee et al. (2011) steers $\mathbf{S}$ according to the orientation θ using the corresponding rotation matrix $\mathbf{R}_\theta$:

$$\mathbf{S}_\theta = \mathbf{R}_\theta \mathbf{S}. \tag{10}$$

A good set $\mathbf{S}$ of sampling pairs needs to be uncorrelated, so that each pair adds new information to the descriptor and they must have high variance to make features more discriminative. Rublee et al. (2011) applied a greedy search to a large training data set to obtain a set for ORB with $n = 256$ relatively uncorrelated tests with high variance.

After the feature description, OpenCV allows different matching procedures for ORB. Like Rublee et al. (2011), we use brute-force matching and compare each feature of the first image to all features in the second image.

As a comparison measure, we use the Hamming distance, which is equal to the number of positions in which the two considered feature vectors have a different value.

$$\begin{aligned} \boldsymbol{b}_1 &= 1011101 \\ \boldsymbol{b}_2 &= 1001001, \end{aligned} \tag{11}$$

For example, comparing the two binary vectors $\boldsymbol{b}_1$ and $\boldsymbol{b}_2$ returns the Hamming distance $d = 2$, since the third and fifth position have a different value.

Our setting returns the best two matches and applies the ratio test from Lowe (2004) to decide whether the best match

is accepted or rejected. The match is accepted if ratio of the distances $\frac{d_1}{d_2} <$ is below a given threshold. The ratio test eliminates a high number of false matches, while discarding only few correct matches.

3.2 ORB setting and parameter tuning

Achieving the best possible performance of ORB for sea ice drift from Sentinel-1 images requires a good setting and tuning of the parameters shown in Table 2.

It is not recommended to reproject one image onto the projection of the second image before applying the ORB algorithm, since this is computationally very expensive. Instead, geographic coordinates of the matched start and end point shall be calculated independently using the georeference information from GCPs of the first and second image.

Manual interpretation of ice drift results (using the training data from Table 1) reveals that a good compromise between amount of vectors and correct results can be achieved with a Lowe ratio test threshold equal to 0.75. That means that the Hamming distance of the best match has to be less than $0.75 \times$ Hamming distance of the second best match. Tested on the image pairs from Table 1, the ratio test showed a clearly better performance and is computationally less expensive than the alternative cross-check, where features are matched in both directions (first image to second image and vice versa) and rejected if the drift vectors are too different.

Unreasonably high sea ice displacements (e.g. above 40 km for a time difference between two scenes of ~ 30 h) are removed in a post-processing step from the drift field. In addition, displacements below 2.5 km are rejected during the testing to disregard matches over land. This does not influence the number of correct matches, since the sea ice displacement in all considered test images is above 2.5 km.

Based on our observations we assume that the proportion of wrong matches does not increase with increasing total number of matches. Under this assumption the algorithm performance refers to the total number of matches and is used to tune the algorithm parameters in Table 2. ORB is computationally more efficient, enabling testing the parameters over a wide range with high-resolution using both HH and HV polarization.

As a starting point, the tested parameters were set as follows: resize factor = 0.5, patch size = 31, pyramid levels = 8, scale factor = 1.2, HH limits = [0,0.12], HV limits = [0, 0.012] and ratio test = 0.8. As a compromise between performance and computational efficiency, the maximum amount of retained keypoints is set to 100 000. Tested range and parameter meaning are shown in Table 2.

In order to find an optimal value for the tested parameter, it is varied in a reasonable range, the feature-tracking algorithm is applied and the total number of matched vectors is found. Once the most suitable value for a tested parameter is found, it is applied for further testing.

3.3 Comparison of ORB to SIFT and SURF

The presented ORB algorithm has been compared to other OpenCV feature-tracking algorithms, namely SIFT (Lowe, 2004) and SURF (Bay et al., 2006), using 43 image pairs acquired over Fram Strait and north-east of Greenland (Fig. 8). SIFT and SURF were used in standard mode and the framework conditions were set to equal for the comparison. Image preprocessing has been carried out as described above, brute-force matching including the Lowe ratio test with threshold 0.75 has been applied for all three algorithms as well as the removal of unreasonably high sea ice displacements in a post-processing step. Since SIFT allows for defining the number of retained keypoints, this parameter has been set to 100 000 as done for ORB. The further tuning of SIFT and SURF is not the aim of this paper, since these two algorithms are not open source and computationally less efficient.

The distribution and reliability of the calculated vector fields have been assessed for each image pair using two parameters on a grid with cell size 1° longitude × 0.2° latitude: number of derived vectors per grid cell (N) and root mean square distance (D) of all vectors in a gird cell computed as follows:

$$D = \frac{\sqrt{\sum_i (u_i - \widetilde{u})^2 + (v_i - \widetilde{v})^2}}{N}, \tag{12}$$

where i is the index of a vector inside the grid cell, u_i and v_i are the eastward and northward drift components and $\widetilde{u}$, $\widetilde{v}$ the corresponding mean values. To combine the results of several image pairs, the sum of N and the mean of D is considered.

3.4 Validation

The ORB algorithm has been validated against drift data from two independent sources using the image pair Fram Strait (Table 1). First, 350 features were identified by a sea ice expert in both images and manually connected using ArcGIS. Second, sea ice drift vectors were taken from the Copernicus Marine Environment Monitoring Service (CMEMS, http://marine.copernicus.eu). The SAR ice drift product of CMEMS is operated by the Technical University of Denmark (DTU) and drift data are provided with a resolution of 10 km using pattern-matching techniques (Pederson et al., 2015, http://www.seaice.dk/).

Since the starting locations of ORB, manual and CMEMS vectors do not coincide, the corresponding (ORB) reference vectors were found as nearest neighbours within 5 km radius from the (CMEMS or manual) validation vectors.

Three parameters were considered for the comparison: root mean square error (E), slope (S) and offset (O) of the linear fit between the reference and validation vectors. E was calculated as follows:

Table 2. Recommended set of parameters for retrieval of sea ice drift from Sentinel-1 data using ORB.

Parameter	Meaning	Tested range (increment)	Recommended setting
Amount keypoints	Maximum number of keypoints to retain	–	100 000
Resize factor	Resolution reduction during pre-processing	0.5–1 (0.5)	0.5
Patch size	Size of descriptor patch in pixels	10–60 (1)	34
Pyramid levels	Number of pyramid levels	1–15 (1)	7
Scale factor	Pyramid decimation ratio	1.1–1.4 (0.1)	1.2
$[\sigma^0_{\min}, \sigma^0_{\max}]$ (HH)	Brightness boundaries for HH channel	[0–0.04, 0.01–0.2] (0.01)	[0, 0.08]
$[\sigma^0_{\min}, \sigma^0_{\max}]$ (HV)	Brightness boundaries for HV channel	[0–0.007, 0.001–0.02] (0.001)	[0, 0.013]
Ratio test	Threshold for ratio test	0.5–1 (0.1), 0.7–0.8 (0.01)	0.75

$$E = \frac{\sqrt{\sum_i (u_i - U_i)^2 + (v_i - V_i)^2}}{n}, \quad (13)$$

where i is the index of a vector pair (reference and validation vector) inside the entire sample, u_i and v_i are eastward and northward drift components of the validation vector, U_i and V_i are eastward and northward components of the reference vector and n is the number of vector pairs.

In addition, the CMEMS data have been validated against manual vectors in order to understand the credibility of the reference data.

4 Results

4.1 ORB parameter tuning

Table 2 shows the recommended parameter set for ORB Sentinel-1 sea ice drift application for our region and period of interest. Using these parameters yielded the best compromise between performance and computational efficiency for the four representative image pairs from Table 1.

4.1.1 Patch size

Figure 2 shows that changing the size (length and width) of the considered patch p between 10 and 60 pixels can modify the resulting amount of vectors by an order of magnitude. To resolve drift gradients with high resolution, the patch size shall be as small as possible. Taking this into account and the performance represented by the amount of matches, the most suitable patch size was chosen to be 34 pixels. For our training data set (Table 1), this yields on average around 1 and 4 vectors per 10 km^2 for HH and HV respectively. The four image pairs respond similar to a patch size variation. Franz Josef Land has the highest number of HH matches and the lowest for HV.

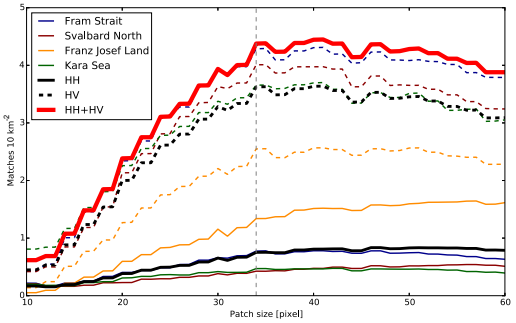

Figure 2. Patch size of descriptor vs. number of matches of the four test image pairs from Table 1. Solid and dashed lines represent results for HH and HV polarization respectively. Mean values of the four image pairs are shown in black and the sum of the mean values in red. Vertical grey line at 34 pixels represents chosen parameter.

4.1.2 Brightness boundaries

The performance of the algorithm (represented by the amount of matches) for different backscatter limits $\sigma^0_{\max}$ (Eq. 2) for HH and HV polarization is shown in Fig. 3. Within the chosen backscatter range, the amount of vectors can vary by an order of magnitude. As a compromise between the different results of the four image pairs, we suggest setting the upper brightness boundary $\sigma^0_{\max}$ to 0.08 and 0.013 for HH and HV. The chosen lower boundary $\sigma^0_{\min}$ is 0 for both HH and HV, because the number of matches decreases for increasing values of $\sigma^0_{\min}$ (not shown). Applying this setting on the training data set yields on average around 1 and 4 vectors per 10 km^2 for HH and HV.

4.1.3 Pyramid levels and scale factor

We calculated the number of matches using 1 to 14 pyramid levels and the scale factors 1.1, 1.2, 1.3 and 1.4. As a compromise between performance, i.e. number of matches, and computational efficiency (linked to the number of pyramid

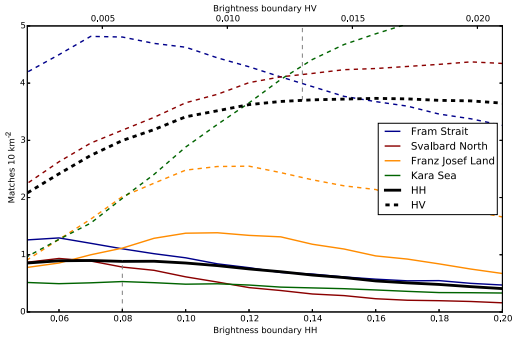

Figure 3. Upper brightness boundary $\sigma^0_{\max}$ (Eq. 2) vs. number of matches of the four test image pairs from Table 1. Solid and dashed lines represent results for HH and HV respectively. Black lines are the mean values of the four image pairs. Vertical grey lines at 0.08 (HH) and 0.013 (HV) represent chosen parameters.

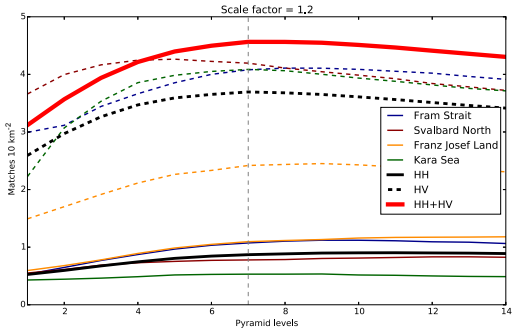

Figure 4. Number of pyramid levels vs. number of matches of the four test image pairs from Table 1 for a scale factor of 1.2. Solid and dashed lines represent results for HH and HV polarization. Mean values are shown in black and the sum of the mean values in red. Vertical grey line at 7 represents chosen number of pyramid levels.

levels), a scale factor of 1.2 with seven pyramid levels was chosen. As shown in Fig. 4, the number of matches does not increase significantly when using more than seven pyramid levels and even decreases towards 14 pyramid levels.

4.2 HH and HV comparison

Figures 2, 3 and 4 display the HH and HV results with solid and dashed lines. All image pairs show significantly better performance of the HV channel. On average, around four times as many vectors have been found using HV. Even the image pair Franz Josef Land (Table 1), which has the best HH and the worst HV performance, shows more than two times as many vectors using HV channel. However, due to the different appearance of sea ice in the HH and HV image, the spatial distribution of the resulting drift vectors is also slightly different.

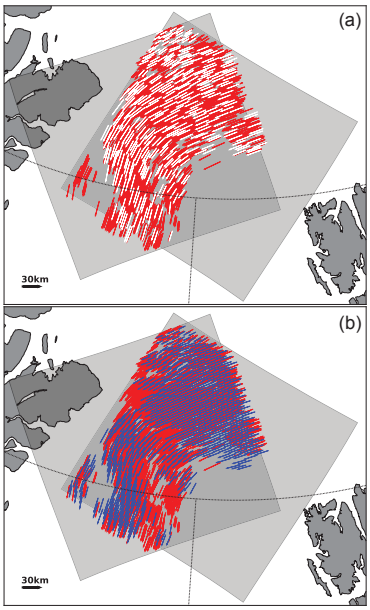

Figure 5. Sea ice drift of the Sentinel-1 image pair Fram Strait (Table 1). **(a)** Manually drawn vectors are shown in white and the computed ORB vectors in red. **(b)** shows ORB vectors in comparison to the drift vectors from the CMEMS/DTU data (blue).

Figure 6 shows the spatial distribution of identified keypoints and matched features in a 200 × 200 pixels sub-image from image pair Fram Strait (Table 1). The results for HH and HV are displayed in two separate panels. The density of identified keypoints in HH (11 keypoints per 10 × 10 pixels window) is in the same order of magnitude as in HV (15 keypoints per 10 × 10 pixels window). This is expected, since the number of retained keypoints for both channels is set to 100 000 for the entire scene. However, the number of matched features in HH is significantly lower (0.15 features per 10 × 10 pixels window) than in HV (1.6 features per 10 × 10 pixels window). The observed difference in matching success can be explained by looking at the frequency distribution of the radar backscatter standard deviation in a sliding window with same size as used for feature description (34 × 34 pixels). The comparison in Fig. 7 shows that HH provides a few windows with very high variability, i.e. high standard deviation, but the majority have very low backscatter variability (sharp peak with mode 20). On the HV image, however, most of the windows have a medium to high backscatter variability (wide peak with mode 25) which is more favourable for keypoint detection.

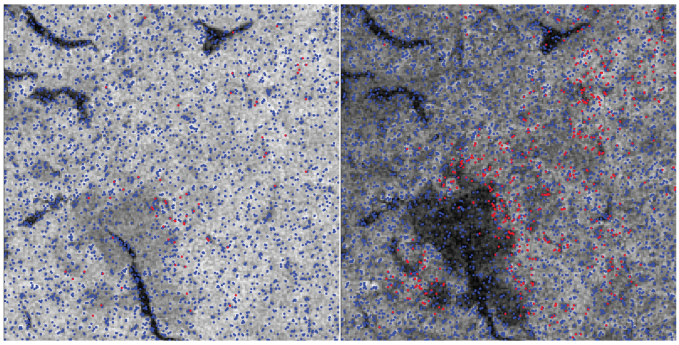

Figure 6. Identified keypoints (blue) and matched features (red) on a 200 × 200 pixels sub-image from the pack ice area in image pair Fram Strait (Table 1). Results of HH are shown in the left panel and HV in the right panel.

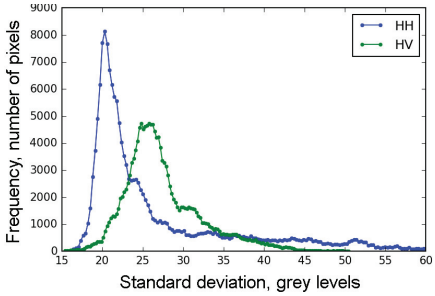

Figure 7. Frequency distribution of radar backscatter standard deviation using a 34 × 34 pixels sliding window (step = 1 pixel) on a 1000 × 1000 pixels sub-image from image pair Fram Strait (Table 1). The radar backscatter is scaled to range 0–255 using Eq. (2). The considered sub-image covers pack ice, marginal ice zone and small parts of open water. Results for HH are shown in blue and HV in green.

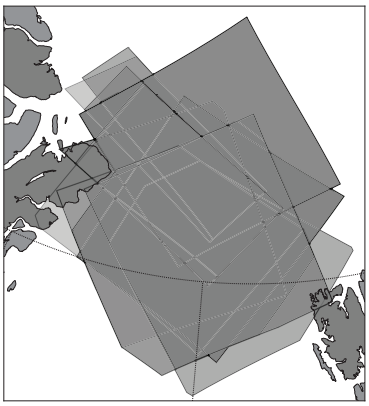

Figure 8. Overlapping area of 43 Sentinel-1 image pairs used to compare ORB, SIFT and SURF. The image pairs have been acquired between 2 January and 21 March 2015 with time gaps varying between 7 and 48 h.

4.3 Comparison with SIFT and SURF

A total of 177 513, 43 260 and 25 113 vectors are found for the 43 test image pairs (Fig. 8) using ORB, SIFT and SURF respectively (Fig. 9a). Comparing the vector fields using the sum of N and the mean of D, as described in Sect. 3, shows that ORB covers the largest area with close to 1000 vectors per grid cell and lower root mean square distance values.

Comparing the distributions of N (Q-Q plot in Fig. 10, left panel), shows that ORB derives in all cases around five times as many vectors than SIFT and SURF. The Q-Q plot in the right panel of Fig. 10 considers the distributions of D. For $D < 500$ m, the vectors derived by ORB exhibit a higher variability within one grid cell (slightly higher D), probably due to a larger number of vectors N. For the higher root mean square values ($D > 500$ m), SIFT and SURF vectors are much less consistent than ORB vectors (higher D).

4.4 Computational efficiency

The OpenCV feature-tracking algorithms ORB, SIFT and SURF in combination with the Python toolbox, Nansat, are computationally efficient (total processing time on regular MacBook Pro: 2–4 min) and allow high-resolution sea ice drift retrieval from data sets with large temporal and spatial extent. The processing times shown in Table 3 are based on testing the algorithms on a MacBook Pro from early 2013 with a 2.7 GHz Intel Core i7 processor and 8 GB 1600 MHz DDR3 memory. Applying the introduced ORB algorithm

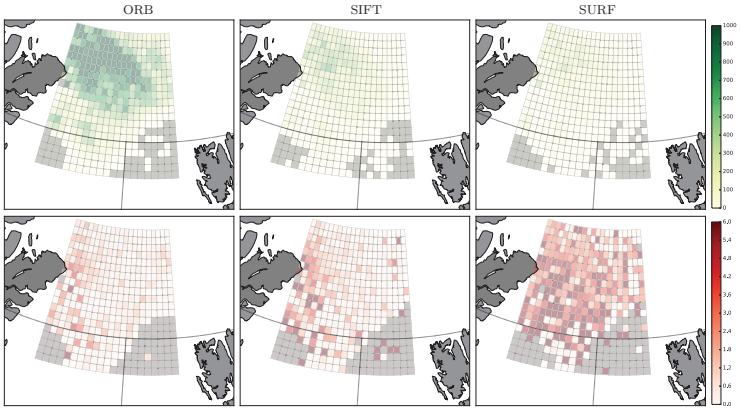

Figure 9. Sea ice drift derived from 43 Sentinel-1 image pairs (Fig. 8) using both HH and HV channel and ORB (first column, 177 513 vectors), SIFT (second column, 43 260 vectors) and SURF (third column, 25 113 vectors) algorithm. The panels show the sum of the number of vectors per grid cell N (green, first row) and mean root mean square distance D in km (red, second row).

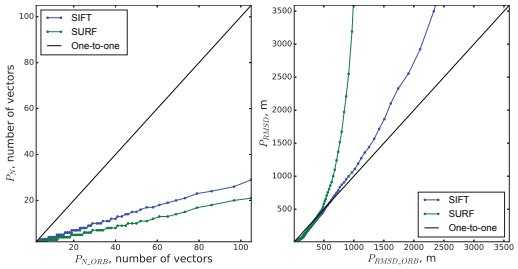

Figure 10. Q-Q plot of number of vectors N (left panel) and root mean square distance D (right panel) from results shown in Fig. 9. Tuned ORB algorithm (x axis) compared to SIFT (y axis, blue dots) and SURF (y axis, green dots).

needs 36 and 67 % of the processing time to compute drift fields with SIFT and SURF.

4.5 Validation

Since reference vectors were searched only within a given radius of the validation vectors, the number of matches decreased for the ORB vs. manual comparison from 350 possible matches to 314, for ORB vs. CMEMS from 560 to 436 and for CMEMS vs. manual from 350 to 201 (Table 4). The average distances between compared vectors were 1702, 2261 and 3440 m for ORB vs. manual, ORB vs. CMEMS and CMEMS vs. manual respectively.

The validation of ORB vectors with manually derived vectors (Fig. 5a, Table 4) reveals a high accuracy of our tuned ORB algorithm with root mean square error $E = 563$ m, slope $S = 1.02$ and offset $O = -372$ m. Given the displacement range for the used image pair of 10–35 km, the relative error of the algorithm (ratio of E to mean drift) is 2.5 %.

Table 3. Processing times for sea ice drift computation from one channel.

Process	Time [s]
Create two Nansat objects from Sentinel-1 image pair	21.1
Read matrixes from two Nansat objects	48.8
Apply feature-tracking algorithm – ORB	65.8
Apply feature-tracking algorithm – SIFT	181.8
Apply feature-tracking algorithm – SURF	98.5

The vector distributions of ORB and CMEMS (Fig. 5b) are similar. ORB covers a larger area in total, but in a few regions only CMEMS provides drift information. The ORB vs. CMEMS comparison gives an error $E = 1641$ m, slope $S = 1.03$ and offset $O = 265$ m (Table 4).

Validating CMEMS using manual data results in the highest root mean square error $E = 1690$ m with slope $S = 0.98$ and offset $O = -415$ m (Table 4) .

Decreasing the threshold radius between reference and validation vectors does not influence the error E significantly but reduces the number of found matching vectors, especially when comparing CMEMS and manual vectors.

5 Discussion and outlook

The open-source feature-tracking algorithm ORB (Oriented FAST and Rotated BRIEF) has been tuned for sea ice drift retrieval from Sentinel-1 SAR imagery and used for processing winter and spring data in the ice-covered oceans between Greenland and Severnaya Zemlya. Validating cal-

Table 4. Comparison of ORB, CMEMS and manually derived sea ice drift data from image pair Fram Strait (Table 1). The total numbers of derived vectors are 6920 (ORB), 560 (CMEMS/DTU) and 350 (manual). The # vector pairs is the number of used vector pairs for comparison, i.e. vector pairs with maximum 5 km distance. The average distance refers to the starting locations of the used reference and validation vectors. E is the root mean square error, S and O are slope and offset of the linear fit.

Algorithm	E [m]	S	O [m]	# vector pairs	Average distance [m]
ORB vs. manual	563	1.02	−372	314	1702 ± 1325
ORB vs. CMEMS	1641	1.03	265	436	2261 ± 1247
CMEMS vs. manual	1690	0.98	−415	201	3440 ± 1105

culated drift results against manually derived vectors, we found that our algorithm ($E_{\mathrm{ORB}} = 563$ m) had a distinctly higher accuracy than the drift data set provided by CMEMS ($E_{\mathrm{CMEMS}} = 1690$ m). The given root mean square errors E represent a combination of three error sources:

- error of manual ice drift identification introduced by the sea ice expert
- difference between derived and reference vector due to different geographical location of the starting point (maximum 5 km)
- actual error of the algorithm.

Hence, the actual error of the tuned ORB algorithm is expected to be even lower than 563 m.

As expected, the application of the tuned ORB algorithm is much more efficient than manual ice drift assessment, e.g. 6920 vectors have been calculated within 3 min, whereas identifying 350 sea ice drift vectors manually takes several hours. The number of calculated vectors can be increased by returning a higher number of keypoints (e.g. 1 000 000). However, the processing time increases proportional to the square of the considered keypoints and the algorithm performance becomes suboptimal at some point.

The presented ORB algorithm also outperforms other available feature-tracking algorithms, such as SIFT and SURF not only in processing time, but also in quantity and quality of drift vectors, measured by the two introduced indexes N and D. This proves that ORB is the best option for feature-tracking of sea ice on Sentinel-1 SAR imagery.

The algorithm tuning has been performed using winter and spring data, since our area of interest experiences the highest sea ice cover during this period. During summer and autumn, most considered areas have very little or no ice cover (e.g. Barents Sea and Kara Sea), making ice drift calculation during this period less meaningful. Nevertheless, some areas, like the western Fram Strait, experience sea ice cover during the entire year. Dependence of the algorithm performance on the season needs to be evaluated in future work. Computing sea ice drift from summer and autumn data is expected to be more demanding, since features might be destroyed by melting.

Comparing the four considered image pairs, Franz Josef Land yields the highest number of HH matches, accompanied by the lowest number from HV channel. A distinctly shorter time difference between the acquisitions (8 h for Franz Josef Land compared to more than 30 for the other image pairs) might be one reason for an improved HH performance. That would conclude that HH features are less preserved over time and increasing the repeat frequency of the satellite (as planned with Sentinel-1B) will improve the algorithm performance, in particular for the HH channel. The sea ice conditions are another important factor when comparing the algorithm performance for different scenes. The image pair Fram Strait includes the marginal ice zone in the eastern part and multiyear ice in the north-west. Not many matches are expected in the marginal ice zone, but the multiyear ice includes more stable deformation pattern, like ridges, that lead to a good feature-tracking performance. The image pair Svalbard North includes a very small part of the marginal ice zone and the major part is comparable homogeneous pack ice with long cracks along a prevailing direction. Franz Josef Land and Kara Sea are clearly less homogeneous and show a mixture of ice floes with different scales and newly formed young ice. This paper has focused on finding the most suitable algorithm for a range of ice conditions found in the considered area and we can give an idea how ice conditions and acquisition time might affect the ORB feature-tracking performance. Further investigations need to be carried out in order to evaluate the algorithm performance for different ice conditions and other areas like the Beaufort Sea or Antarctica.

Komarov and Barber (2014) have evaluated sea ice drift results from dual-polarization Radarsat-2 imagery using a combination of phase and cross-correlation. Comparing the polarization channels, HH is more sensitive to small-scale roughness, whereas the HV channel provides more stable, large-scale features linked to ice topography. Komarov and Barber (2014) concludes that the combination of HH and HV is beneficial, since more reliable vectors are provided and the vector distributions complement each other. They also found that noise floor stripes in the HV images do not affect the motion tracking from pattern matching. We can extent this discussion for feature based algorithms. Using noise removal for HV and angular correction for HH has been tested, but did not improve the feature-tracking results, i.e. a lower number of vectors has been found. Like Komarov and Barber (2014), we recommend the usage of both channels since the vector distributions are complementary. However, using feature tracking, HV provides about four times as many vectors than HH, making HV the more informative channel. The different performance can be explained by a higher variability of the HV backscatter intensity, considering a window with the same size as used for feature description (34×34 pix).

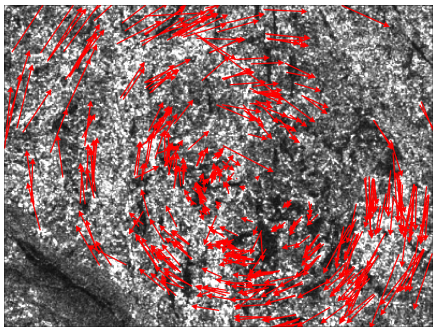

Figure 11. Sea ice drift anomaly (compared to mean drift of the scene) detected in a 300×400 pix (24×32 km) sub-image from Fram Strait (Table 1) close to the marginal ice zone.

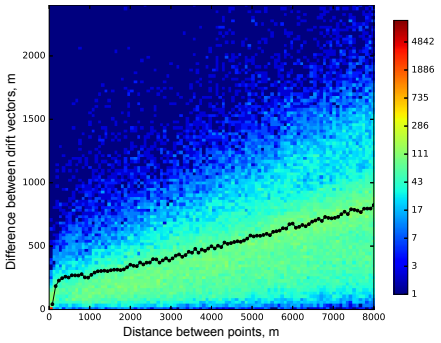

Figure 12. Variogram of drift vectors (black line) on top of 2-D histogram of distance between vectors and difference between vectors estimated from vectors identified on the Sentinel-1 image pair Fram Strait (Table 1). Colour of the 2-D histogram indicates the number of vectors.

Contemporary algorithms for calculating sea ice drift vectors from consecutive image pairs are based either on feature tracking or pattern matching. The feature-tracking approach detects keypoints on two images based solely on the backscatter distribution of the images without taking other keypoints into account. Hence, ORB identifies the keypoints independently. Based on the keypoint locations, the binary feature vectors are calculated. During the second step, all features in the first images are compared to all features in the second image without taking drift information from surrounding vectors into account, i.e. the matching of features from one image to the other is also done independently. Although very close keypoints may share some pixels during the feature description process (i.e. overlap of the considered patches around the keypoints), the detection of keypoints and matching of features are done independently. Eventually, feature-tracking vectors are independent of each other in terms of position, lengths and direction, allowing very close drift vectors to point into different directions.

Figure 11 illustrates 430 drift vector anomalies detected in a 300×400 pix (24×32 km) sub-image from Fram Strait (Table 1) close to the marginal ice zone. The anomalies are calculated as the difference to the mean drift of the entire scene. This example shows that very small-scale dynamic processes, such as the observed rotation, can be detected and quantified with the feature-tracking approach.

Common pattern-matching techniques limit the independence of neighbour vectors for practical reasons. First, pattern matching is usually performed on a regular grid, determining the position and distance between vectors. Second, pattern matching often follows a pyramid approach in order to speed up processing (Thomas et al., 2008a): low-resolution drift is initially estimated using large subwindows and large steps. This first guess constrains the following pattern matching to a finer scale. Repeating this procedure increases the resolution of the end product, but length and direction of the high-resolution vectors depend on the low-resolution estimates, i.e. neighbour vectors depend on each other. Although pattern matching can be designed to retrieve independent vectors by varying the extent of the correlation area and the spacing between vectors, for practical reasons the overlap between the correlation areas is usually half the size of the area (Thomas et al., 2008b).

The independence of feature-tracking vectors has positive and negative implications. On one hand, very close vectors that are independent in length and direction allow identification of ice deformation at very high resolution. The variogram (Fig. 12), which shows how vector differences dependent on the distance between them (Cressie, 1993), indicates that very close vectors may differ significantly, although the difference is generally linearly proportional to the distance. On the other hand, feature-tracking vectors are not evenly distributed in space, and large gaps may occur between clouds of densely located vectors. Spatial irregularity is not optimal for systematic detection of divergence and shear zones and calculation of deformation.

Therefore, computationally efficient feature tracking should be complemented by systematic pattern matching to deliver evenly distributed, high-resolution vector fields. Combining the two different drift calculation approaches and making use of the respective advantages is planned as the next step of our research.

Appendix A: Open-source distribution

The presented work is entirely based on open-source software (Python, OpenCV and Nansat) and satellite images with open and free access for all users. Sentinel-1 SAR data can be downloaded at no cost, in near real time under https://scihub.esa.int/dhus/. The used programming language is Python, a free and open-source software available under https://www.python.org. The OpenCV (open-source Computer Vision) programming library includes the ORB algorithm, and a Python-compatible version can be downloaded under http://opencv.org. To handle and read the satellite data, Nansat is used, which is a scientist-friendly Python toolbox for processing 2-D satellite Earth observation data (source code incl. installation description can be found under https://github.com/nansencenter/nansat). The presented sea ice drift algorithm including an application example can be downloaded from https://github.com/nansencenter/sea_ice_drift.

Acknowledgements. This research was supported by the Norwegian Research Council project IceMotion (high-resolution sea-ice motion from synthetical aperture radar using pattern tracking and Doppler shift, project number 239998/F50) and by the European-Russian Centre for cooperation in the Arctic and Sub-Arctic environmental and climate research (EuRuCAS) under the European Commission FP7 programme (INCO-LAB), GA#295068. We thank both developer groups of the ORB feature-tracking algorithm and the Earth observation toolbox Nansat. The used satellite data was provided by the European Space Agency. A special thanks to the three anonymous reviewers, Tim Dunker and Wolfgang Dierking (AWI) for their comments and valuable input that improved the paper.

Edited by: D. Notz

References

Anonymous: https://earth.esa.int/web/sentinel/technical-guides/sentinel-1-sar (last access: 25 April 2016), 2014.

Bay, H., Tuytelaars, T., and Van Gool, L.: Surf: Speeded Up Robust Features, in: Computer Vision – ECCV 2006, 9th European Conference on Computer Vision, Proceedings, Part I, 7–13 May 2006, Graz, Austria, 404–417, doi:10.1007/11744023_32, 2006.

Calonder, M., Lepetit, V., Strecha, C., and Fua, P.: BRIEF: Binary Robust Independent Elementary Features, CVLab, EPFL, Lausanne, Switzerland, 1281–1298, 2010.

Cressie, N.: Statistics for spatial data: Wiley series in probability and statistics, Wiley-Interscience, New York, 15, 105–209, 1993.

ESA: Sentinel-1 ESA's Radar Observatory Mission for GMES Operational Services, ESA Communications, SP-1322/1, ESA, the Netherlands, 15–21, 2012.

Harris C. and Stephens M.: A Combined Corner and Edge Detector, in: Proceedings of the Alvey Vision Conference, edited by: Taylor, C. J., Alvey Vision Club, 23.1–23.6, doi:10.5244/C.2.23, 1988.

Hollands, T. and Dierking, W.: Performance of a multiscale correlation algorithm for the estimation of sea-ice drift from SAR images: initial results, Ann. Glaciol., 52, 311–317, 2011.

IPCC: Climate Change 2013: The Physical Science Basis, in: Contribution of Working Group I to the Fifth Assessment Report of the Intergovernmental Panel on Climate Change, edited by: Stocker, T. F., Qin, D., Plattner, G.-K., Tignor, M., Allen, S. K., Boschung, J., Nauels, A., Xia, Y., Bex, V., and Midgley, P. M., Cambridge University Press, Cambridge, UK and New York, NY, USA, 323–335, doi:10.1017/CBO9781107415324, 2013.

Komarov, A. S. and Barber, D. G.: Sea Ice Motion Tracking From Sequential Dual-Polarization RADARSAT-2 Images, IEEE T. Geosci. Remote, 52, 121–136, doi:10.1109/TGRS.2012.2236845, 2014.

Korosov, A. A., Hansen, M. W., and Yamakava, A.: Nansat – scientist friendly toolbox for processing satellite data, World Ocean Science Congress, Korosov, A. A., Hansen, M. W., and Yamakava, A., 2–8 February, Cochin, India, 2015.

Korosov, A. A. Hansen, W. M., Yamakawa, A., Dagestad, K. F., Vines, A., Riechert, M., Myasoedov, A., Morozov, E. A., and Zakhvatkina, N.: Nansat-0.6.8, Zenodo, doi:10.5281/zenodo.45703, 2016.

Kwok, R., Curlander, J. C., McConnell, R., and Pang, S.: An Ice Motion Tracking System at the Alaska SAR Facility, IEEE J. Ocean. Eng., 15, 44–54, 1990.

Lowe, D. G.: Distinctive image features from scale-invariant keypoints, Int. J. Comput. Vision, 60, 91–110, 2004.

Pedersen, L. T., Saldo, R., and Fenger-Nielsen, R.: Sentinel-1 results: Sea ice operational monitoring, IEEE International Geoscience and Remote Sensing Symposium (IGARSS), 26–31 July 2015, Milan, Italy, 2828–2831, doi:10.1109/IGARSS.2015.7326403, 2015.

Rosin, P. L.: Measuring corner properties, Comput. Vis. Image Und., 73, 291–307, 1999.

Rosten, E. and Drummond, T.: Machine learning for high-speed corner detection, in: Computer Vision – ECCV 2006, 9th European Conference on Computer Vision, Proceedings, Part I, 7–13 May 2006, Graz, Austria, 430–443, doi:10.1007/11744023_34, 2006.

Rublee, E., Rabaud, V., Konolige, K., and Bradski, G.: ORB: an efficient alternative to SIFT or SURF, IEEE I. Conf. Comp. Vis. (ICCV), 6–13 November 2011, Barcelona, Spain, 2564–2571, doi:10.1109/ICCV.2011.6126544, 2011.

Schubert, A., Small, D., Meier, E., Miranda, N., and Geudtner, D.: Spaceborne Sar Product Geolocation Accuracy: A Sentinel-1 Update, IEEE International Geoscience and Remote Sensing Symposium (IGARSS), 13–18 July 2014, Quebec City, QC, 2675–2678, doi:10.1109/IGARSS.2014.6947025, 2014.

Thomas, M., Geiger, C. A., and Kambhamettu, C.: High resolution (400 m) motion characterization of sea ice using ERS-1 SAR imagery, Cold Reg. Sci. Technol., 52, 207–223, 2008a.

Thomas, M., Geiger, C. A., Kannan, P., and Kambhamettu, C.: Streamline Regularization for Large Discontinuous Motion of Sea Ice, in: 2008 IAPR Workshop on Pattern Recognition in Remote Sensing (PRRS 2008), edited by: Aksoy, S. and Younan, N. H., International Association for Pattern Recognition, Institute of Electrical and Electronics Engineers, Inc., Tampa, FL, 1–4, doi:10.1109/PRRS.2008.4783171, 2008b.

D | PUBLICATION IV

OPEN-SOURCE SEA ICE DRIFT ALGORITHM FOR SENTINEL-1 SAR IMAGERY USING A COMBINATION OF FEATURE TRACKING AND PATTERN MATCHING

Stefan Muckenhuber[1] and Stein Sandven[1]

1 Nansen Environmental and Remote Sensing Center (NERSC), Thormøhlensgate 47, 5006 Bergen, Norway

The Cryosphere, 11, 1835–1850, 2017
https://doi.org/10.5194/tc-11-1835-2017

The Cryosphere Open Access EGU

Open-source sea ice drift algorithm for Sentinel-1 SAR imagery using a combination of feature tracking and pattern matching

Stefan Muckenhuber and Stein Sandven

Nansen Environmental and Remote Sensing Center (NERSC), Thormøhlensgate 47, 5006 Bergen, Norway

Correspondence to: Stefan Muckenhuber (stefan.muckenhuber@gmail.com)

Received: 10 November 2016 – Discussion started: 5 December 2016
Revised: 14 June 2017 – Accepted: 8 July 2017 – Published: 7 August 2017

Abstract. An open-source sea ice drift algorithm for Sentinel-1 SAR imagery is introduced based on the combination of feature tracking and pattern matching. Feature tracking produces an initial drift estimate and limits the search area for the consecutive pattern matching, which provides small- to medium-scale drift adjustments and normalised cross-correlation values. The algorithm is designed to combine the two approaches in order to benefit from the respective advantages. The considered feature-tracking method allows for an efficient computation of the drift field and the resulting vectors show a high degree of independence in terms of position, length, direction and rotation. The considered pattern-matching method, on the other hand, allows better control over vector positioning and resolution. The preprocessing of the Sentinel-1 data has been adjusted to retrieve a feature distribution that depends less on SAR backscatter peak values. Applying the algorithm with the recommended parameter setting, sea ice drift retrieval with a vector spacing of 4 km on Sentinel-1 images covering 400 km × 400 km, takes about 4 min on a standard 2.7 GHz processor with 8 GB memory. The corresponding recommended patch size for the pattern-matching step that defines the final resolution of each drift vector is 34 × 34 pixels (2.7 × 2.7 km). To assess the potential performance after finding suitable search restrictions, calculated drift results from 246 Sentinel-1 image pairs have been compared to buoy GPS data, collected in 2015 between 15 January and 22 April and covering an area from 80.5 to 83.5° N and 12 to 27° E. We found a logarithmic normal distribution of the displacement difference with a median at 352.9 m using HV polarisation and 535.7 m using HH polarisation. All software requirements necessary for applying the presented sea ice drift algorithm are open-source to ensure free implementation and easy distribution.

1 Introduction

Sea ice drift has a strong impact on sea ice distribution on different temporal and spatial scales. The motion of sea ice due to wind and ocean currents causes convergence and divergence zones, resulting in the formation of ridges and opening/closing of leads. On large scales, ice export from the Arctic and Antarctic into lower latitudes, where the ice eventually melts away, contributes to a strong seasonality of total sea ice coverage (IPCC, 2013). Due to a lack of ground stations in sea-ice-covered areas, satellite remote sensing represents the most important tool for observing sea ice conditions on medium to large scales. Despite the strong impact of sea ice drift and the opportunities given by the latest satellite remote sensing techniques, there is a lack of extensive ice drift data sets providing sufficient resolution for estimating sea ice deformation on a spatial scaling of less than 5 km.

Our main regions of interest are the ice-covered seas around Svalbard and the east of Greenland. Characteristic of this area are a large variation of different ice types (marginal ice zone, first-year ice, multiyear ice, etc.), a strong seasonality of ice cover and a wide range of drift velocities. Focus was put on the winter/spring period, since the area of interest experiences the highest ice cover during this time of the year.

Early work from Nansen (1902) established the rule-of-thumb that sea ice velocity resembles 2 % of the surface wind speed with a drift direction of about 45° to the right (Northern Hemisphere) of the wind. This wind-driven explanation can give a rough estimate for instantaneous ice velocities. However, the respective influences of wind and ocean current strongly depend on the temporal and spatial scale. Only about 50 % of the long-term (several months) averaged ice drift in the Arctic can be explained by geostrophic winds, whereas the rest is related to mean ocean circulation. This proportion

increases to more than 70 % explained by wind, when considering shorter timescales (days to weeks). The wind fails to explain large-scale ice divergence patterns and its influence decreases towards the coast (Thorndike and Colony, 1982).

Using GPS drift data from the International Arctic Buoy Program (IABP), Rampal et al. (2009a) analysed the general circulation of the Arctic sea ice velocity field and found that the fluctuations follow the same diffusive regime as turbulent flows in other geophysical fluids. The monthly mean drift using 12 h displacements was found to be in the order of 0.05 to 0.1 m s^{-1} and showed a strong seasonal cycle with a minimum in April and maximum in October. The IABP data set also revealed a positive trend in the mean Arctic sea ice speed of +17 % per decade for winter and +8.5 % for summer considering the time period 1979–2007. This is unlikely to be the consequence of increased external forcing. Instead, the thinning of the ice cover is suggested to decrease the mechanical strength which eventually causes higher speed given a constant external forcing (Rampal et al., 2009b).

Fram Strait represents the main gate for Arctic ice export and high drift velocities are generally found in this area with direction southward. Based on moored doppler current meters mounted near 79° N 5° W, Widell et al. (2003) found an average southward velocity of 0.16 m s^{-1} for the period 1996–2000. Daily averaged values were usually in the range 0–0.5 m s^{-1} and on very few occasions above 0.5 m s^{-1}.

GPS buoys and current meters are important tools for measuring ice drift at specific locations. However, to monitor sea ice drift on medium to large scales, satellite remote sensing represents the most important data source today. The polar night and a high probability for cloud cover over sea ice limit the capability of optical sensors for reliable year-round sea ice monitoring. Unlike optical sensors, Spaceborne Synthetic Aperture Radar (SAR) are active sensors, operate in the microwave spectrum and can produce high-resolution images regardless of solar illumination and cloud cover. Since the early 1990s SAR sensors have been delivering systematic acquisitions of sea-ice-covered oceans and Kwok et al. (1990) showed that sea ice displacement can be calculated from consecutive SAR scenes.

The geophysical processor system from Kwok et al. (1990) has been used to calculate sea ice drift fields in particular over the western Arctic (depending on SAR coverage) once per week with a spatial resolution of 10–25 km for the time period 1996–2012. This extensive data set makes use of SAR data from RADARSAT-1 operated by the Canadian Space Agency, and from ENVISAT (Environmental Satellite) ASAR (Advanced Synthetic Aperture Radar) operated by ESA (European Space Agency).

To resolve drift details on a finer scale, a high-resolution sea ice drift algorithm for SAR images from ERS-1 (European Remote-sensing Satellite from ESA) based on pattern matching was introduced by Thomas et al. (2008), which allowed drift calculation with up to 400 m resolution. Hollands and Dierking (2011) implemented their own modified version of this algorithm to derive sea ice drift from ENVISAT ASAR data.

To also provide drift estimates in areas where areal matching procedures (like cross and phase correlation) fail, Berg and Eriksson (2014) introduced a hybrid algorithm for sea ice drift retrieval from ENVISAT ASAR data using phase correlation and a feature based matching procedure that is activated if the phase correlation value is below a certain threshold.

The current generation of SAR satellites including RADARSAT-2 and Sentinel-1 are able to provide images with more than one polarisation. Komarov and Barber (2014) and Muckenhuber et al. (2016) have evaluated the sea ice drift retrieval performance with respect to the polarisation using a combination of phase/cross-correlation and feature tracking based on corner detection respectively. Muckenhuber et al. (2016) has shown that feature tracking provides on average around four times as many vectors using HV polarisation compared to HH polarisation.

After the successful start of the Sentinel-1 mission in early 2014, high-resolution SAR images are delivered for the first time in history within a few hours after acquisition as open-source data to all users. This introduced a new era in SAR Earth observation with great benefits for both scientists and other stakeholders. Easy, free and fast access to satellite imagery facilitate the possibility to provide products on an operational basis. The Danish Technical University (Pedersen et al., 2015, http://www.seaice.dk/) provides an operational sea ice drift product based on Sentinel-1 data with 10 km resolution as part of the Copernicus Marine Environment Monitoring Service (CMEMS, http://marine.copernicus.eu).

The sea-ice-covered oceans in the European Arctic sector represent an important area of interest for the Sentinel-1 mission and due to the short revisit time in the Arctic, our area of interest is monitored by Sentinel-1 on a daily basis (ESA, 2012).

This paper follows up the work from Muckenhuber et al. (2016), who published an open-source feature-tracking algorithm to derive computationally efficient sea ice drift from Sentinel-1 data based on the open-source ORB algorithm from Rublee et al. (2011), which is included in the OpenCV Python package. We aim to improve the feature-tracking approach by combining it with pattern matching. Unlike Berg and Eriksson (2014), the feature-tracking step is performed initially and serves as a first guess to limit the search area of the pattern-matching step.

From a methodological point of view, algorithms for deriving displacement vectors between two consecutive SAR images are based either on feature tracking or pattern matching.

Feature tracking detects distinct patterns (features) in both images and tries to connect similar features in a second step without the need for knowing the locations. This can be done

in a computationally efficient manner and the resulting vectors are often independent of their neighbours in terms of position, length, direction and rotation, which can potentially be an important advantage for resolving shear zones, rotation and divergence/convergence zones. The considered feature-tracking approach identifies features without taking the position of other features into account and matches features from one image to the other without taking the drift and rotation information from the surrounding vectors into account (Muckenhuber et al., 2016). However, due to the independent positioning of the features, very close features may share some pixels and since all vectors from the resolution pyramid are combined, the feature size varies among the matches, which implies a varying resolution. In addition, the resulting vector field is not evenly distributed in space and large gaps may occur between densely covered areas, which can eventually lead to missing a shear or divergence/convergence zone.

Pattern matching, on the other hand, takes a small template from the first image at the starting location of the vector and tries to find a match on a larger template from the second image. Simple pattern-matching methods based on normalised cross-correlation often demand considerable computational effort. Nevertheless, this approach is widely used, since it allows the vector positions to be defined. For practical reasons, a pyramid approach is generally used to derive high-resolution ice drift. This speeds up the processing, but potentially limits the independence of neighbouring vectors, since they depend on a lower-resolution estimate (Thomas et al., 2008).

The objective of this paper is to combine the two approaches in order to benefit from the respective advantages. The main advantages of the considered feature-tracking approach are the computational efficiency and the independence of the vectors in terms of position, length, direction and rotation. The considered pattern-matching method, on the other hand, allows better control over vector positioning and resolution, which is a necessity for computing divergence, shear and total deformation.

The presented algorithm, all necessary software requirements (python including Nansat, openCV and SciPy) and the satellite data from Sentinel-1 are open-source. A free and user-friendly implementation shall support an easy distribution of the algorithm among scientists and other stakeholders.

The paper is organised as follows: the used satellite products and buoy data are introduced in Sect. 2. The algorithm description including data preprocessing is given in Sect. 3, together with tuning and performance assessment methods. Section 4 presents the preprocessing, parameter tuning and performance assessment results and provides a recommended parameter setting for the area and time period of interest. The discussion including outlook can be found in Sect. 5.

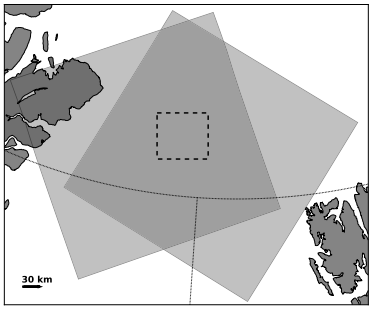

Figure 1. Coverage of image pair Fram Strait that is used as representative image pair to explain the algorithm approach. The dashed rectangle depicts the area shown in Fig. 4 and illustrates the vector distribution of the algorithm steps.

2 Data

The Sentinel-1 mission is a joint initiative of the European Commission and the European Space Agency (ESA) and represents the European Radar Observatory for the Copernicus programme, a European system for monitoring the Earth with respect to environmental and security issues. The mission includes two identical satellites, Sentinel-1A (launched in April 2014) and Sentinel-1B (launched in April 2016), each carrying a single C-band SAR with a centre frequency of 5.405 GHz and dual-polarisation support (HH + HV, VV + VH) also for the wide swath mode. Both satellites fly in the same near-polar, sun-synchronous orbit and the revisit time is less than 1 day in the Arctic (ESA, 2012). The main acquisition mode of Sentinel-1 over sea-ice-covered areas is Extra Wide mode Ground Range Detected Medium Resolution (EW GRDM) and the presented algorithm is built for processing this data type. The covered area per image is 400 km × 400 km and the data are provided with a pixel spacing of 40 m × 40 m in both HV and HH polarisation. The introduced algorithm can utilise both the HV and HH channel. However, the focus of this paper is put on using HV polarisation (mainly acquired over the European Arctic and the Baltic sea), since this channel provides on average four times more feature tracking vectors in our area of interest than HH (Muckenhuber et al., 2016), representing a better initial drift estimate for the combined algorithm.

To illustrate the algorithm performance and explain the individual steps, we use an image pair acquired over Fram Strait. The acquisition times of the two consecutive images are 28 March 2015 07:44:33 UTC and 29 March 2015 16:34:52 UTC, and the covered area is shown in Fig. 1. This image pair covers a wide range of different ice conditions (multiyear ice, first-year ice, marginal ice zone etc.) and the ice conditions are representative of our area and time period of interest.

To evaluate suitable search limitations and assess the potential algorithm performance, we use GPS data from drift buoys that have been set out in the ice-covered waters north of Svalbard as part of the Norwegian Young Sea Ice Cruise (N-ICE2015) project of the Norwegian Polar Institute (Spreen and Itkin, 2015). The ice conditions during the N-ICE2015 expedition are described on the project website (http://www.npolar.no/en/projects/n-ice2015.html) as challenging. The observed ice pack, mainly consisting of 1.3–1.5 m thick multiyear and first-year ice, drifted faster than expected and was very dynamic. Closer to the ice edge, a break up of ice floes has been observed due to rapid ice drift and the research camp had to be evacuated and re-established four times. This represents a good study field, since these challenging conditions are expected in our area and time period of interest. The considered GPS data have been collected in 2015 between 15 January and 22 April, and cover an area ranging from 80.5 to 83.5° N and 12 to 27° E. The buoys recorded their positions either hourly or every 3 h. In the latter case, the positions have been interpolated for each hour.

3 Method

3.1 Data preprocessing

To process Sentinel-1 images within Python (extraction of backscatter values and corresponding geolocations, reprojection, resolution reduction etc.), we use the Python toolbox Nansat (Korosov et al., 2016), which builds on the Geospatial Data Abstraction Library (http://www.gdal.org). As in Muckenhuber et al. (2016), we change the projection of the provided ground control points (latitude/longitude values given for certain pixel/line coordinates) to stereographic and use spline interpolation to calculate geographic coordinates. This also provides a good geolocation accuracy at high latitudes. The pixel spacing of the image is changed by averaging from 40 to 80 m, which is closer to the sensor resolution of 93 m range × 87 m azimuth, and decreases the computational effort.

For each pixel p, the Sentinel-1 data file provides a digital number $\mathrm{DN_p}$ and a normalisation coefficient A_p, from which the normalised radar cross section σ^0_raw is derived by the following equation:

$$\sigma^0_\mathrm{raw} = \mathrm{DN}^2_\mathrm{p}/A^2_\mathrm{p}. \quad (1)$$

The normalised radar cross section σ^0_raw reveals a logarithmic distribution and the structures in the sea ice are mainly represented in the low and medium backscatter values rather than in the highlights. Therefore, we change the linear scaling of the raw backscatter values σ^0_raw to a logarithmic scaling and get the backscatter values $\sigma^0 = 10 \cdot \lg(\sigma^0_\mathrm{raw})$ [dB]. A representative backscatter distribution over sea ice is shown in Fig. 2. Using a logarithmic scaling provides a keypoint distribution for the feature tracking algorithm that depends less on high peak values, while the total number of vectors increases.

To apply the feature-tracking algorithm from Muckenhuber et al. (2016), the SAR backscatter values σ^0 have to be converted into intensity values i with $0 \leq i \leq 255$ for $i \in \mathbb{R}$. This conversion is done by using Eq. (2) and setting all values outside the domain to 0 and 255.

$$i = 255 \cdot \frac{\sigma^0 - \sigma^0_\mathrm{min}}{\sigma^0_\mathrm{max} - \sigma^0_\mathrm{min}}. \quad (2)$$

The upper brightness boundary σ^0_max is set according to the recommended values from Muckenhuber et al. (2016), i.e. −18.86 and −10.97 dB for HV and HH respectively. The lower boundary σ^0_min was chosen to be −32.5 dB (HV) and −25.0 dB (HH), since this was found to be a reasonable range of expected backscatter values. Figure 3 shows the image pair Fram Strait after the conversion into intensity values. For the sake of computational efficiency, the same intensity value scaling is used for the pattern-matching step.

3.2 Sea ice drift algorithm

The presented sea ice drift algorithm is based on a combination of feature tracking and pattern matching, and is designed to utilise the respective advantages of the two considered approaches. Computationally efficient feature tracking is used to derive a first estimate of the drift field. The provided vectors serve as the initial search position for pattern matching, which provides accurate drift vectors at each given location including rotation estimate and maximum cross-correlation value. As illustrated in the flow chart in Fig. 4, the algorithm consists of five main steps: (I) feature tracking, (II) filter, (III) first guess, (IV) pattern matching and (V) final drift product.

(I) Feature tracking

The feature-tracking algorithm used in this work is an adjusted version from Muckenhuber et al. (2016), who introduced a computationally efficient sea ice drift algorithm for Sentinel-1 based on the ORB (Oriented FAST and Rotated BRIEF) algorithm from Rublee et al. (2011). ORB uses the concept of the FAST keypoint detector (Rosten and Drummond, 2006) to find corners on several resolution levels. The patch around each corner is then described using an modified version of the binary BRIEF descriptor from Calonder et al. (2010). To ensure rotation invariance, the orientation of the patch is calculated using the intensity-weighted centroid. Muckenhuber et al. (2016) applies a brute force matcher that compares each feature from the first image to all features in the second image. The comparison of two features is done using the Hamming distance, which represents the number of positions in which the two compared binary feature vectors differ from each other. The best match is accepted if the ratio of the shortest and second shortest Hamming distances

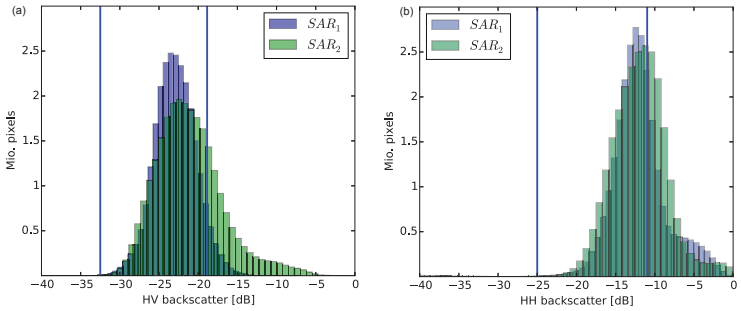

Figure 2. Histogram of **(a)** HV and **(b)** HH backscatter values σ^0 from image pair Fram Strait. The lower and upper brightness boundaries for HV ($\sigma^0_{\text{min}} = -32.5\,\text{dB}$, $\sigma^0_{\text{max}} = -18.86\,\text{dB}$) and HH ($\sigma^0_{\text{min}} = -25.0\,\text{dB}$, $\sigma^0_{\text{max}} = -10.97\,\text{dB}$) are shown with blue lines and illustrate the domain for the intensity values i.

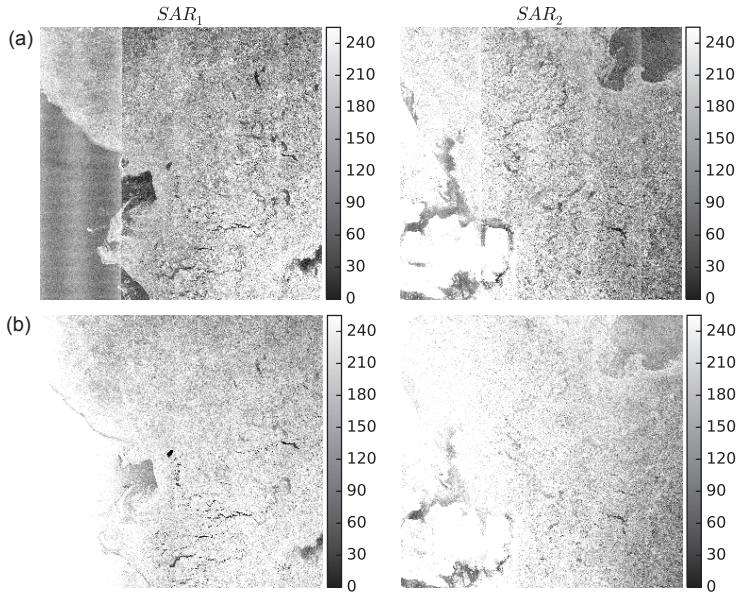

Figure 3. Image pair Fram Strait in **(a)** HV and **(b)** HH polarisation after conversion (Eq. 2) from backscatter values σ^0 into intensity values with range $0 \le i \le 255$ using lower and upper brightness boundaries for HV: $\sigma^0_{\text{min}} = -32.5\,\text{dB}$ and $\sigma^0_{\text{max}} = -18.86\,\text{dB}$ and HH: $\sigma^0_{\text{min}} = -25.0\,\text{dB}$, $\sigma^0_{\text{max}} = -10.97\,\text{dB}$.

is below a certain threshold. Given a suitable threshold (and unique features), the ratio test will discard a high number of false matches, while eliminating only a few correct matches.

Muckenhuber et al. (2016) found a suitable parameter setting for our area and time period of interest, including a Hamming distance threshold of 0.75, a maximum drift filter of $0.5\,\text{m}\,\text{s}^{-1}$, a patch size of 34×34 pixels and a resolution pyramid with seven steps combined with a scaling factor of 1.2. Due to the resolution pyramid, the considered feature area varies from 2.7×2.7 to 9.8×9.8 km and the resulting drift field represents a resolution mixture between these boundaries.

We adjust the algorithm from Muckenhuber et al. (2016) by applying a logarithmic scaling for the SAR backscatter values σ_0 instead of the previously used linear scaling (Sect. 3.1). In addition, we extract for each vector the rotation information α, i.e. how much the feature rotates from the first to the second image.

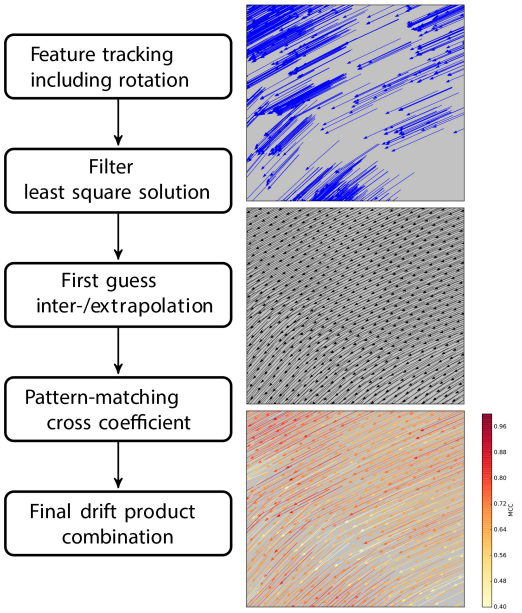

Figure 4. The flow chart on the left depicts the five main steps of the algorithm. The right column illustrates the evolution of the drift results using image pair Fram Strait in HV polarisation and a grid with 4 km spacing. (NB The part of the image pair that is depicted here is marked with a dashed rectangle in Fig. 1.) Blue vectors are derived by applying an adjusted version of the feature tracking algorithm from Muckenhuber et al. (2016). Black vectors indicate the initial drift estimate (first guess) based on filtered feature-tracking vectors. The final drift product (yellow to red vectors) are derived from combining the first guess with pattern-matching adjustment and applying a minimum cross-correlation value. A total of 4725 vectors have been found on image pair Fram Strait with a MCC value above 0.4 in 4 min.

Applying the adjusted feature-tracking algorithm provides a number of unevenly distributed vectors (e.g. blue vectors in Fig. 4) with start positions $x_{1\mathrm{f}}$, $y_{1\mathrm{f}}$ on the first image (SAR_1), end positions $x_{2\mathrm{f}}$, $y_{2\mathrm{f}}$ on the subsequent image (SAR_2) and corresponding rotation values $\alpha_{\mathrm{raw\,f}}$. The index f represents a feature-tracking vector and ranges from 1 to F, with F being the total number of derived feature-tracking vectors. For the sake of computational efficiency, the vectors from all resolution pyramid levels are treated equally.

To avoid zero-crossing issues during the following filter and inter-/extrapolation process (in case the image rotation δ between SAR_1 and SAR_2 is close to 0°), a factor $|180-\delta|$ is added to the raw rotation values $\alpha_{\mathrm{raw\,f}}$ using the following equation:

$$\alpha_{\mathrm{f}} = \begin{cases} \alpha_{\mathrm{raw\,f}} + |180-\delta| & \text{if } \alpha_{\mathrm{raw\,f}} + |180-\delta| < 360 \\ \alpha_{\mathrm{raw\,f}} + |180-\delta| - 360 & \text{if } \alpha_{\mathrm{raw\,f}} + |180-\delta| > 360 \end{cases}. \quad (3)$$

This centres the reasonable rotation values in the proximity of 180°. After applying the filter and inter-/extrapolation process, the estimated rotation α is corrected by subtracting $|180-\delta|$.

(II) Filter

To reduce the impact of potentially erroneous feature-tracking vectors on the following steps, outliers are filtered according to drift and rotation estimates derived from least-squares solutions using a third-degree polynomial function. Considering a matrix $\mathbf{A}$ that contains all end positions $x_{2\mathrm{f}}$, $y_{2\mathrm{f}}$ in the following form

$$\mathbf{A} = \begin{pmatrix} 1 & x_{21} & y_{21} & x_{21}^2 & y_{21}^2 & x_{21}\cdot y_{21} & x_{21}^3 & y_{21}^3 \\ 1 & x_{22} & y_{22} & x_{22}^2 & y_{22}^2 & x_{22}\cdot y_{22} & x_{22}^3 & y_{22}^3 \\ \vdots & \vdots & \vdots & \vdots & \vdots & \vdots & \vdots & \vdots \\ 1 & x_{2F} & y_{2\mathrm{F}} & x_{2\mathrm{F}}^2 & y_{2\mathrm{F}}^2 & x_{2\mathrm{F}}\cdot y_{2\mathrm{F}} & x_{2\mathrm{F}}^3 & y_{2\mathrm{F}}^3 \end{pmatrix}, \quad (4)$$

we derive three vectors $\boldsymbol{b}_{x_1}$, $\boldsymbol{b}_{y_1}$ and $\boldsymbol{b}_{\alpha}$ that represent the least-squares solutions for $\mathbf{A}$ and $\boldsymbol{x}_1 = (x_{11}, \ldots, x_{1\mathrm{F}})$, $\boldsymbol{y}_1 = (y_{11}, \ldots, y_{1\mathrm{F}})$ and $\boldsymbol{\alpha} = (\alpha_1, \ldots, \alpha_{\mathrm{F}})$ respectively. The starting position $x_{1\mathrm{f}}$, $y_{1\mathrm{f}}$ and the rotation α_{f} of each vector can then be simulated using a third-degree polynomial function $f(x_{2\mathrm{f}}, y_{2\mathrm{f}}, \boldsymbol{b})$ depending on the end position $x_{2\mathrm{f}}$, $y_{2\mathrm{f}}$ and the corresponding least-squares solution $\boldsymbol{b} = (b_0, b_1, b_2, b_3, b_4, b_5, b_6, b_7)$.

$$f(x_{2\mathrm{f}}, y_{2\mathrm{f}}, \boldsymbol{b}) = b_0 + b_1 x_{2\mathrm{f}} + b_2 y_{2\mathrm{f}} + b_3 x_{2\mathrm{f}}^2 + b_4 y_{2\mathrm{f}}^2 + b_5 x_{2\mathrm{f}} y_{2\mathrm{f}} + b_6 x_{2\mathrm{f}}^3 + b_7 y_{2\mathrm{f}}^3 \quad (5)$$

If the simulated start position, derived from $f(x_{2\mathrm{f}}, y_{2\mathrm{f}}, \boldsymbol{b})$, deviates from the feature-tracking start position $x_{1\mathrm{f}}$, $y_{1\mathrm{f}}$ by more than 100 pixels, the vector is deleted. The same accounts for rotation outliers. If the simulated rotation deviates from the feature-tracking rotation α_{f} by more than 60°, the vector is deleted. We found a third-degree polynomial function to be a good compromise between allowing for small- to medium-scale displacement and rotation discontinuities, and excluding very unlikely vectors that eventually would disturb the following steps. The parameters for the filter process, i.e. 100 pixels (displacement) and 60° (rotation), have been chosen according to visual interpretation using several representative image pairs. Figure 5 illustrates the filter process by depicting the results from image pair Fram Strait.

(III) First guess

The remaining feature-tracking vectors are used to estimate the drift including rotation on the entire first image, i.e. estimated x_2, y_2 and α values are provided for each pixel on SAR_1 (Fig. 6). The quality of this "first guess", however, depends on the density of the feature-tracking vector field and the local ice conditions.

Between the feature-tracking vectors, estimated values are constructed by triangulating the input data and performing linear barycentric interpolation on each triangle. That

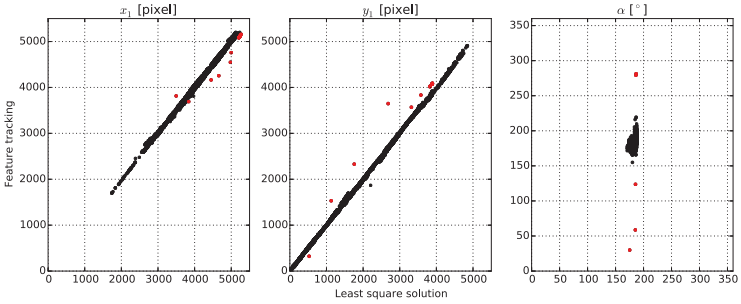

Figure 5. Filter process applied to image pair Fram Strait in HV polarisation. The x axis represents the simulated start position and rotation, derived from $f(x_{2f}, y_{2f}, \boldsymbol{b})$ and the y axis represents the feature-tracking start position x_{1f}, y_{1f} and rotation α_f. NB The image rotation is $\delta = 129.08°$, which means the rotation was adjusted by 50.92° (Eq. 3). Red points were identified as outliers and deleted.

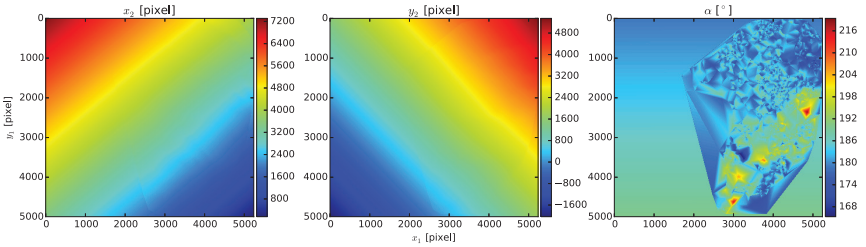

Figure 6. Example of estimated drift and rotation (first guess) based on filtered feature-tracking vectors using image pair Fram Strait in HV polarisation. The three panels show the components x_2, y_2 of the estimated end positions and the estimated rotation α for each pixel on the coordinate system x_1, y_1 of the first image (SAR_1).

means the estimated values represent the weighted mean of the three neighbouring feature-tracking values. The interpolated value v_p at any pixel p inside the triangle is given by Eq. (6), where v_1, v_2, v_3 represent the feature-tracking values at the corners of the triangle and A_1, A_2, A_3 are the areas of the triangle constructed by p and the two opposite corners; e.g. A_1 is the area between p, and the corners with values v_2 and v_3.

$$v_p = \frac{A_1 v_1 + A_2 v_2 + A_3 v_3}{A_1 + A_2 + A_3} \tag{6}$$

To provide a first guess for the surrounding area, values are estimated based on the least-squares solutions using a linear combination of x_1 and y_1. Considering a matrix $\mathbf{C}$ that contains all start positions x_{1f}, y_{1f} in the following form

$$\mathbf{C} = \begin{pmatrix} 1 & x_{11} & y_{11} \\ 1 & x_{12} & y_{12} \\ \vdots & \vdots & \\ 1 & x_{1F} & y_{1F} \end{pmatrix}. \tag{7}$$

We derive three vectors $\boldsymbol{d}_{x_2}$, $\boldsymbol{d}_{y_2}$ and $\boldsymbol{d}_{\alpha}$ that represent the least-squares solutions for $\mathbf{C}$ and $\boldsymbol{x}_2 = (x_{21}, \ldots, x_{2F})$, $\boldsymbol{y}_2 = (y_{21}, \ldots, y_{2F})$ and $\boldsymbol{\alpha} = (\alpha_1, \ldots, \alpha_F)$ respectively. The estimated end position x_2, y_2 and rotation α at any location can then be simulated using the linear function $f(x_1, y_1, \boldsymbol{c})$ depending on the start position x_1, y_1 and the corresponding least-squares solution $\boldsymbol{d} = (d_0, d_1, d_2)$.

$$f(x_1, y_1, \boldsymbol{d}) = d_0 + d_1 x_1 + d_2 y_1 \tag{8}$$

As mentioned above, the rotation estimates α are now corrected for the adjustment applied in Eq. (3), by subtracting $|180 - \delta|$.

An example for the resulting first guess, i.e. estimated values for x_2, y_2 and α on SAR_1, is shown in Fig. 6 (this figure illustrates the matrices that the algorithm considers as first guess) and corresponding vectors are shown in black in Fig. 4. Note that rotation α has already been corrected by subtracting $|180 - \delta|$. It now includes both the relative image rotation δ from SAR_1 to SAR_2 and the actual rotation of the feature itself. The introduced algorithm also provides the image rotation δ by projecting the left corners of SAR_2 onto SAR_1 and calculating the angle between the left edges of SAR_1 and SAR_2. The actual rotation of the features can easily be obtained by subtracting δ from α.

(IV) Pattern matching

The estimated drift field derived from feature tracking provides values for x_2, y_2 and α at any location on SAR_1. The representativeness of this estimate however, depends on the distance d to the closest feature-tracking vector. Therefore, small- to medium-scale adjustments of the estimates are necessary, depending on the distance d (NB The representativeness also depends on the variability of the surrounding vectors, but for the sake of computational efficiency, we only consider the distance d as representativeness measure). We apply pattern matching at the chosen points of interest to adjust the drift and rotation estimate at these specific locations.

The used pattern-matching approach is based on the maximisation of the normalised cross-correlation coefficient. Considering a small template t_1 around the point of interest from SAR_1 with size $t_{1s} \times t_{1s}$ and a larger template t_2 around the location x_2, y_2 (defined by the corresponding first guess) from SAR_2 with size $t_{2s} \times t_{2s}$, the normalised cross-correlation matrix **NCC** is defined as (Hollands, 2012):

$$\mathbf{NCC}(x,y) = \frac{\sum_{x',y'} \left(t_1'(x',y') t_2'(x+x', y+y')\right)}{\sqrt{\sum_{x',y'} \left(t_1'(x',y')^2 \sum_{x',y'} t_2'(x+x', y+y')\right)^2}} \quad (9)$$

$$t_1'(x',y') = t_1(x',y') - \frac{1}{t_{1s}^2} \sum_{x'',y''} t_1(x'',y'') \quad (10)$$

$$t_2'(x+x', y+y') = t_2(x+x', y+y') - \frac{1}{t_{1s}^2} \sum_{x'',y''} t_2(x+x'', y+y'') \quad (11)$$

with $t_1(x',\ y')$ and $t_2(x',\ y')$ representing the value of t_1 and t_2 at location x', y'. The summations are calculated over the size of the smaller template, i.e. x', y', x'' and y'' go from 1 to t_{1s}. Template t_1 is moved with step size 1 pixel over template t_2 both in the horizontal (x) and vertical (y) direction and the cross-correlation values for each step are stored in the matrix **NCC** with size $(1 + t_{2s} - t_{1s}) \times (1 + t_{2s} - t_{1s})$. The highest value in the matrix **NCC**, i.e. the maximum normalised cross-correlation value MCC, represents the location of the best match and the corresponding location adjustment is given by dx and dy.

$$\left(\frac{1+t_{2s}-t_{1s}}{2} + dx, \frac{1+t_{2s}-t_{1s}}{2} + dy\right) = \underset{x,\,y}{\operatorname{argmax}} \left(\mathbf{NCC}(x,y)\right) \quad (12)$$

To restrict the search area t_{2s} to a circle, we set all values of **NCC** that are further than $t_{2s}/2$ away from the centre position to zero. This limits the distance from the first guess to a constant value, rather than to an arbitrary value depending on the looking angle of the satellite. To account for rotation adjustment, the matrix **NCC** is calculated several times: template t_1 is rotated around the initially estimated rotation α from $\alpha - \beta$ to $\alpha + \beta$ with step size $\Delta\beta$. The angle β is the maximum additional rotation and therefore represents the rotation restriction. The **NCC** matrix with the highest cross-correlation value MCC is returned.

To illustrate the pattern-matching process, an example taken from image pair Fram Strait is shown in Fig. 7.

The described process demands the specification of four parameters: t_{1s}, t_{2s}, β and $\Delta\beta$.

The size of the small template $t_{1s} \times t_{1s}$ defines the considered area that is tracked from one image to the next and hence affects the resolution of the resulting drift product. Sea ice drift might be different on different resolution scales. This is particularly an issue in the case of rotation. The feature-tracking vectors provide the first guess and this vector field should represent the same drift resolution as considered by the pattern-matching step. In order to be consistent with the resolution of the feature-tracking step and achieve our goal of a sea ice drift product with a spatial scaling of less than 5 km, we use the size of the feature-tracking patch of the pyramid level with the highest resolution to define the size of t_1. That means we use $t_{1s} = 34$ pixels (2.7 km).

The size of the larger template $t_{2s} \times t_{2s}$ restricts the search area on SAR_2, i.e. to what extent the first guess can be adjusted geographically, and the angle β restricts the rotation adjustment of the first guess α. The three parameters t_{2s}, β and $\Delta\beta$ have a strong influence on the computational efficiency of the drift algorithm, meaning that an increase of t_{2s}, β and a decrease of $\Delta\beta$ increase the computational effort of the pattern-matching step. Based on the visual interpretation of several representative image pairs, we found $\Delta\beta = 3°$ to be a good compromise between the matching performance and computational efficiency.

Since the representativeness of the first guess decreases with distance d to the closest feature-tracking vector (an example to illustrate the distribution of d is shown Fig. 8), the search restrictions t_{2s} and β should increase with d. Based on the performed search restriction evaluation (Sect. 4), we found the following functions to represent useful restrictions for our area and time period of interest.

$$t_{2s}(d) = t_{1s} + 2d \quad d_{\min} \le d \le d_{\max} \quad d \in \mathbb{N} \quad (13)$$

$$\beta(d) = \begin{cases} 9 & \text{if } d < d_{\max} \\ 12 & \text{if } d \ge d_{\max} \end{cases} \quad (14)$$

The values for $d_{\min}$, $d_{\max}$, β and $\Delta\beta$ can easily be varied in the algorithm to adjust, for example, for different areas, drift conditions or a different compromise between matching performance and computational efficiency.

(V) Final drift product

In the last step, the small- to medium-scale displacement adjustments from pattern matching are added to the estimated

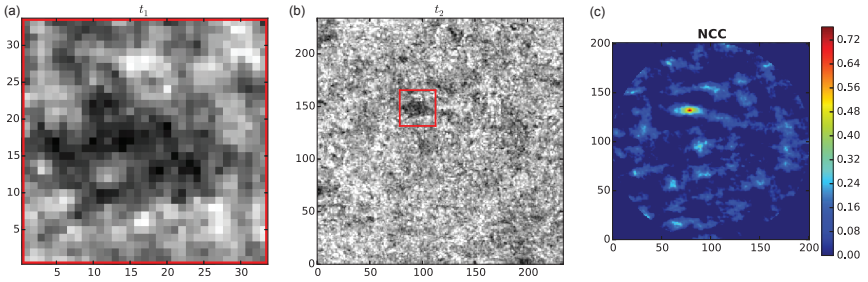

Figure 7. Pattern matching using initial drift estimate from feature tracking: The small template t_1 **(a)** around the point of interest on SAR_1 is rotated from $\alpha - \beta$ to $\alpha + \beta$ and matched with the large template t_2 **(b)** from SAR_2, which has its centre at the estimated end position x_2, y_2. The right contour plot shows the normalised cross-correlation matrix **NCC** of the rotation β^* that provided the highest maximum cross-correlation coefficient MCC. The estimated end position x_2, y_2 of this example has to be adjusted by $dx = -21$ pixels, $dy = 32$ pixels to fit with the location of MCC = 0.71. Rotation adjustment β^* was found got be 3°. NB x and y axes represent pixel coordinates.

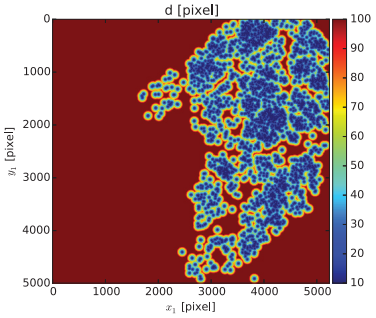

Figure 8. Example to illustrate the distribution of distance d to the closest feature-tracking vector using image pair Fram Strait in HV polarisation. Values outside the range $d_{min} \leq d \leq d_{max}$ are set to $d_{min} = 10$ and $d_{max} = 100$. The points with value d_{min} represent the start positions x_{1f}, y_{1f} of the feature-tracking vectors on the coordinate system x_1, y_1 of SAR_1. The figure depicts the matrix that the algorithm considers for the distribution of d.

first guess derived from feature tracking. Using buoy comparison, we found that the probability for large displacement errors decreases with increasing MCC value (Sect. 4). Therefore, vectors that have a MCC value below the threshold MCC_{min} are removed. We found $MCC_{min} = 0.4$ to be a good filter value, but this value can easily be adjusted in the algorithm depending on the sought compromise between number of vectors and error probability. The algorithm returns the final drift vectors in longitude, latitude, the corresponding first guess rotation α and the rotation adjustment β in degrees and the maximum cross-correlation value MCC. An example for the final product is depicted with yellow-to-red-coloured vectors in Fig. 4. The colour scale refers to the MCC value, indicating the probability of an erroneous vector.

3.3 Comparison with buoy data

Sentinel-1 image pairs have been selected automatically according to the position and timing of the GPS buoy data from the N-ICE2015 expedition. Each pair yielded more than 300 drift vectors when applying the feature-tracking algorithm from Section 3.2 and had a time difference between the two acquisitions of less than 3 days. Drift vectors have been calculated with the presented algorithm starting at the buoy GPS position with the least time difference to the acquisition of the first satellite image. The distance D between the calculated end position on the second image and the buoy GPS position with the least time difference to the second satellite acquisition has been calculated using the following equation:

$$D = \sqrt{(u - U)^2 + (v - V)^2}, \quad (15)$$

where u and v represent eastward and northward drift components of the displacement vector derived by the algorithm, and U and V are the corresponding drift components of the buoy.

4 Results

4.1 Search restriction evaluation

To find suitable values for restricting the size of the search window t_{2s} and the rotation range defined by β, we calculated drift vectors, which can be compared to the considered GPS buoy data set, using restrictions that are computationally more demanding than we anticipate for the recommended setting, i.e. $t_{2s} = 434$ pixels and $\beta = 18°$. These values correspond to a possible pattern-matching adjustment of up to 200 pixels (16 km) and 18° in any direction independent of the distance d to the closest feature-tracking vector.

Based on an automatic search, we found 244 matching Sentinel-1 image pairs (consisting of 111 images) that al-

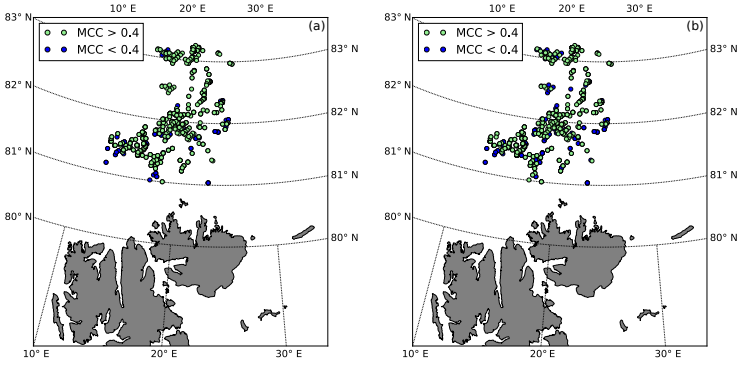

Figure 9. Considered buoy locations from the N-ICE2015 expedition that were used for comparison with algorithm results. Green and blue colours indicate start locations (on SAR_1) to which the algorithm provided vectors with a MCC value above and below 0.4 using **(a)** HV and **(b)** HH polarisation.

lowed for comparison with 711 buoy vectors (buoy locations are shown in Fig. 9). The distance D (Eq. 15) between the buoy location at the time of the second image SAR_2 and the corresponding algorithm result represents the error estimate for one vector pair. To identify algorithm results that are more likely erroneous, vector pairs with a value D above 1000 m are marked with red dots in Figs. 10 and 11. Vector pairs with $D < 1000$ m are plotted with black dots.

Figures 10 and 11 show the resulting pattern-matching adjustment of location (dx, dy) and rotation ($d\beta$) using the computationally demanding restrictions. The values are plotted against distance d to the next feature tracking vector in order to identify the dependence of the parameters on d. The blue lines in Figs. 10 and 11 indicate the recommended restrictions. This represents a compromise between computational efficiency and allowing the algorithm to adjust the first guess as much as needed for our time period and area of interest. The corresponding functions for $t_{2s}(d)$ and $\beta(d)$ are given in Eqs. (13) and (14) and the recommended boundary values for distance d are $d_{min} = 10$ and $d_{max} = 100$.

4.2 Performance assessment

Using the recommended search restrictions from above, the algorithm has been compared to the N-ICE2015 GPS buoy data set (Fig. 9) to assess the potential performance after finding suitable search restrictions for the area and time period of interest. The automatic search provided 246 image pairs (consisting of 111 images) and 746 vectors for comparison for the considered time period (15 January to 22 April) and area (80.5 to 83.5° N and 12 to 27° E). NB This is a higher number of vectors than found for the evaluation of the search restrictions, since the used search windows t_2 are smaller and vectors closer to the SAR edge may be included.

The results of the conducted performance assessment are shown in Fig. 12. We found that the probability for a large D value (representative for the error) decreases with increasing maximum cross-correlation value MCC. Therefore we suggest excluding matches with a MCC value below a certain threshold MCC_{min}. This option is embedded into the algorithm, but can easily be adjusted or turned off by setting $MCC_{min} = 0$. Based on the findings shown in Fig. 12, we recommend a cross-correlation coefficient threshold $MCC_{min} = 0.4$ for our time period and area of interest. Using the suggested threshold reduces the number of vector pairs from 746 to 588 for the HV channel and to 478 for the HH channel.

The conducted performance assessment also reveals a logarithmic normal distribution of the distance D (Eq. 15) that can be expressed by the following probability density function (solid red line in Fig. 12):

$$\ln N(D;\mu,\sigma) = \frac{1}{\sigma D\sqrt{2\pi}} e^{-\frac{(\ln D-\mu)^2}{2\sigma^2}}, \quad (16)$$

with μ and σ being the mean and standard deviation of the variable's natural logarithm. We found the mean and variance of the distribution $\ln N$ to be $\mu = 5.866$ and $\sigma^2 = 1.602$ for HV polarisation and $\mu = 6.284$ and $\sigma^2 = 2.731$ for HH polarisation (solid red lines in Fig. 12). The medians of the logarithmic normal distribution are $e^{\mu} = 352.9$ m for HV polarisation and $e^{\mu} = 535.7$ m for HH polarisation (dashed red lines in Fig. 12).

4.3 Recommended parameter setting

Based on the restriction evaluation, our experience with the algorithm behaviour, and considering a good compromise between computational efficiency and high quality of the resulting vector field, we recommend the parameter setting shown in Table 1 for our area and time period of interest. The corresponding recommended values for $t_{2s}(d)$ and $\beta(d)$ are given in Eqs. (13) and (14).

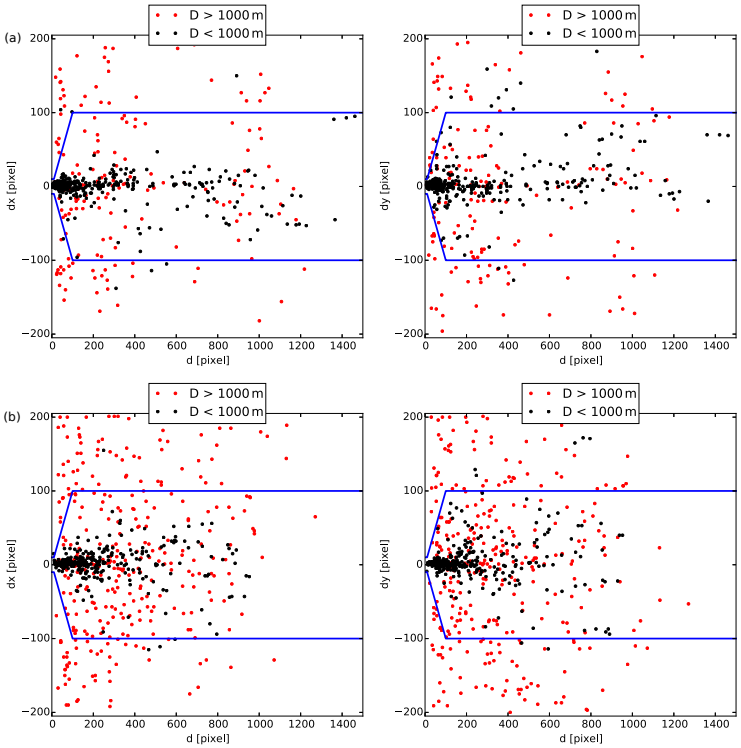

Figure 10. Pattern-matching location adjustment dx and dy in x and y direction vs. distance d to closest feature-tracking vector using **(a)** HV and **(b)** HH polarisation. D represents the difference between buoy GPS position and algorithm result. The blue lines indicate the recommended setting for t_{2s} (Eq. 13) with $d_{min} = 10$ and $d_{max} = 100$.

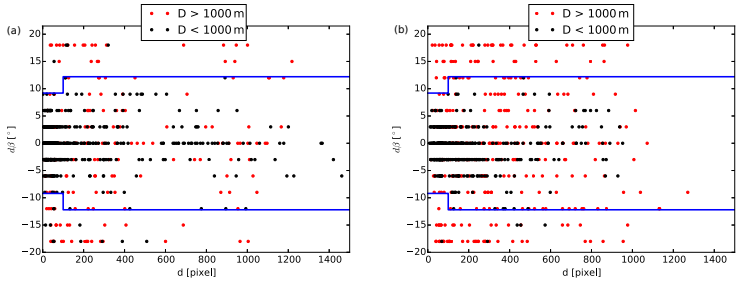

Figure 11. Pattern-matching rotation adjustment $d\beta$ vs. distance d to closest feature-tracking vector using **(a)** HV and **(b)** HH polarisation. D represents the difference between buoy GPS position and algorithm result. The blue lines indicate the recommended setting for β (Eq. 14) with $d_{min} = 10$ and $d_{max} = 100$.

4.4 Computational efficiency

The processing time depends on the parameter setting and the chosen vector distribution. Using the recommended parameter setting from Table 1 allows for high-resolution sea ice drift retrieval from a Sentinel-1 image pair within a few minutes. Figure 4 depicts calculated ice drift vectors for the image pair Fram Strait on a grid with 4 km (50 pixels) spac-

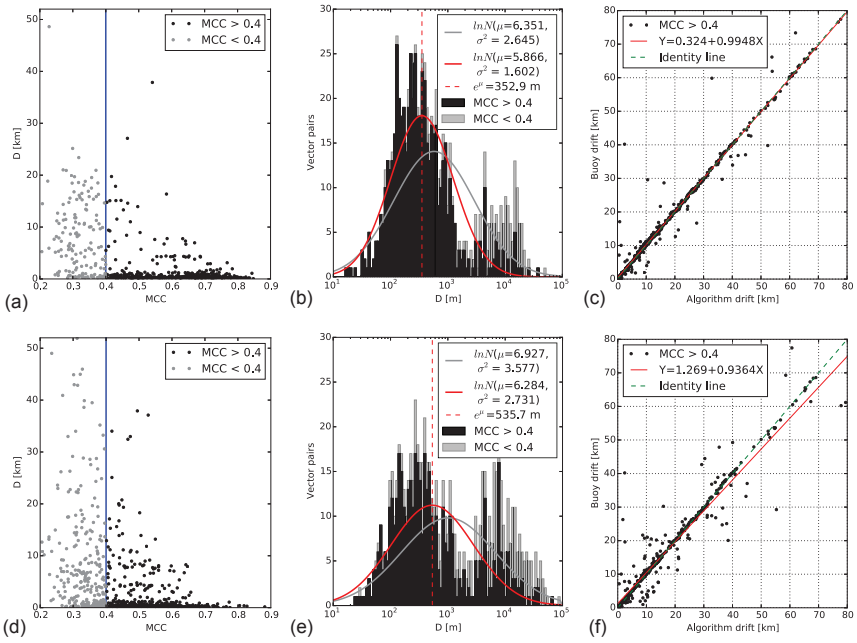

Figure 12. Calculated ice drift using recommended search restrictions compared to buoy GPS data using **(a–c)** HV and **(d–f)** HH polarisation. Light grey represents vectors with maximum cross-correlation values MCC < 0.4 and results after using the suggested threshold $MCC_{min} = 0.4$ are shown in black. **(a, d)** MCC values against distance D (Eq. 15) between algorithm and buoy end position. The blue line indicates the recommended setting for $MCC_{min} = 0.4$. **(b, e)** Logarithmic histogram of distance D with 100 bins between 10 and 10^5 m including two logarithmic normal distributions that were fitted to all results (grey) and to the filtered results with MCC > 0.4 (solid red line). **(c, f)** Comparison of drift distance derived from the algorithm against buoy displacement for the filtered results with MCC > 0.4.

Table 1. Recommended parameter setting for sea ice drift retrieval from Sentinel-1 using the presented algorithm.

Parameter	Meaning	Recommended setting
$[\sigma^0_{min}, \sigma^0_{max}]$ (HH)	Brightness boundaries for HH channel	[−25, −10.97 dB]
$[\sigma^0_{min}, \sigma^0_{max}]$ (HV)	Brightness boundaries for HV channel	[−32.5, −18.86 dB]
t_{1s}	Size of template t_1	34 pixels (2.7 km)
$[d_{min}, d_{max}]$	Boundaries for distance d	[10, 100 pixels]
MCC_{min}	Threshold for cross-correlation	0.4
$\Delta\beta$	Rotation angle increment	3°

ing. The corresponding processing times are shown in Table 2. The calculations have been done using a MacBook Pro from early 2013 with a 2.7 GHz Intel Core i7 processor and 8 GB 1600 MHz DDR3 memory. The total processing time for 4725 vectors with a normalised cross-correlation value above 0.4, is about 4 min. This can be considered a representative value for an image pair with large overlap, good coverage with feature-tracking vectors and 4 km grid spacing.

The initial process in Table 2 "Create Nansat objects from Sentinel-1 image pair and read matrixes" takes the same amount of computational effort for all image pairs consisting of Sentinel-1 images with 400 × 400 km coverage.

The process (I) feature tracking depends on the setting of the feature-tracking algorithm and varies strongly with the chosen number of features. Using the recommended setting from Muckenhuber et al. (2016), which includes the number of features to be 100 000, the presented computational effort can be considered representative for all image pairs, independent of chosen points of interest and overlap of the SAR scenes.

Table 2. Processing time for sea ice drift retrieval from image pair Fram Strait on a grid with 4 km (50 pixels) spacing using HV polarisation (Fig. 4). Representative for an image with large overlap and good coverage with feature-tracking vectors.

Process	Time [s]
Create Nansat objects from Sentinel-1 image pair and read matrixes	70
(I) Feature tracking	66
(II)–(V) Pattern matching and combination	107
$\sum$ Sea ice drift retrieval	243

The process (IV) pattern matching, however, depends on the considered image pair and the chosen drift resolution. The computational effort is proportional to the number of chosen points of interest. Given a evenly distributed grid of points of interest, the computational effort increases with overlapping area of the SAR scenes, since pattern-matching adjustments are only calculated in the overlapping area. The effort potentially decreases with a higher number of well-distributed feature-tracking vectors, since the size of the search windows t_2 (and slightly the range of the angle β) increases with distance d to the closest feature-tracking vector.

5 Discussion and outlook

To estimate the potential performance of the introduced algorithm for given image pairs, given ice conditions, given region and given time, we compared drift results from 246 Sentinel-1 image pairs with corresponding GPS positions from the N-ICE2015 buoy data set. We found a logarithmic error distribution with a median at 352.9 m for HV and 535.7 m for HH (Fig. 12). The derived error values represent a combination of the following error sources:

- Timing: buoy GPS data were collected every 1–3 h and the timing does not necessarily match the satellite acquisition time.
- Resolution: the algorithm returns the drift of a pattern (recommended size = 34 pixels; see Table 1), whereas the buoy measures the drift at a single location.
- Conditions: the ice conditions around the buoy are not known well enough to exclude the possibility that the buoy is floating in a lead. In this case, the buoy trajectory could represent a drift along the lead rather then the drift of the surrounding sea ice.
- Actual error of the algorithm.

A main advantage of the combined algorithm compared to simple feature tracking is the user-defined positioning of the drift vectors. The current algorithm set-up allows the user to choose whether the drift vectors should be positioned at certain points of interest or on a regular grid with adjustable spacing. Constricting the pattern-matching process to the area of interest minimises the computational effort according to the individual needs.

The recommended parameters shown in Table 1 are not meant as a fixed setting, but should rather act as guidelines to estimate the expected results and the corresponding computational effort. The parameters can easily be varied in the algorithm set-up and should be chosen according to availability of computational power, required resolution, area of interest and expected ice conditions (e.g. strong rotation).

The presented combination of feature tracking and pattern matching can be applied to any other application that aims to derive displacement vectors from two consecutive images in a computationally efficient way. The only restriction is that images need to depict edges that can be recognised as keypoints for the feature-tracking algorithm, and the conversion into intensity values i (Eq. 2) needs to be adjusted according to the image type.

The remote sensing group at NERSC is currently developing a new preprocessing step to remove thermal noise on HV images over the ocean and sea ice. First tests have shown a significant improvement of the sea ice drift results using this preprocessing step before applying the presented algorithm. This is ongoing work and will be included in a future version of the algorithm.

The European Space Agency is also in the process of improving their thermal noise removal for Sentinel-1 imagery. Noise removal in range direction is driven by a function that takes measured noise power into account. Until now, noise measurements are taken at the start of each data acquisition, i.e. every 10–20 min, and a linear interpolation is performed to provide noise values every 3 s. The distribution of noise measurements showed a bimodal shape and it was recently discovered that lower values are related to noise over ocean while higher values are related to noise over land. This means that Sentinel-1 is able to sense the difference of the earth surface brightness temperature similarly to a passive radiometer. When the data acquisition includes a transition from ocean to land or vice versa, the linear interpolation fails to track the noise variation. The successors of Sentinel-1A/B are planned to include more frequent noise measurements. Until then, ESA wants to use the 8–10 echoes after the burst that is recorded while the transmitted pulse is still travelling and the instrument is measuring the noise. This will provide

noise measurements every 0.9 s and allows the noise variations to be tracked in more detail. In addition, ESA is planning to introduce a change in the data format during 2017 that shall remove the noise shaping in azimuth. These efforts are expected to improve the performance of the presented algorithm significantly (N. Miranda, personal communication, January 2017).

Having a computationally efficient algorithm with adjustable vector positioning allows not only the provision of near-real-time operational drift data, but also the investigation of sea ice drift over large areas and long time periods. Our next step is to embed the algorithm into a supercomputing facility to further test the performance in different regions, time periods and ice conditions and evaluate and combine the results of different polarisation modes. The goal is to deliver large ice drift data sets and open-source operational sea ice drift products with a spatial resolution of less than 5 km.

This work is linked to the question of how to combine the different timings of the individual image pairs in a most useful way. Having more frequent satellite acquisitions, as we get with the Sentinel-1 satellite constellation, enables to derive displacements for shorter time gaps and the calculated vectors will reveal more details, e.g. rotational motion due to tides. As part of a scientific cruise with KV-Svalbard in July 2016, we deployed three GPS trackers on loose ice floes and pack-ice in Fram Strait. The trackers send their position every 5–30 min to deliver drift information with high temporal resolution. These efforts shall help us to gain a better understanding of short-term drift variability and by comparison with calculated sea ice drift, we will investigate how displacement vectors from subsequent satellite images relate to sea ice displacements with higher temporal resolution.

The focus of this paper in terms of polarisation was put on the HV channel, since this polarisation provides on average four times more feature-tracking vectors (using our feature-tracking approach) than HH and therefore delivers a finer initial drift for the first guess. We found our area of interest covered with HV images, but other areas in the Arctic and Antarctic are currently only monitored in HH polarisation. Considering the four representative feature-tracking image pairs from Muckenhuber et al. (2016), the relatively better HH polarisation performance (i.e. most vectors from HH, while at the same time fewest vectors from HV) was provided by the image pair that had the least time difference, i.e. 8 h compared to 31, 33 and 48 h. Therefore, we assume that the HV polarisation provides more corner features that are better preserved over time. And more consistent features could potentially also favour the performance of the pattern-matching step, but this is only an assumption and has not been tested yet. Another argument is that the presented feature-tracking approach identifies and matches corners, which represent linear features. The linear features on HH images are more sensitive to changes in incidence angle, orbit and ice conditions than the linear features on HV images. This could explain the better feature-tracking performance of the HV channel. However, pattern matching is less affected by changing linear features and more sensitive to areal pattern changes. This could potentially mean that the HH channel performs better than HV when it comes to pattern matching. However, at this point, these are just assumptions and will be addressed in more detail in our future work.

Utilising the advantage of dual polarisation (HH + HV) is certainly possible with the presented algorithm, but increases the computational effort. A simple approach is to combine the feature tracking vectors derived from HH and HV and produce a combined first guess. Pattern matching can be performed based on this combined first guess for both HH and HV individually and the results can be compared and eventually merged into a single drift product. Having two drift estimates for the same position, from HH and HV pattern matching respectively, would also allow us to disregard vectors that disagree significantly. However, this option would increase the computational effort by two, meaning that the presented Fram Strait example would need about 8 min processing time.

After implementing the presented algorithm into a supercomputing facility, we aim to test and compare the respective performances of HV, HH and HH + HV on large data sets to identify the respective advantages.

The current setting of the feature-tracking algorithm applies a maximum drift filter of $0.5\,\mathrm{m\,s^{-1}}$. We found this to be a reasonable value for our time period and area of interest. However, when considering extreme drift situations in Fram Strait and a short time interval between image acquisitions, this threshold should be adjusted.

As mentioned above, we deployed three GPS tracker in Fram Strait and they recorded their positions with a temporal resolution of 5–30 min between 8 July and 9 September 2016 in an area covering 75 to 80° N and 4 to 14° W. Considering the displacements with 30 min interval, we found velocities above $0.5\,\mathrm{m\,s^{-1}}$ on a few occasions, when the tidal motion adds to an exceptionally fast ice drift.

The GPS data from the hovercraft expedition FRAM2014-2015 (https://sabvabaa.nersc.no), which was collected with a temporal resolution of 10 s between 31 August 2014 and 6 July 2015, did not reveal a single 30 min interval during which the hovercraft was moved by ice drift more than $0.45\,\mathrm{m\,s^{-1}}$. The hovercraft expedition started at 280 km south from the North Pole towards the Siberian coast, crossed the Arctic Ocean towards Greenland and was picked up in the north-western part of Fram Strait.

In case the estimated drift from feature tracking reaches velocities close to $0.5\,\mathrm{m\,s^{-1}}$, the pattern-matching step might add an additional degree of freedom of up to 8 km, which could eventually lead to a higher drift result than $0.5\,\mathrm{m\,s^{-1}}$, depending on the time interval between the acquisitions. The smaller the time difference, the larger the potentially added velocity. In order to be consistent when combining the drift information from several image pairs with different timings,

one should apply a maximum drift filter on the final drift product of the presented algorithm that has the same maximum velocity as the feature-tracking filter. The corresponding function is implemented in the distributed open-source algorithm. As an alternative, one could adjust the search window according to the time span. However, this would add additional complexity to both the algorithm and the parameter evaluation and needs more research on how the search window should be adjusted depending on the time span. For the sake of computational efficiency, we suggest the simple approach of removing final drift vectors above the maximum speed.

Data availability. The presented sea ice drift retrieval method is based on open-source satellite data and software to ensure free application and easy distribution. Sentinel-1 SAR images are distributed by ESA for free within a few hours of acquisition under https://scihub.esa.int/dhus/. The algorithm is programmed in Python (source code: https://www.python.org) and makes use of the open-source libraries Nansat, openCV and SciPy. Nansat is a Python toolbox for processing 2-D satellite Earth observation data (source code: https://github.com/nansencenter/nansat). OpenCV (Open Source Computer Vision) is a computer vision and machine learning software library and can be downloaded under http://opencv.org. SciPy (source code: https://www.scipy.org) is a Python-based ecosystem of software for mathematics, science and engineering. The presented sea ice drift algorithm, which includes an application example, is distributed as open-source software as supplement to this paper.

The Supplement related to this article is available online at https://doi.org/10.5194/tc-11-1835-2017-supplement.

Competing interests. The authors declare that they have no conflict of interest.

Author contributions. S Muckenhuber designed the algorithm and the experiments, performed the data analysis and interpretation of the results and wrote the paper. S Sandven critically revised the work and gave important feedback for improvement. Stefan Muckenhuber and Stein Sandven approved the final version for publication.

Acknowledgements. This research was supported by the Norwegian Research Council project IceMotion (High resolution sea-ice motion from Synthetic Aperture Radar using pattern tracking and Doppler shift, project number 239998/F50). We thank Polona Itkin and Gunnar Spreen for providing us with the buoy GPS data that were collected as part of the N-ICE2015 project with support from the Norwegian Polar Institute's Centre for Ice, Climate and Ecosystems (ICE) and its partner institutes. The used satellite data were provided by the European Space Agency. We thank Nuno Miranda for information on ESA's denoising efforts for Sentinel-1. A special thanks to the anonymous reviewers for their comments and valuable input that improved the paper.

Edited by: Lars Kaleschke
Reviewed by: three anonymous referees

References

Berg, A. and Eriksson, L. E. B.: Investigation of a Hybrid Algorithm for Sea Ice Drift Measurements Using Synthetic Aperture Radar Images, IEEE T. Geosci. Remote, 52, 5023–5033, 2014.

Calonder, M., Lepetit, V., Strecha, C., and Fua, P.: BRIEF: Binary Robust Independent Elementary Features, CVLab, EPFL, Lausanne, Switzerland, 2010.

ESA: Sentinel-1 ESA's Radar Observatory Mission for GMES Operational Services, ESA Communications, SP-1322/1, ESA, the Netherlands, 2012.

Hollands, T.: Motion tracking of sea ice with SAR satellite data, dissertaiton, Section 2: Estimation of motion from images, University Bremen, Bremen, 2012.

Hollands, T. and Dierking, W.: Performance of a multiscale correlation algorithm for the estimation of sea-ice drift from SAR images: initial results, Ann. Glaciol., 52, 311–317, 2011.

IPCC – Intergovernmental Panel on Climate Change: Climate Change 2013: The Physical Science Basis, Fifth Assessment Report AR5, Cambridge University Press, Cambridge, UK and New York, NY, USA, 317–382, 323–335, 2013.

Komarov, A. S. and Barber, D. G.: Sea Ice Motion Tracking From Sequential Dual-Polarization RADARSAT-2 Images, IEEE T. Geosci. Remote, 52, 121–136, https://doi.org/10.1109/TGRS.2012.2236845, 2014.

Korosov, A. A., Hansen, W. M., Dagestad, F. K., Yamakawa, A., Vines, A., and Riechert, A.: Nansat: a Scientist-Orientated Python Package for Geospatial Data Processing, J. Open Res. Softw., 4, e39, https://doi.org/10.5334/jors.120, 2016.

Kwok, R., Curlander, J. C., McConnell, R., and Pang, S.: An Ice Motion Tracking System at the Alaska SAR Facility, IEEE J. Ocean. Eng., 15, 44–54, 1990.

Muckenhuber, S., Korosov, A. A., and Sandven, S.: Open-source feature-tracking algorithm for sea ice drift retrieval from Sentinel-1 SAR imagery, The Cryosphere, 10, 913–925, https://doi.org/10.5194/tc-10-913-2016, 2016.

Nansen, F.: The Oceanography of the North Polar Basin. Scientific Results, Vol. 3, 9, Longman Green and Co., Kristinania, Norway, 1902.

Pedersen, L. T., Saldo, R., and Fenger-Nielsen, R.: Sentinel-1 results: Sea ice operational monitoring, IEEE International Geoscience and Remote Sensing Symposium (IGARSS), 26–31 July 2015, Milan, Italy, 2828–2831, https://doi.org/10.1109/IGARSS.2015.7326403, 2015

Rampal, P., Weiss, J., Marsan, D., and Bourgoin, M.: Arctic sea ice velocity field: General circulation and turbulent-like fluctuations, J. Geophys. Res.-Oceans, 114, C10014, https://doi.org/10.1029/2008JC005227, 2009a.

Rampal, P., Weiss, J., and Marsan, D.: Positive trend in the mean speed and deformation rate of Arctic sea

ice 1979–2007, J. Geophys. Res.-Oceans, 114, C5013, https://doi.org/10.1029/2008JC005066, 2009b.

Rosten, E. and Drummond, T.: Machine learning for high-speed corner detection, in: European Conference on Computer Vision, 7–13 May 2006, Graz, Austria, 430–443, https://doi.org/10.1007/11744023_34, 2006.

Rublee, E., Rabaud, V., Konolige, K., and Bradski, G.: ORB: an efficient alternative to SIFT or SURF, IEEE I. Conf. Comp. Vis. (ICCV), 6–13 November 2011, Barcelona, Spain, 2564–2571, https://doi.org/10.1109/ICCV.2011.6126544, 2011.

Spreen, G. and Itkin, P.: N-ICE2015 buoy data, Norwegian Polar Institute, https://data.npolar.no/dataset/6ed9a8ca-95b0-43be-bedf-8176bf56da80 (last access: 30 August 2016), 2015.

Thomas, M., Geiger, C. A., and Kambhamettu, C.: High resolution (400 m) motion characterization of sea ice using ERS-1 SAR imagery, Cold Reg. Sci. Technol., 52, 207–223, 2008.

Thorndike, A. S. and Colony, R.: Sea ice motion in response to geostrophic winds, J. Geophys. Res.-Oceans, 87, Nr. C8, 5845–5852, https://doi.org/10.1029/JC087iC08p05845, 1982.

Widell, K., Østerhus, S., and Gammelsrød, T.: Sea ice velocity in the Fram Strait monitored by moored instruments, Geophys. Res. Lett., 30, 1982, https://doi.org/10.1029/2003GL018119, 2003.

BIBLIOGRAPHY

Arrigo, Kevin R., Thomas Mock, and Michael P. Lizotte

2010 "Sea Ice", in ed. by David N. Thomas and Gerhard S. Dieckmann, second edition, Wiley-Blackwell, chap. 8 Primary Producers and Sea Ice.

Berg, Anders and Leif E. B. Eriksson

2014 "Investigation of a Hybrid Algorithm for Sea Ice Drift Measurements Using Synthetic Aperture Radar Images", *IEEE Transactions on Geoscience and Remote Sensing*, 52, 8, pp. 5023-5033.

Bogdanov, Andrey V., Stein Sandven, Ola M. Johannessen, Vitaly Yu. Alexandrov, and Leonid P. Bobylev

2005 "Multisensor Approach to Automated Classification of Sea Ice Image Data", *IEEE Transactions on Geoscience and Remote Sensing*, 43, 7, pp. 1448-1664.

Clausi, David A.

2002 "An analysis of co-occurrence texture statistics as a function of grey level quantization", *Can. J. Remote Sensing*, 28, 1, pp. 45-62.

Clausi, David A., Kai A. Qin, M S Chowdhury, P. Yu, and Philippe Maillard

2010 "MAGIC: MAp-Guided Ice Classification System", *Canadian Journal of Remote Sensing*, 36, S1, S13-S25, DOI: 10.5589/m10-008, eprint: http://dx.doi.org/10.5589/m10-008, http://dx.doi.org/10.5589/m10-008.

Collins, Michael J. and William J. Emery

1988 "A computational method for estimating sea ice motion in sequential Seasat synthetic aperture radar imagery by matched filtering", *Journal of Geophysical Research: Oceans*, 93, C8, pp. 9241-9251, ISSN: 2156-2202, DOI: 10.1029/JC093iC08p09241, http://dx.doi.org/10.1029/JC093iC08p09241.

Curlander, John C., Benjamin Holt, and Hussey Kevin J.

1985 "Determination of sea ice motion using digital SAR imagery", *IEEE Journal of Oceanic Engineering*, 10, 4, pp. 358-367.

Daida, Jasonand, Ramin Samadani, and John F. Vesecky

1990 "Object-oriented Feature-tracking Algorithms For SAR Image Of The Marginal Ice Zone", *IEEE Transactions on Geoscience and Remote Sensing*, 28, 4, pp. 573-589.

Dieckmann, Gerhard S. and Hartmut H. Hellmer

2010 "Sea Ice", in ed. by David N. Thomas and Gerhard S. Dieckmann, second edition, Wiley-Blackwell, chap. 1 The Importance of sea ice: An Overview.

Dokken, Sverre Thune, Peter Winsor, Thorsten Markus, Jan Askne, and Göran Björk

2002 "{ERS} {SAR} characterization of coastal polynyas in the Arctic and comparison with SSM/I and numerical model investigations", *Remote Sensing of Environment*, 80, 2, pp. 321-335, ISSN: 0034-4257, DOI: http://dx.doi.org/10.1016/S0034-4257(01)00313-3, http://www.sciencedirect.com/science/article/pii/S0034425701003133.

Eicken, Hajo, Rolf Gradinger, Maya Salganek, Kunio Shirasawa, Don Perovich, and Leppäranta Matti

2009 (eds.), *Field Techniques for Sea Ice Research*, ISBN: 978-1-60223-059-0, University of Alaska Press.

Fily, Michel and D.A. Rothrock

1987 "Sea Ice Tracking by Nested Correlations", *IEEE Transactions on Geoscience and Remote Sensing*, GE-25, 5, pp. 570-580.

Geldsetzer, Torsten and John J. Yackel

2009 "Sea ice type and open water discrimination using dual co-polarized C-band SAR", *Canadian Journal of Remote Sensing*, 35, 1, pp. 73-84, DOI: 10.5589/m08-075, eprint: http://dx.doi.org/10.5589/m08-075, http://dx.doi.org/10.5589/m08-075.

Gill, Jagvijay P.S. and John J. Yackel

2012 "Evaluation of C-band SAR polarimetric parameters for discrimination of first-year sea ice types", *Canadian Journal of Remote Sensing*, 38, 3, pp. 306-323, DOI: 10.5589/m12-025, eprint: http://dx.doi.org/10.5589/m12-025, http://dx.doi.org/10.5589/m12-025.

Haarpaintner, Jörg and Stian Solbø

2007 *Automatic ice-ocean discrimination in SAR imagery*, Tech. Rep. Norut IT-rapport.

Hall, R.T. and D.A. Rothrock

1981 "Sea ice displacement from Seasat synthetic aperture radar", *Journal of Geophysical Research*, 86, C11, pp. 11078-11082.

Hollands, Thomas and Wolfgang Dierking

2011 "Performance of a multiscale correlation algorithm for the estimation of sea-ice drift from SAR images: initial results", *Annals of Glaciology*, 52, 57, pp. 311-317.

Karvonen, Juha

2010 "Geoscience and Remote Sensing New Achievements", in ed. by Pasquale Imperatore and Daniele Riccio, InTech, chap. 8 C-Band Sea Ice SAR Classification Based on Segmentwise Edge Features.

2012 "Operational SAR-based sea ice drift monitoring over the Baltic Sea", *Ocean Science*, 8, pp. 473-483.

Karvonen, Juha, Markku Similä, and Marko Mäkynen

2005 "Open Water Detection From Baltic Sea Ice Radarsat-1 SAR Imagery", *IEEE Geoscience and Remote Sensing Letters*, 2, 3.

Kloster, K., H. Flesche, and O.M. Johannessen

1992 "Ice motion from airborne SAR and satellite imagery", *Advances in Space Research*, 12, 7, pp. 149-153, ISSN: 0273-1177, DOI: http://dx.doi.org/10.1016/0273-1177(92)90210-O, http://www.sciencedirect.com/science/article/pii/027311779290210O.

Komarov, Alexander S. and David G. Barber

2014 "Sea Ice Motion Tracking From Sequential Dual-Polarization RADARSAT-2 Images", *IEEE Transactions on Geoscience and Remote Sensing*, 52, 1, pp. 121-136.

Kwok, R. and G. F. Cunningham

2002 "Seasonal ice area and volume production of the Arctic Ocean: November 1996 through April 1997", *Journal of Geophysical Research: Oceans*, 107, C10, 8038, SHE 12-1-SHE 12-17, ISSN: 2156-2202, DOI: 10.1029/2000JC000469, http://dx.doi.org/10.1029/2000JC000469.

Kwok, Ronald, John C. Curlander, Ross McConnell, and Shirley S. Pang

1990 "An ice-motion tracking system at the Alaska SAR facility", *IEEE Journal of Oceanic Engineering*, 15, 1, pp. 44-54.

Leigh, Steven, Zhijie Wang, and David A. Clausi

2014 "Automated Ice-Water Classification Using Dual Polarization SAR Satellite Imagery", *IEEE Transactions on Geoscience and Remote Sensing*, 52, 9, pp. 5529-5539.

Leppäranta, Matti

2011 *The Drift of Sea Ice*, second edition, ISBN: 978-3-642-04682-7, Springer.

Maillard, Philippe, David A. Clausi, and H. Deng

2005 "Map-guided sea ice segmentation and classification using SAR imagery and a MRF segmentation scheme", *IEEE Transactions on Geoscience and Remote Sensing*, 43, 12, pp. 2940-2951.

Mäkynen, Marko P., A. Terhikki Manninen, Markku H. Similä, Juha A. Karvonen, and Martti T. Hallikainen

2002 "Incidence angle dependence of the statistical properties of C-band HH-polarization backscattering signatures of the Baltic Sea ice", *IEEE Transactions on Geoscience and Remote Sensing*, 40, 12, pp. 2593-2605.

McCandless, Samuel W. and Christopher R. Jackson

2004 "Synthetic Aperture Radar Marine User's Manual", in ed. by Christopher R. Jackson and John R. Apel, U.S. department of commerce, National Oceanic and Atmospheric Administration, chap. 1 Principles of Synthetic Aperture Radar, pp. 1-23.

McConnell, Ross, Ronald Kwok, John C. Curlander, Wolfgang Kober, and Shirley S. Pang

1991 "Psi-S correlation and dynamic time warping: two methods for tracking ice floes in SAR images", *IEEE Transactions on Geoscience and Remote Sensing*, 29, 6, pp. 1004-1012.

McPhee, Miles

2008 *Air-Ice-Ocean Interaction: Turbulent Ocean Boundary Layer Exchange Processes*, ISBN: 978-0-387-78334-5, Springer.

Meier, Walter N. and Thorsten Markus

2015 "Remote Sensing of the Cryosphere", in ed. by Marc Tedesco, John Wiley and Sons, Ltd, chap. 11 Remote sensing of sea ice, pp. 248-272.

Moreira, Alberto, Pau Prats-Iraola, Marwan Younis, Gerhard Krieger, Irena Hajnsek, and Konstantinos Papathanassiou

2013 "A Tutorial on Synthetic Aperture Radar", *IEEE Geoscience and remote sensing magazine*, doi: 10.1109/MGRS.2013.2248301 (Apr. 2013), pp. 6-43.

Muckenhuber, S. and S. Sandven

2017 "Open-source sea ice drift algorithm for Sentinel-1 SAR imagery using a combination of feature tracking and pattern matching", *The Cryosphere*, 11, 4 (Aug. 2017), pp. 1835-1850, DOI: 10.5194/tc-11-1835-2017, https://www.the-cryosphere.net/11/1835/2017/.

Muckenhuber, Stefan, Anton Andreevich Korosov, and Stein Sandven

2016 "Open-source feature-tracking algorithm for sea ice drift retrieval from Sentinel-1 SAR imagery", *The Cryosphere*, doi:10.5194/tc-10-913-2016, 10, pp. 913-925.

Muckenhuber, Stefan, Frank Nilsen, Anton Andreevich Korosov, and Stein Sandven

2016 "Sea ice cover in Isfjorden and Hornsund, Svalbard (2000–2014) from remote sensing data", *The Cryosphere*, doi:10.5194/tc-10-149-2016, 10, pp. 149-158.

Nansen, Fridtjof

1902 "The Oceanography of the North Polar Basin. Scientific Results", in 9, Longmans, Green and Company, vol. 3.

Ochilov, Shuhratchon and David A. Clausi

2012 "Operational SAR Sea-Ice Image Classification", *IEEE Transactions on Geoscience and Remote Sensing*, 50, 11, pp. 4397-4408.

Onstott, Robert G.

1992 "Microwave Remote Sensing of Sea Ice", in ed. by Frank D. Carsey, American Geophysical Union, chap. 5 SAR and Scatterometer Signatures of Sea Ice, pp. 73-104.

Onstott, Robert G. and Robert A. Shuchman

2004 "Synthetic Aperture Radar Marine User's Manual", in ed. by Christopher R. Jackson and John R. Apel, U.S. department of commerce, National Oceanic and Atmospheric Administration, chap. 3 SAR Measurements of Sea Ice, pp. 81-115.

Pedersen, Leif T., Roberto Saldo, and Rasmus Fenger-Nielsen

2015 "Sentinel-1 results: Sea ice operational monitoring", in *2015 IEEE International Geoscience and Remote Sensing Symposium (IGARSS)*, doi=10.1109/IGARSS.2015.7326403, IEEE, pp. 2828-2831.

Petrich, Chris and Hajo Eicken

2010 "Sea Ice", in ed. by David N. Thomas and Gerhard S. Dieckmann, second edition, Wiley-Blackwell, chap. 2 Growth, Structure and Properties of Sea Ice.

Polyak, Leonid, Richard B. Alley, John T. Andrews, Julie Brigham-Grette, Thomas M. Cronin, Dennis A. Darby, Arthur S. Dyke, Joan J. Fitzpatrick, Svend Funder, Marika Holland, Anne E. Jennings, Gifford H. Miller, Matt O'Regan, James Savelle, Mark Serreze, Kristen St. John, James W.C. White, and Eric Wolff

2010 "History of sea ice in the Arctic", *Quaternary Science Reviews*, 29, 15–16, Special Theme: Arctic Palaeoclimate Synthesis (PP. 1674-1790), pp. 1757-1778, ISSN: 0277-3791, DOI: http://dx.doi.org/10.1016/j.quascirev.2010.02.010, http://www.sciencedirect.com/science/article/pii/S0277379110000429.

Sandven, Stein, Vitaly Y. Alexandrov, Natalia Zakhvatkina, and Mohammed Babiker

2012 "Sea ice classification using RADARSAT-2 Dual Polarisation data", SeaSAR 2012, the 4th International Workshop on Advances in SAR Oceanography, Tromso, Norway, 18-22 June 2012.

Sandven, Stein and Ola M. Johannesen

2006 "Manual of Remote Sensing: Remote Sensing of the Marine Environment", in ed. by James F.R. Gower, 3rd, The American Society for Photogrammetry and Remote Sensing, vol. 6, chap. 8 Sea Ice Monitoring by Remote Sensing, pp. 241-283.

Sandven, Stein, Ola M. Johannessen, Martin W. Miles, Lasse H. Pettersson, and Kjell Kloster

1999 "Barents Sea seasonal ice zone features and processes from ERS 1 synthetic aperture radar: Seasonal Ice Zone Experiment 1992", *Journal of Geophysical Research: Oceans*, 104, C7, pp. 15843-15857, ISSN: 2156-2202, DOI: 10.1029/1998JC900050, http://dx.doi.org/10.1029/1998JC900050.

Shokr, Mohammed

2009 "Compilation of a radar backscatter database of sea ice types and open water using operational analysis of heterogeneous ice regimes", *Can. J. Remote Sensing*, 35, 4, pp. 369-384.

Shokr, Mohammed E.

1991 "Evaluation of second-order texture parameters for sea ice classification from radar images", *Journal of Geophysical Research: Oceans*, 96, C6, pp. 10625-10640, ISSN: 2156-2202, DOI: 10.1029/91JC00693, http://dx.doi.org/10.1029/91JC00693.

Shokr, Mohammed and Nirmal Sinha

2015 *Sea Ice: Physics and Remote Sensing, Geophysical Monograph 209*, ISBN: 978-1-119-02789-8, American Geophysical Union, John Wiley and Sons.

Showman, Gregory A.

2010 "Principles of Modern Radar", in ed. by Mark A. Richards, James A. Scheer, and William A. Holm, Scitech Publishing, vol. Volume I - Basic Principles, chap. 21. An Overview of Radar Imaging.

Soh, Leen-Kiat and Costas Tsatsoulis

1999 "Texture analysis of SAR sea ice imagery using gray level co-occurrence matrices", *IEEE Transactions on Geoscience and Remote Sensing*, 37, 2, pp. 780-795.

Soh, Leen-Kiat, Costas Tsatsoulis, Denise Gineris, and Cheryl Bertoia

2004 "ARKTOS: An Intelligent System for SAR Sea Ice Image Classification", *IEEE Transactions on Geoscience and Remote Sensing*, 42, 1, pp. 229-248.

Stroeve, Julienne and Walt Meier

2017 "Sea Ice Trends and Climatologies from SMMR and SSM/I-SSMIS, Version 2." *Boulder, Colorado USA. NASA National Snow and Ice Data Center Distributed Active Archive Center.* doi: http://dx.doi.org/10.5067/EYICLBOAAJOU.

Sullivan, Roger

2008 "Radar Handbook", in ed. by Merrill Skolnik, Third Edition, McGraw Hill, chap. 17. Synthetic Aperture Radar.

Sun, Y.

1996 "Automatic ice motion retrieval from ERS-1 SAR images using the optical flow method", *International Journal of Remote Sensing*, 17, 11, pp. 2059-2087, DOI: 10.1080/01431169608948759, eprint: http://dx.doi.org/10.1080/01431169608948759, http://dx.doi.org/10.1080/01431169608948759.

Thomas, M., C.A. Geiger, and C. Kambhamettu

2008 "High resolution (400 m) motion characterization of sea ice using ERS-1 {SAR} imagery", *Cold Regions Science and Technology*, 52, 2, Research in Cryospheric Science and Engineering, pp. 207-223, ISSN: 0165-232X, DOI: http://dx.doi.org/10.1016/j.coldregions.2007.06.006, http://www.sciencedirect.com/science/article/pii/S0165232X07001449.

Tomiyasu, Kiyo

1978 "Tutorial Review of Synthetic-Aperture Radar (SAR) with Applications to Imaging of the Ocean Surface", *Proceedings of the IEEE*, 66, 5 (May 1978).

Tynan, Cynthia T., David G. Ainley, and Ian Stirling

2010 "Sea Ice", in ed. by David N. Thomas and Gerhard S. Dieckmann, second edition, Wiley-Blackwell, chap. 11 Sea Ice: A Critical Habit for Polar Marine Mammals and Birds.

Ulaby, Fawwaz T., David G. Long, William Blackwell, Charles Elachi, Adrian Fung, Chris Ruf, Kamal Sarabandi, Jakob van Zyl, and Howard Zebker

2014 *Microwave Radar and Radiometric Remote Sensing*, Ann Arbor, University of Michigan Press.

Ulaby, Fawwaz T., Richard K. Moore, and Adrian K. Fung

1986 *Microwave remote sensing: active and passive, Volume III: from theory to applications*, Artech House Inc.

Vesecky, John F., Ramin Samadani, Martha P. Smith, Jason M. Daida, and Ronald N. Bracewell

1988 "Observation of sea-ice dynamics using synthetic aperture radar images: automated analysis", *IEEE Transactions on Geoscience and Remote Sensing*, 26, 1, pp. 38-48.

Warren, Stephen G., Ignatius G. Rigor, Norbert Untersteiner, Vladimir F. Radionov, Nikolay N. Bryazgin, Yevgeniy I. Aleksandrov, and Roger Colony

1999 "Snow Depth on Arctic Sea Ice", *Journal of Climate*, 12, 1814-1829.

Younis, Marwan

2015 "Synthetic Aperture Radar (SAR): Principles and Applications" (Sept. 2015), presentation at 6th ESA advanced trainging course on land remote sensing in Bucharest Romania.

Yu, Peter, A. K. Qin, and David A. Clausi

2012 "Feature extraction of dual-pol SAR imagery for sea ice image segmentation", *Canadian Journal of Remote Sensing*, 38, 3, pp. 352-366, DOI: 10.5589/m12-028, eprint: http://dx.doi.org/10.5589/m12-028, http://dx.doi.org/10.5589/m12-028.

Yu, Qiyao and David A. Clausi

2008 "IRGS: Image Segmentation Using Edge Penalties and Region Growing", *IEEE Transactions on Pattern Analysis and Machine Intelligence*, 30, 12, pp. 2126-2139.

Zakhvatkina, Natalia, Vitaly Y. Alexandrov, Ola M. Johannessen, Stein Sandven, and Ivan Y. Frolov

2013 "Classification of Sea Ice Types in ENVISAT Synthetic Aperture Radar Images", *IEEE Transactions on Geoscience and Remote Sensing*, 51, 5, pp. 2587-2600.

Zakhvatkina, Natalia, Anton A. Korosov, Stefan Muckenhuber, Stein Sandven, and Mohammed Babiker

2017 "Operational algorithm for ice–water classification on dual-polarized RADARSAT-2 images", *The Cryosphere*, 11, 1, pp. 33-46.